Mass transport on micro and macro scale during moisture management and post-drying of Li-ion battery production

Zur Erlangung des akademischen Grades eines

DOKTORS DER INGENIEURWISSENSCHAFTEN

von der KIT-Fakultät für Chemieingenieurwesen und Verfahrenstechnik des
Karlsruher Instituts für Technologie (KIT)
genehmigte

Dissertation

von
Thilo Sebastian Heckmann
aus Plankstadt

Tag der mündlichen Prüfung:	20.10.2025
Erster Gutachter:	Prof. Dr.-Ing. Dr. h. c. Wilhelm Schabel
Zweiter Gutachter:	Prof. Dr.-Ing. Arno Kwade

Kurzfassung

Li-Ionen-Batterien (LiB) leisten einen wesentlichen Beitrag zur Transformation von fossilen zu erneuerbaren Energiequellen. Ihr Anwendungsbereich reicht von tragbaren Geräten bis hin zu stationären Energiespeichersystemen. Außerdem werden LiB für den Antrieb von Fahrzeugen verwendet, um den Transportsektor zu dekarbonisieren. Während der Betrieb von Elektrofahrzeugen ohne Verbrennungsemissionen auskommt, muss die Kohlenstoffbilanz die Emissionen bei der Erzeugung des Ladestroms und bei der Produktion der LiB einschließen. Nur so kann ein ganzheitlicher Vergleich zu den Emissionen von Verbrennungsmotoren gezogen werden. Die Massenproduktion von LiB ist eine komplexe Prozesskette, die die Produktion des aktiven Materials, die Herstellung der Elektroden, die Zellfertigung und den Modulbau beinhaltet. Die Optimierung dieser gesamten Prozesskette reduziert den ökologischen Fußabdruck von LiB durch die Verringerung von Emissionen. Die Motivation für diese Arbeit ist die Optimierung der Elektrodenproduktion und der Zellmontage. Bei der Elektrodenproduktion wird das Aktivmaterial der LiB in einem Lösungsmittel dispergiert und mit Additiven als dünner Film auf die Stromableiterfolien appliziert. Die entstandenen Elektroden werden zu einer Zelle zusammengebaut, indem Anode, Separator und Kathode in einem Gehäuse eingebracht und mit einem Elektrolyten befüllt werden.

Der Wassergehalt einer Zelle wirkt sich auf deren Leistung aus und muss vor dem Befüllen mit Elektrolyten auf einen optimalen Wert eingestellt werden. Der optimale Wassergehalt in einer Zelle hängt von der Chemie der Zelle ab und liegt im Millionstel-Bereich. Da der Wassergehalt so niedrig ist, wird er durch Sorption von Wasser in der Produktionsatmosphäre in Anode, Kathode und Separator beeinflusst. Besondere Maßnahmen sind erforderlich, um den optimalen Wassergehalt in den Bauteilen vor der Befüllung des Elektrolyten einzustellen. Diese Maßnahmen sind die Nachtrocknung und das Feuchtemanagement. Die Nachtrocknung erfolgt entweder in kontinuierlichen Rolle-zu-Rolle Trocknern oder in Batch-Vakuumöfen. In den Öfen werden Elektroden- und Separator-Coils oder Zellstapel nachgetrocknet. Nach diesem

Trocknungsschritt befindet sich die Produktion in Trockenräumen. Die Atmosphäre in diesen Räumen vermindert die Resorption von Wasser in die Zellkomponenten, bis die Zelle mit dem Elektrolyten befüllt wird und versiegelt ist. Trockenräume und Nachtrocknung haben einen hohen Energieverbrauch. Daher hat deren Optimierung das Potential, den Energieverbrauch der Zell-Fertigung zu reduzieren. Diese Reduzierung kann durch eine bedarfsorientierte Auslegung der Prozesse erreicht werden, die durch ein grundlegendes Verständnis der Sorption und des Stofftransports während der Nachtrocknung und des Feuchtemanagements möglich wird.

Diese Arbeit trägt zur Optimierung der Nachtrocknung und des Feuchtemanagements durch Grundlagenforschung bei. Die Überführung der Grundlagenforschung in Modelle ermöglicht eine Simulation der Prozesse. Diese Überführung ist für den Stofftransport von Wasser durch die Kompositstruktur einer Elektrode vorgesehen. Insbesondere wird die Modellierung des Wassertransports während der Lagerung, des Handlings und der Nachtrocknung im Coil-Format vorangetrieben. Je nach Konfiguration der Elektroden bei der Nachtrocknung und dem Feuchtemanagement findet der Stofftransport auf unterschiedlichen Längenskalen statt. Konkret wird in dieser Arbeit:

- ein zwei-skaliges Stofftransportmodell entwickelt, das die Stofftransportphänomene auf Mikro- und Markoskala in Anoden berücksichtigt
- ein geeignetes Modell zur Beschreibung der Diffusion durch die poröse Struktur einer Elektrode gefunden
- die Sorption auf Mikroskala in dem aktiven Kathodenmaterial Nickel-Kobalt-Mangan untersucht.

Zunächst wird das Two-Scale-Model entwickelt, bei dem der Stofftransport auf Mikro- und Makroskala jeweils instationäre Stofftransportphänomene darstellt. Dieses Modell berücksichtigt den Stofftransport in mehreren Phasen und auf zwei Längenskalen. Die partiellen Differentialgleichungen des Stofftransports auf Mikro- und Makroskala werden numerisch über die Zeitachse gekoppelt. Die Stofftransportwiderstände werden durch Diffusionszeiten τ charakterisiert. Diese sagen aus, ob der Einfluss des Stofftransports von Wasser in der Elektrode auf der Mikro- oder Makroskala überwiegt. Das Two-Scale-Modell wird durch Betrachtung von Grenzfällen validiert. Zusätzlich werden Sorptionsexperimente an Elektroden mit definierten Stofftransportwegen auf der Makroskala zur Validierung des Modells genutzt. Dieses neue Modell vereint den Stofftransport in der Kompositstruktur einer Elektrode mit dem aktuellen Wissensstand des Stofftransports in einzelnen Elektrodenkomponenten. Das erhöht die Vorhersagbarkeit von Feuchtemanagement und Nachtrocknungsprozessen in der Massenproduktion.

Ein neuartiger Versuchsaufbau zur Messung der Trocknungsverläufe bei reduziertem Druck liefert zeitaufgelöste Trocknungskurven für poröse Strukturen, die Elektroden ähneln. Dieser Aufbau liefert Daten für die Validierung des Stofftransports auf der Makroskala des Two-Scale-Models. Der Stofftransportwiderstand ist die Gasphase in der porösen Struktur der Elektrode. Wenn die Nachtrocknung unter Vakuum durchgeführt wird, kann die Knudsen Diffusion diesen Stofftransport beeinflussen. Daher wird ein Modell für den Diffusionskoeffizienten von Wasser in der Gasphase einer porösen Struktur vorgeschlagen. Dieses Modell deckt den Übergang von Stefan (Fick‘schen) Diffusion zur Knudsen-Diffusion auf der Grundlage der Bosanquet-Gleichung ab. Graphit, das aktive Material von Anoden, dient in Form einer Schüttung als Modellstruktur. Das Fick‘sche Gesetz beschreibt zusammen mit einer Wasserbilanz den Stofftransport von Wasser in dieser Schüttung. Die Experimente zeigen, dass das Modell den Stofftransport von Wasser in der Gasphase der porösen Struktur korrekt abbildet. Die Knudsen-Diffusion beeinflusst den Stofftransport bei niedrigem Druck in Richtung Vakuum. Der Einfluss der Knudsen-Diffusion wird durch das Diffusionskoeffizientenmodell berücksichtigt. Die Genauigkeit der Simulation nimmt zum Vakuum hin ab, was auf einen Massentransportwiderstand des Wassers im Graphit zurückgeführt wird. Diese Ergebnisse ermöglichen eine bedarfsgerechte Prozessauslegung und das Modell kann zur Simulation der Vakuum-Coiltrocknung eingesetzt werden. Die Ergebnisse tragen zum Verständnis des gesamten Massentransport-Widerstandes in der Elektrode während der Massenproduktion bei.

Als Sorptionsphänomen auf der Mikro-Skala wird die physikalische und chemische Sorption von CO_2 und Wasser in Nickel-Kobalt-Mangan-Kathoden untersucht. Das Sorptionsverhalten dieser Kathoden in feuchter Atmosphäre mit CO_2 führt im Vergleich zum Sorptionsverhalten ohne CO_2 zu einer größeren und konstanten Massenaufnahme über einen langen Zeitraum. Die temperaturabhängige Reversibilität der Massenaufnahme zeigt, dass ein Großteil der aufgenommenen Masse nach Exposition in feuchter Atmosphäre mit CO_2 bei 115 °C nicht wieder abgegeben wird. Der Vergleich verschiedener Sorptionsexperimente deutet darauf hin, dass die Massenaufnahme von CO_2 in Kathodenaktivmaterial (CAM) die Sorption von CO_2 und Wasser in CAM kinetisch hemmt. Diese Hemmung ist eine Funktion der CAM-Chemie und der CO_2-Konzentration der Atmosphäre. Diese Erkenntnisse werten die Grundlagenforschung aus verfahrenstechnischer Sicht aus, um ihre Anwendbarkeit in der Industrie zu erhöhen. Die Unterscheidung zwischen chemischer und physikalischer Sorption sowie die Bewertung ihrer Kinetik ist von entscheidender Bedeutung für die Ausarbeitung von Materiallagerungskonzepten und die Entwicklung von Strategien für das Handling von CAM.

Abstract

Li-ion batteries (LiB) are an essential puzzle piece, which supports the transition from fossil to renewable energy sources. Their application ranges from small hand-held devices to large stationary energy-storage systems. LiB are also used to power vehicles to decarbonize commercial and personal transportation. While the operation of electric vehicles is free from combustion emissions, the carbon balance must include power generation for charging and production of the LiB. This enables a holistic comparison to the emissions from combustion vehicles. The mass production of LiB is a complex process chain, connecting active material production, electrode production, cell assembly, and module assembly. Optimizing these processes as a chain and individually reduces the ecological impact of LiB on the environment by reducing their cradle to gate emissions. The motivation of this thesis is the optimization of electrode production and cell assembly. Herein, the active material of the LiB, dissolved in a solvent with additives, is applied as thin films onto a current-collector foil. These electrodes are assembled to cells by placing anode, separator, and cathode in a housing and adding electrolyte.

The water content of a cell affects device performance and must be at an optimal level prior to electrolyte filling. This optimal water-level in a cell is in the range of parts per million and depends on the cell's chemistry. Water levels that are this low are affected by sorption of water from the production atmosphere in anode, cathode, and separator. Therefore, specific measures are taken to achieve the optimal water levels in the components of the cell prior to electrolyte filling. These measures are post-drying and moisture management. Post-drying is conducted either in batch vacuum ovens or in continuous roll-to-roll dryers. The ovens either post-dry coils of electrodes and separator or stacks of cells. After this drying step, the production is situated in dry rooms. The atmosphere in these rooms mitigates the resorption of water into the components of the cell until they are filled with electrolyte and sealed. Dry-rooms and post-drying are energy intensive and therefore have potential to reduce the energy consumption of LiB fabrication. A demand-oriented process design allows this reduction enabled by a profound understanding of the sorption and mass transport during the post-drying and moisture management.

This work contributes to the optimization of these processes through fundamental research. Transforming this fundamental research into models enables a simulation of these processes. This transformation is planned for the mass transport of water through the composite structure of an electrode. Especially the modeling of water mass transport during storage, handling and post-drying in coil format is addressed. Depending on the configuration of these processes, mass transport occurs on different lengths scale. Specifically, this work includes:

- the development of a two-scale mass-transport model, which accounts for mass-transport phenomena on micro and macro scale in anodes,
- the determination of a suitable model to describe the diffusion through the porous structure of an electrode, and
- the investigation of the micro-scale sorption in the cathode active material nickel-cobalt-manganese.

First, the Two-Scale-Model, where the mass transport on both, micro and macro scale is represented by transient mass-transport phenomena is developed. This model accounts for the mass transport in multiple phases and on two length scales. The partial differential equations of the mass transport on micro and macro scale are numerically coupled via the time scale. This arrangement of mass-transport resistances is characterized by diffusion times. The diffusion times determine if the influence of mass transport on micro or macro scale of water in the electrode predominates. This model is validated by the evaluation of boundary cases. Additionally, sorption experiments of electrodes with defined mass-transport distances on macro scale are used to validate the model. This new model connects the mass transport of a composite structure with the current state of knowledge of mass transport in the individual components of an electrode. This increases the predictability of moisture management and post-drying processes in mass production.

A novel experimental setup for measuring the propagation of drying at reduced pressure provides time-resolved drying curves for porous structures that resemble an electrode. This setup generates data for the validation of the mass-transport simulation on macro scale of the Two-Scale-Model. This mass transport is the gas-phase mass transport through the porous structure of the electrode. If post-drying is performed under vacuum, Knudsen diffusion may affect this mass transport. Therefore, a model for the diffusion coefficient of water in the gas phase of a porous structure is proposed. This model covers the transition from Stefan (Fickian) diffusion to Knudsen diffusion, based on the Bosanquet equation. Graphite, the active material of anodes, as backfill is the model structure. Fick's law with a water balance describes the mass transport in this backfill. The experiments show that the model correctly describes the mass transport of water in the gas phase of the porous structure. Knudsen diffusion affects the mass transport towards vacuum. The transition model of the diffusion coefficient accounts for this effect. The accuracy of the simulation decreases towards vacuum, which is currently attributed to a mass-transport resistance of water in the graphite. These results support a demand-oriented process design, and the model can be used to simulate vacuum-coil drying processes. These findings add to the understanding of the overall mass-transport resistance inside an electrode during mass production.

As a sorption phenomenon on micro scale, the physical and chemical sorption of CO_2 and water in nickel-cobalt-manganese cathode active materials (CAM) is investigated. The sorption behavior of this CAM in humid atmosphere with CO_2 results in a larger and constant mass uptake over a long period of time, compared to the mass uptake in an atmosphere without CO_2. The temperature-dependent reversibility of the mass uptake during exposure to humid atmospheres with CO_2 showed that most of the mass does not desorb at 115 °C. The comparison of sorption experiments indicates that the mass uptake of CO_2 in CAM kinetically limits the sorption of CO_2 and water in CAM. This limitation is a function of the CAM-chemistry and the CO_2 concentration of the atmosphere. These findings evaluate the fundamental research from a process engineering perspective to increase their applicability in industry. Differentiation between chemical and physical sorption as well as assessing their kinetics is crucial to designing material storage concepts and handling strategies of CAM.

Table of Contents

Symbols & Abbreviations

Latin Letters

T	Temperature	K
p	Pressure	Pa
$D_{i,j}$	Diffusion coefficient of i in j	m^2/s
M	Mass	kg
a_i	Activity of i	-
R	Gas constant	J/mol/K
f_i	Fugacity of i	Pa
k	Parameter BET	-
X_i	Mass loading of i	-
g	Parameter BET	-
K	Sorption constant	-
n	Number of sorbate layer	-
$\dot{n}_i$	Areal molar flux of i	$mol/m^2/s$
C_i	Concentration of i	mol/m^3
x	Space coordinate	m
V	Volume	m^3
L	Length	m
N_A	Avogadro constant	1/mol
r	Radius	m
$\bar{c}$	Mean molecule velocity	m/s
$\widetilde{M}_i$	Molar mass of i	g/mol
t	Time	s
z	Space coordinate	m
$\tilde{y}_i$	Molar fraction of i	-

Greek Letters

ε	Porosity	-
τ	Tortuosity	-
τ_{Macro}	Diffusion time macro scale	s
τ_{Micro}	Diffusion time micro scale	s

ρ	Gravimetric density	kg/m³
μ	Chemical potential	J/mol
Λ	Mean free path	m
$\tilde{\rho}$	Molar density	mol/m³
σ	Diameter of a molecule	m
$\Delta\nu$	Empirical diffusion volume	-
Φ	Volume fraction of the macro scale	-
β	Mass-transport coefficient	m/s

Subscripts & Superscripts

LV	Liquid – vapor
DP	Dew point
i	Component “i”
j	Component “j”
l	Liquid
g	Gas
+	Standard condition
w	Water
m	Monolayer
BET	Brunauer-Emmett-Teller
solid	Solid phase
fluid	Fluid phase
eff	Effective
c	Characteristic
v	Velocity
s	Solid
f	Fluid
Mi	Micro
Ma	Macro
k	Index of macro-scale mesh point
St	Stefan
Kn	Knudsen
SKT	Stefan-Knudsen-Transition
T	Transition

Dimensionless Numbers

Kn	Knudsen number
Bi	Biot number heat transfer
Bi'	Biot number mass transport

Abbreviations

LiB	Lithium-ion battery
SEI	Solid electrolyte interface
R2R	Roll-2-Roll
$LiPF_6$	Lithium hexafluorophosphate
CO_2	Carbon dioxide
NMP	N-methyl-2-pyrrolidone
PVDF	Polyvinylidene fluoride
CMC	Carboxymethyl cellulose
SBR	Styrene-butadiene rubber
NMC	Lithium nickel manganese cobalt oxides
MSB	Magnetic suspension balance
PI	Pressure indication
MI	Moisture indication
FC	Flow control
TC	Temperature control
IUPAC	International Union of Pure and Applied Chemistry
RH	Relative humidity
BET	Brunauer, Emmett, and Teller
ZBS	Zehner, Bauer, and Schlünder
CAM	Cathode active material
PDE	Partial differential equation
LiOH	Lithium hydroxide
Sim	Simulation
Exp	Experiment
SKT	Stefan Knudsen transition
I	Interval
St	Stefan

Preface

The research presented in this thesis was conducted during my employment as a research assistant of the Thin Film Technology (TFT) group at the Karlsruhe Institute of Technology (KIT). I would like to thank everyone who accompanied and supported me during this interesting, productive, positive, and joyful chapter of my life.

Prof. Dr.-Ing. Dr. h.c. Wilhelm Schabel and Dr.-Ing. Philip Scharfer supported and trusted me to pursue my own ideas and conduct research in an interesting and future-oriented field of research. Their broad network provided ample opportunities for fruitful cooperations and insightful conference visits, which was always rewarding to me. I am very thankful for being part of their great research group. I would also like to thank Margit Morvay for always being supportive in every way and having an open ear for our troubles.

I would like to thank Prof. Dr.-Ing. Arno Kwade for providing a second review of this thesis regardless of his many obligations.

A large factor for the success of my research and joy during the daily are the colleagues that provide a positive, supporting, and inspirational work environment. I am thankful for working with, Andreas Altvater, Philipp Barbig, Julian Borho, Tobias Börnhorst, David Burger, Ralf Diehm, Jochen Eser, Lisa Eser, Víctor Gracia, Alexander Hoffmann, Linus Janning, Julian Klemens, Jana Kumberg, Lukas Lödige, Kevin Ly, Jonas Mohacsi, Philipp Quarz, Sandro Spiegel, Max Tönsmann, and Nadine Zimmerer along with all colleagues from our partner, the institute of thermal process engineering (TVT), especially, Lisa Cloos, Julia Gandert, Gina Kaysan, and Oliver Queisser.

I also thank Prof. Dr.-Ing. Matthias Kind and Prof. Dr.-Ing. Thomas Wetzel of the TVT for the opportunity to be involved in student teaching in collaboration with the TFT.

Working with students was always very rewarding, both professionally and personally. My gratitude goes to every student that I was able to advise during either thesis work or student research, namely, Kassian Armbruster, Rieke Banzhaf, Philipp Barbig, Johannes Dörr, Felix Hollert, Nico Korell, Hannah Lepère, Lukas Madlindl, Anh Thi Pham, Aliénor Potthoff, Natalie Streller, and Guohui Yang.

The collaboration with other research institutions was a pleasant and productive way to forward the research of all partners. I am grateful for collaborating with Carina Heck, Fabienne Huttner, Hans Fenske, Maximilian Lechner, Mark Lippke, and Gabriela Ventura Silva.

I thank the Federal Ministry of Education and Research for the funding of the projects Sim4Pro, Epic, and InMiTro via the research clusters ProZell and InZePro. The goals of these projects provided inspiration for the research of this thesis.

Finally, I want to express my gratitude for the unconditional support of my family and fiancé. Without their support my academic career would not have been possible. I am deeply thankful for my fiancé that provided mental and professional support whenever necessary.

Mannheim, 01.03.2026

Thilo He

Thilo Heckmann

1 Introduction

The human's impact on the world's climate is threating the inhabitability of entire regions, increasing the frequency of severe weather events, and causing an overall rise of temperatures in the oceans and atmosphere. The mitigation of this impact on the climate is a pressing challenge of today's society. Many efforts aim to reach global and national climate goals and reduce the emission of greenhouse gases. Therefore, international climate agreements and conventions, national legislations, and statements of intent issued by large companies as well as governments are measures to reduce this emission.

For Germany's national climate targets, emissions are categorized into seven sectors depending on their origin. Here, the largest share of emissions comes from energy conversion, industry, and transport in that order. Referencing the emissions of 1990, the goal is to reduce national emissions by 65 % until 2030[1]. The goals for each sector vary. The emission reduction in, for example the transport sector is projected to decrease from 128 (2020) to 85 (2030) million tons CO_2-equivalent[2]. The transition to renewable primary energy sources such as wind and solar helps to achieve the climate goals of the abovementioned sectors.

Transitioning to renewable energy sources yields energy in the form of electricity, which despite being climate friendly brings challenges: Energy availability fluctuates and requirements for energy logistics change compared to fossils. Large amounts of electric energy must be stored. The solutions are manifold. In the case of the transport sector either battery-powered vehicles or fuel-cell powered vehicles can be climate-friendly alternatives to combustion engines. Decisive requirements are volumetric and gravimetric energy density, storability, and power availability. Both technologies have ad-

---

[1] https://www.gesetze-im-internet.de/ksg/BJNR251310019.html (17.05.2024)

[2] https://www.gesetze-im-internet.de/ksg/BJNR251310019.html (17.05.2024)

vantages, which is why they are recommended for specific tasks in the transportation sector (Cano et al., 2018).

Batteries such as Li-ion batteries (LiB) are especially suitable for short- to mid-range applications, which make them attractive for e.g. personal vehicles (Cano et al., 2018). The transition from combustion-engines to electric cars requires the mass production of these cars and batteries (Günther et al., 2016; Keppeler et al., 2020). While battery-powered vehicles run emission-free, given renewable energy is used for charging, a holistic consideration of its carbon footprint includes their production and recycling as well. The raw materials and the fabrication for the battery cells make up a large share of this footprint (Schünemann et al., 2016). Potential to minimize the footprint of electric vehicles lies in optimizing for example the production processes of their batteries such as LiB (Bryntesen et al., 2021).

The basic repeating unit of a LiB consists of anode, cathode, and separator, as shown in Figure 1.1 (Kaiser et al., 2014). In commercial LiB, these components are arranged to optimize performance (short diffusion paths for electrons and ions) and to be compact. This optimization results in an alternating layered structure of these components and requires the fabrication of thin films (Kwade et al., 2018). Large scale production of thin metal sheets as well as of separators (usually sheets of woven and non-woven fibers) are readily available. The large-scale production of thin, porous, composite electrodes made from cathode and anode materials for LiBs is an expensive part of the production of Li-ion batteries (Hawley and Li, 2019). Cell production and cell conditioning accompany this electrode production to complete the LiB production (Kwade et al., 2018).

The state-of-the-art process to produce electrodes is from liquid suspension and web (in this case the current collector) coating. The process begins by mixing the active materials in solvent with conductive and structure-building additives (Gordon et al., 2020; Mayer et al., 2020). Subsequently, this suspension is cast onto the current collector, usually by pre-metered coating techniques such as slot-die coating (Diehm et al., 2020; Schmitt et al., 2013; Spiegel et al., 2022). The liquid film passes through a dryer that removes the solvent, forms the porous film of the electrode, and determines the component distribution in the film (Altvater et al., 2023; Klemens et al., 2023; Kumberg et al., 2019; Lippke et al., 2022). A calendering unit compacts the porous film to the desired density. A post-drying or final drying step removes residual solvent and water from the components (Huttner et al., 2021b). The production continues in a dry room atmosphere after this drying step. During cell assembly the electrodes are slit to size, packed, contacted, and placed in a cell housing (Kwade et al., 2018; Lechner et al., 2024). Finally, the electrolyte is added, and the cell sealed (Hagemeister et al., 2023).[3]

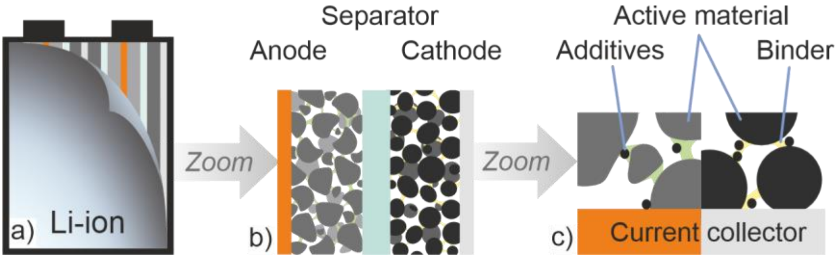

Figure 1.1: Zoom levels of a LiB. The cell (a) consists of several repeating units, which contain cathode, anode, and separator. Level (b) shows one repeating unit. The anode is coated on a copper foil and the cathode is coated on an aluminum foil with polymeric binder and conductive additives (c).

Many of the abovementioned processes hold potential to optimize cell quality and reduce energy consumption of the production (Ventura Silva et al., 2022). Material exclusive, coating and drying, and moisture management consume the largest proportion of the energy required to produce the cells of Li-ion batteries (Degen et al., 2023). Moisture management and post-drying are the motivation of the research that provides the basis for this dissertation.

---

[3] The order of the individual process steps may vary, depending on the manufacturer and cell geometry. This summary of the LiB cell production chain excludes details e.g., during cell assembly. For more details the reader is referred to comprehensive publications regarding the production chain of LiB by e.g. Kwade et al. (Kwade et al., 2018).

1.1 Moisture management and post-drying in Li-ion battery production

Moisture management and post-drying provide an optimal production environment, adjust the moisture levels in the cell components, and mitigate degradation of the components during mass production of LiB. These measures are necessary because moisture levels in the order of parts per million inside the components of a battery, even if only absorbed from the humidity in the atmosphere, may deteriorate device performance (Fenske et al., 2025; Stich et al., 2017). Additionally, the carbon dioxide (CO_2) levels in the atmosphere suffices to damage certain cathode active materials, if they are exposed to humid atmosphere (Jung et al., 2018).

The motivation behind moisture management and post-drying is a detrimental effect of moisture inside cell components on the performance of a LiB (Fenske et al., 2025; Lux et al., 2012; Plakhotnyk et al., 2005; Yang et al., 2016). A chemical reaction of water with the conducting salt lithium hexafluorophosphate ($LiPF_6$), of the electrolyte causes this detrimental effect, in the commercially most-used electrolyte system (Heider et al., 1999; Terborg et al., 2012). However, the influence of water inside a LiB on the formation of the solid electrolyte interface (SEI) can also be beneficial depending on the water concentration. Small concentrations of water can support the SEI formation, while significant concentrations of water negatively affect the SEI (Aurbach et al., 1999; Kitz et al., 2020; Langklotz et al., 2013; Vetter et al., 2005). A safety concern is the gas formation in the cell, which has also been observed due to added water to the electrolyte (Burns et al., 2013; Xiong et al., 2016).

Ecological and economic interests coincide in case of moisture management and post-drying. The energy consumption of these processes originates from the dehumidification and conditioning of the production environment and the heating and cooling of the post-drying ovens. A reduction of these energy costs is possible through a demand-oriented process design, enabled by a fundamental comprehension of the sorption of water and CO_2 in the individual components (Huttner et al., 2021b, 2020). Figure 1.2 schematically shows the connection between research and process optimization that supports sustainable production. The precise knowledge about the sorption of individual electrode component allows a demand-orientated process design of moisture management and post-drying as opposed to an "as dry as possible" modus operandi.

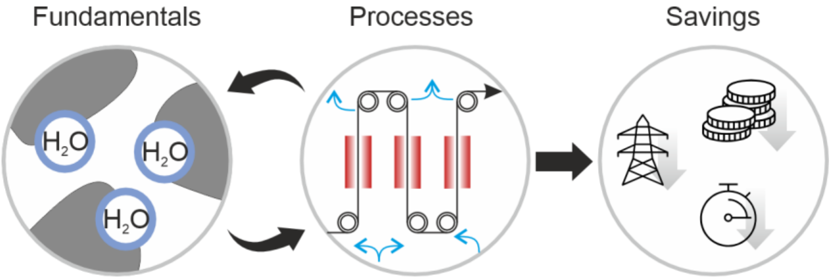

Figure 1.2: Fundamental science, represented by adsorption of water to a surface, and processes, represented by R2R post-drying, must be understood and connected for an ideal process design. This process design may be optimized to save resources, time, and money if fundamental science and processes are well aligned.

Fundamentals regarding sorption combined with process-oriented research aim to exploit the optimization potential in moisture management and post-drying. The term sorption describes the general phenomenon. Attributes of sorption are its mechanism, kinetics, and equilibrium. Figure 1.3 shows the sorption mechanisms, sorption kinetics and where they technically apply in the context of moisture management and post-drying. The sorption mechanisms are the fundamental basis that describe the physical interaction of water and CO_2 with battery components during moisture management and post-drying. Classifying the sorption into mechanisms is essential to understand the interaction of battery components and humid atmospheres. The next step is the quantification of sorption kinetics, showing the timescales on which the sorption happens. This kinetics description is crucial to apply the fundamental research to mass production in industry.

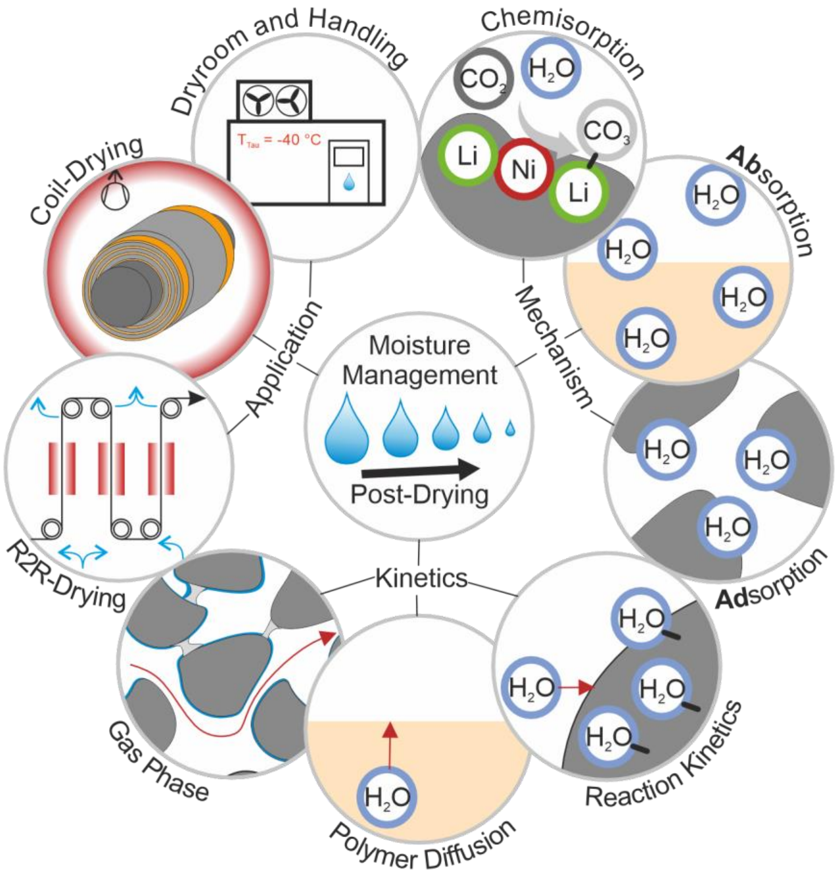

Figure 1.3: Selected aspects of moisture management and post-drying categorized into sorption mechanisms, their respective kinetics, and the technical applications in mass production. The sorption mechanisms range from chemical to physical sorption, classified according to the bond strength and adhesion location of the sorbing molecules. The mass transport of molecules within the battery electrodes during moisture management and post-drying depends on various kinetics. These sorption mechanisms and kinetics affect the interaction of battery components and the surrounding atmosphere during post-drying and in the dry rooms. All aspects of this interdisciplinary research area are addressed in recent literature and selected aspects will be addressed in this thesis.

During sorption, molecules (sorptive) from a gas phase attach to an either liquid or solid phase (sorbens). The mechanisms of sorption indicate the location where the sorptive adheres to the sorbens and which bond forms. Adsorption describes the adhesion to the surface of a sorbens. Absorption describes the uptake of the sorptive into the volume of the sorbens. Physical and chemical sorption differentiate mechanisms according to the strength of the bonds (details see chapter 3.1.2). Due to the large variety of materials inside a battery electrode, all sorption mechanisms occur.

Each sorption is restricted by sorption kinetics, which delay the adjustment of the thermodynamical sorption equilibrium. Reaction kinetics and mass-transport resistances may limit chemical sorption (Schlünder, 1996). The polymer diffusion restricts the absorption of gas molecules into the volume of for example a polymer binder in an electrode, which is temperature- and concentration-dependent (Eser et al., 2020a; Mamaliga et al., 2004; Schabel et al., 2007, 2004; Scharfer et al., 2008). Furthermore, the thickness of a polymeric film has been found to affect the diffusion mechanisms inside the film (Börnhorst et al., 2021, 2020), which could also have an effect on the polymeric binder inside an electrode. The diffusion through the gas phase of the porous electrode structure may also affect the sorption inside an electrode, especially if the electrodes are in coil format (Huttner et al., 2021b).

Dry rooms with dehumidifying units and either roll-to-roll dryer or vacuum ovens are the technical implementation of moisture management and post-drying in mass production of LiB electrodes, respectively (Kwade et al., 2018). The size of the dry-rooms depends on the layout of the production facility. The requirements for the dry-room vary according to the cell chemistry, human traffic in the dry rooms, and quality demands of the product. The technical implementation of the post-drying is not uniform across the giga factory landscape. Multiple large-scale batch-wise operating vacuum ovens are one option to remove moisture prior to and after cell assembly. Additionally, roll-2-roll (R2R) dryers could also post-dry electrodes. Their advantage is a low areal foot print in the factory and continuous processing.[4] However the handling of separators and high web speed may be challenging (Kosfeld et al., 2023).

From a physical point of view, moisture management mitigates ad-, ab-, and chemi-sorption (in general: water uptake) during mass production and post-drying accelerates desorption processes during final moisture and solvent removal of the components. The mechanisms of this sorption vary depending on the materials (Eser et al., 2020a). Therefore, it must be individually assessed for each production step and geometry of the electrode storage and handling. Some polymer binders absorb water into their volume and express a significant temperature dependency regarding the kinetics of this sorption (Eser et al., 2020b). Cathode active materials may chemically bind water and CO_2, which cannot be reversed once the electrodes are processed (Sicklinger et al., 2019). These are just two examples that show the complexity and diversity of the challenges during the design and operation of moisture management and post-drying.

1.2 Current state of research

The research of moisture management and post-drying is multi-disciplinary and comprises aspects of sorption, its kinetics, and process engineering, compare Figure 1.3. This research is motivated by the detrimental impact of water and CO_2 on the cell performance of LiB (discussed in the previous chapter). A comprehensive summary of the literature, focusing on topics from Figure 1.3, which are relevant for this thesis, follows.

Reduction of moisture in the cell's components by moisture management and post-drying is subject of many studies that focus on process engineering. Huttner et al. conducted experiments focusing on the post-drying of LiB electrodes (Huttner et al., 2020). Comparing various post-drying strategies, they found that the intensity of the post-drying routine alters physical proper-

---

[4] These insights originate form conversation with producers of post-drying machines, projects, factory visits, and conferences.

ties of electrode. They concluded that apart from moisture levels, thermal stability of the electrodes must be considered. Collaborating with us, Huttner et al. also provide a study about scientifically evaluated post-drying routines with simulation and evidence for hysteresis in the sorption of the components (Huttner et al., 2021b). Kosfeld et al. proposed individual moisture management and post-drying strategies for each electrode and the separator with a process evaluation of the various kinds of post-drying (Kosfeld et al., 2023). Huttner et al. showed the influence of calendering on the moisture absorption of NMC-622 (lithium nickel manganese cobalt oxides - atom ratio of Ni, Mn, Co, 60%:20%:20%) cathodes, which increases as a function of the calendering degree (Huttner et al., 2021a)[5]. The larger surface due to particle cracking provides more adsorption area. Fenske et al. showed that the cell assembly of the production of prelithiated anodes must be situated in a dry room atmosphere, to obtain sufficient cell stability (Fenske et al., 2024). In addition to the detrimental effects of moisture inside a cell, a negative effect of N-Methyl-2-pyrrolidone (NMP) residue from cathode processing has been shown despite post drying (Yue et al., 2024).

These studies show how production processes affect the moisture content of individual components of LiB-electrodes and separator and their impact on the cell performance. Understanding the mechanisms of sorption during these processes is necessary to control and monitor the water uptake and assess severity of the exposure to production atmospheres. Numerous studies address specific aspects of sorption inside LiB components and provide insight into the sorption mechanisms. Stich et al. reported that the moisture absorption varies depending on the electrodes and separators (Stich et al., 2017). They found that anodes and glass-fiber separators absorb the largest

---

[5] This publication is one of so far four publications from the fruitful and productive collaboration between the Institute for Particle Technology (iPAT) of the Technical University of Brunswick and the KIT-TFT on the topics of post-drying and moisture management:
Huttner, F.; Diener, A.; **Heckmann, T**.; Eser, J.C.; Abali, T.; Mayer, J.K.; Scharfer, P.; Schabel, W.; Kwade, A.: Increased Moisture Uptake of NCM622 Cathodes after Calendering due to Particle Breakage, In *J. Electrochem. Soc.* 2021 168 (9), 1499-1515 DOI: 10.1149/1945-7111/ac24bb

amounts of water. This valuable overview provided the basis for probing the components of a battery cell individually.

Cathodes such as NMC-622-cathodes may chemically degrade during processing: metallic components of the active material form hydroxides and carbonates. Jung et al. showed that the cathodes stored in humid atmosphere perform significantly worse than the control cathodes. They attribute this fact to the formation of nickel carbonates on the surface of nickel-rich NMC (Jung et al., 2018). Sicklinger et al. provide a detailed analysis of the species that form during storage and handling of NMC cathode active material during production, which also indicates that the nickel forms carbonates (Sicklinger et al., 2019). However, Zou et al. found that lithium is drawn to the surface of NMC in the presence of water vapor, which forms a self-passivating lithium-hydroxide layer (Zou et al., 2020). This passivation layer breaks down if CO_2 reaches it to form lithium-carbonate. These reactions are also reported in other studies (Schuer et al., 2022; Shkrob et al., 2017). Lechner et al. found that these carbonates reduce energy efficiency during formation but do not affect long-term performance of nickel-rich cathodes (~ 90 mol-% nickel) (Lechner et al., 2025).

These studies focus on the reactions of active material degradation and their impact on cell performance. Detailed analysis of the sorption of NMC-materials as function of atmosphere composition and time is not available.

The sorption of the **anode** was investigated in a predecessor work by Eser et al., they showed that the understanding of its sorption mechanism is crucial to identify which component of an anode is responsible for the water uptake (Eser et al., 2020b, 2020c). For example, in an anode with carboxymethyl cellulose (CMC) and styrene-butadiene rubber (SBR) as a binder system, the polymer CMC absorbs up to 85 wt-% of the water inside the electrode while posing only 2 wt-% of the entire electrode. Eser et al. further characterized the anode's components and showed hysteresis of the sorption, which has been confirmed by Huttner et al. These studies show that each material and component inside the LiB anode must individually be considered regarding their sorption (Huttner et al., 2021b).

The research of the previous two paragraphs elucidates sorption mechanisms in both electrodes. It provides the basis for understanding the sorption kinetics inside both electrodes. Understanding these kinetics is crucial to understanding sorption in production environments as a function of system parameters, such as relative humidity, temperature, and time. The kinetics of sorption in LiB materials and components has been addressed by the following studies.

Eser et al. investigated the kinetics of water sorption in the polymeric binders CMC and SBR and provided diffusion coefficients to model the sorption (Eser et al., 2020a). Following up on these results, Eser modeled the sorption in free-standing CMC/SBR anodes, which resembles the post-drying of anodes in R2R processes. The model was verified with sorption data, but requires a validation during drying (Eser, 2021). Huttner et al. approximated the drying time of electrode coils in a vacuum drying process via the gas-phase mass transport in the porous structure of the electrode (Huttner et al., 2021b). Zhao et al. probed the vacuum drying of LFP active material and fitted several empirical model equations (Zhao et al., 2018). Kosfeld et al. provide experimental data that show the kinetics during moisture management and post-drying of electrodes and separator (Kosfeld et al., 2023). These studies consider individual aspects of the entire mass transport inside an electrode, a comprehensive model of this entire mass transport is not published.

In conclusion, dependencies of the chemical sorption kinetics in NMC-cathodes on process and system parameters such as atmosphere composition, temperature, and time are yet to be investigated. The sorption mechanisms of anodes and their components as well as sorption kinetics of the CMC/SBR binder system with water are well known. Therefore, kinetics of the anode sorption are better understood than the ones of the cathode. However, the modeling of the kinetics, for example in coil format is absent. These models must incorporate the composite structure of an electrode. Building on this profound basis of knowledge, the research targets of this thesis are defined in the following chapter.

1.3 Aim of this Work

Eser has shown that the sorption in the composite structure of an electrode is a combination of sorption mechanisms in the individual components (Eser et al., 2020c, 2020b, 2020a). Therefore, the subjects of this thesis are:

- to elucidate sorption mechanisms and kinetics inside electrodes,
- to show how they collectively influence the overall mass-transport resistance of an electrode,
- and to place the findings in context of moisture management and electrode post-drying.

Classifying sorption and mass transport according to their length scales is necessary for the modeling of the overall sorption of e.g. water in an electrode. This overall sorption in an electrode is subdivided into sorption on micro (up to ~µm) and macro (up to ~cm) scale. This division accounts for the composite structure of an electrode. Figure 1.4 shows this classification with exemplary sorption mechanisms and an abstraction for the resulting mass-transport arrangement.

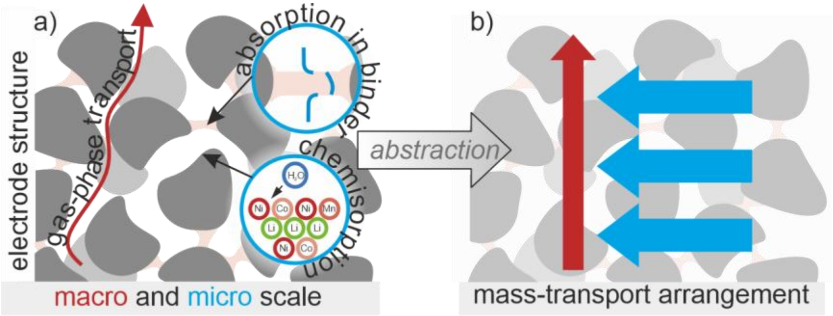

Figure 1.4: The electrode structure (a) consists of active material (gray) and the connecting binder phases (orange). The curved red arrow between these particles represents the mass transport on macro scale. The mass-transport resistance in the binder and the active material particles contribute to the sorption processes on micro scale. The abstraction of the electrode structure (b) shows the arrangement of the mass-transport resistances.

Three hypotheses guide the research to accomplish the goals of this thesis. These hypotheses address topics of individual mechanisms of sorption on micro and macro scale as well as their impact on the overall mass-transport resistance of an electrode.

Coupling sorption on micro and macro scale

Models for the sorption kinetics on micro and macro scale exist in literature. Due to the composite microstructure, it is possible that the kinetics on both scales affect the overall mass transport of an electrode during sorption, which is addressed via the first hypothesis.

Hypothesis 1: Describing the overall mass transport in the composite structure of electrodes requires the modeling of the sorption on micro and macro scale as coupled transient mass transport (compare Figure 1.5).

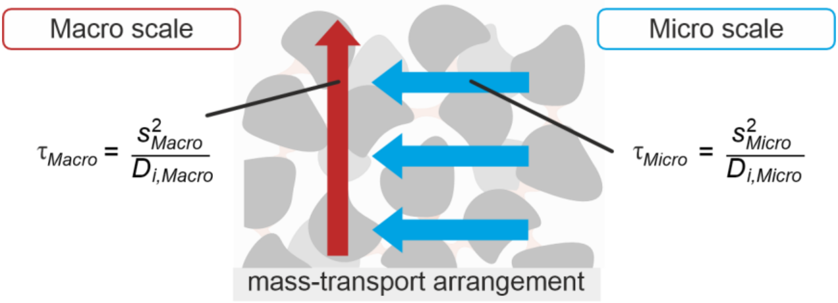

Figure 1.5: Outline of mass-transport resistances on micro and macro scale, representing ~µm and ~cm length scales, respectively. Both mass-transport resistances are transient transport phenomena coupled via the same time variable.

A model must be developed, where sorption on micro and macro scale each represent transient mass-transport phenomena, to assess the validity of this hypothesis. The model must account for the mass transport in multiple phases, two directions, and on two length scales. This structure can be implemented by coupling partial differential equations via the time scale. This model will connect the current state of knowledge for the sorption in the composite structure of an electrode. Diffusion times τ must be considered to quantify which scale's influence on the mass transport of the electrode predominates. Case studies are required to evaluate boundary cases, regarding the diffusion times. Additionally, experimental routines with sufficient accuracy must be established to provide validation data. Eventually, comparing results of the model to experimental data will validate hypothesis 1.

Macro scale: Mass transport in porous structures

The gas-phase mass transport in the porous structure is the mass transport on macro scale in an electrode, which has a transport distance in the range of cm during post-drying in coil format. Previous studies show that this mass-transport distance affects the post-drying result (Huttner et al., 2021b). Considering the vacuum drying in coil format, hypothesis 2 follows:

Hypothesis 2: A model for mass transport in the Stefan-Knudsen transition regime can be used to describe the mass transport inside the gas phase of an electrode structure at low pressure.

Validating this hypothesis requires comparing experiments and simulation that probe this mass transport in a porous model-structure that resembles an electrode. An experimental setup to evaluate drying curves at reduced pressure must be developed. The simulation must incorporate a component balance of water, and the sorption in the gas and solid phase. Figure 1.6 shows an exemplary distribution of pore- and particle-size distribution in the structure of an electrode and illustrates the regimes; Knudsen (discontinuum) and Stefan (continuum) diffusion. A model (e.g. the Bosanquet-equation) must be determined that describes the diffusion-dependent mass transport in this porous structure to validate hypothesis 2.

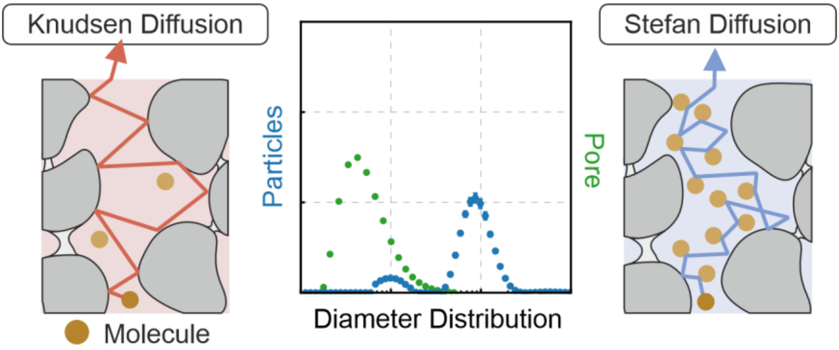

Figure 1.6: Schematics of Knudsen and Stefan diffusion inside a porous structure. The molecule-wall interaction governs the mass transport during Knudsen diffusion (left). The molecule-molecule interaction governs the mass transport of Stefan diffusion (right). The pore diameter is a distribution inside an electrode due to the particle size distribution (middle).

Micro scale: Sorption behavior of cathode active materials

Differentiation between chemical and physical sorption as well as assessing their kinetics is crucial to evaluate material storage concepts and design of cathode active material handling and moisture management strategies. Figure 1.7 schematically shows a cathode exposed to humid atmosphere and the corresponding chemical reactions. However, sorption characteristics as a function of relative humidity, temperature, and time have only been addressed by a few studies to this point, which led to the third hypothesis.

Hypothesis 3: The reaction kinetics of NMC-622 with water and CO_2 determine the mass-uptake kinetics of this cathode active material.

Validating this hypothesis requires sorption experiments with active materials and electrodes. Differentiating the sorption mechanisms of water and CO_2 necessitates exposing the material to various artificial atmospheres. Additionally, a sorption set-up to probe multiple samples simultaneously must be established, to evaluate this hypothesis in long-term experiments. Further information about the sorption mechanisms will be obtained by assessing the temperature-dependent reversibility of the sorption. The following chapters address these subjects, focusing on the experimental setups in the next chapter.

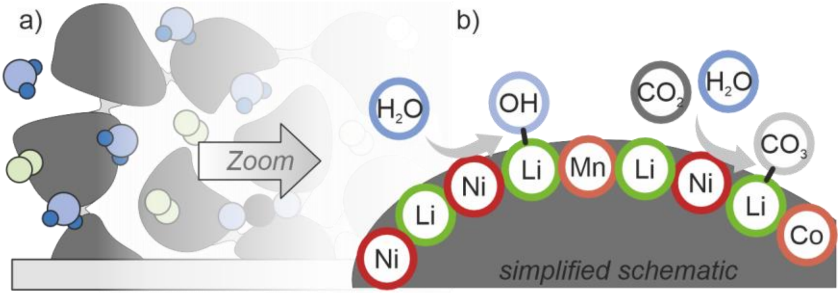

Figure 1.7: The schematic (a) shows the microstructure of a LiB cathode. During production it is exposed to air. The active material particles chemically bind components of the air to their surface. (b) shows simplified chemical sorption on the surface of an active material particle.

2 Materials and Methods

Addressing the aforementioned hypotheses require experiments, modeling and simulation. The modii and preparations of the sorption and drying experiments are explained in the following. The section “Materials” lists all the materials that were used throughout this study. The section “Sample holder” shows the sample geometries utilized for the experiments. The development of a sample holder that meets the requirements of a one-dimensional mass transport, while remaining below the weight limit of the sorption apparatus was also part of this study. The “experimental setup” section shows the various sorption apparatus, that provided data to assess the three hypotheses. This variety of sorption setups was extended by a setup that allows the controlled desorption/drying at defined pressures below atmosphere. The development of this setup is essential to investigate the post-drying at low pressure. Another sorption setup was established to observe the long-term exposure of cathodes to air.

2.1 Materials

Raw materials, electrodes and several fluids were used to conduct the sorption and drying experiments. All materials were used as received unless otherwise indicated.

Solids

Experiments were conducted with active materials as raw materials as well as electrodes. The cathode active material $LiNi_{0.6}Co_{0.2}Mn_{0.2}O_2$ (NMC-622, BASF SE, HED NCM-622 Al-doped) was used as received for sorption experiments in the form of raw material. A spherical graphite (SMGA, Hitachi Chemical Co. Ltd., Japan) was used for drying experiments in form of raw material as well.

The following materials were used to fabricate anodes for this study: A spherical and a non-spherical graphite (SMGA, Hitachi Chemical Co. Ltd., Japan), carboxymethyl cellulose (CMC, Sunrose MAC500LC, Nippon Paper industries, Japan), styrene-butadiene rubber (SBR, Zeon Europe GmbH, Japan), Polyvinylidene fluoride (PVDF, Solvay Solef 5130, Belgium), and carbon black (Super C65, Timcal, Switzerland).

Some cathodes were kindly provided by partners and were used as received. NMC-622 cathodes were fabricated as noted by Huttner et al., sealed in a pouch bag at inert atmosphere, and measured shortly after arrival (Huttner et al., 2021a). The same procedure was executed for the NMC-811 cathodes from Heck et al. (Heck et al., 2023).

Fluids

Gases provide the atmosphere for the sorption experiments in this study. The nitrogen originated from a liquid-nitrogen tank supplied by Air Liquide S.A. The dew-point temperature of this nitrogen ranges between -65 °C and -68 °C at the extraction point. This dew point was measured with a dew-point indicator “S8000 RS” by Michell Instruments. Throughout this study, the dew-point indicator “S8000” by the same company was also used. Pressurized air was supplied by an on-site apparatus. The dew-point temperature of the air stream at the extraction point varied seasonally between -40 °C and -60 °C. Due to this fluctuation, the dew point of the air stream was constantly monitored during experiments. Linde GmbH supplied the CO_2 (4.5) specified as 99.995% pure.

Liquids were used to provide a humidified atmosphere for sorption experiments and during electrode production. Salt solutions adjust a constant relative humidity for experiments described in chapter 6. This supersaturated salt solution was Strontium Chloride Hexahydrate (Carl Roth GmbH & Co. KG, Germany) and DI-water. N-methyl-2-pyrrolidone (NMP, Carl Roth GmbH & Co. KG, Germany, purity 99.8%) was used to dissolve PVDF during electrode production.

2.2 Sample holder

The hypotheses regarding mass-transport phenomena of this thesis can be verified by comparing experiments to a simulation. If the experiments match the expectation derived from the simulations, it indicates that the physics described by the simulation are correct. It is crucial that the restricting mass-transport resistance in the experiment is the one that is described by the simulation, to allow such conclusions. Therefore, the sample holders were developed and chosen as follows.

2.2.1 Sample holder for active materials

Active materials exchange Li-ions during the operation of a LiB and pose the largest weight-fraction of solids in an electrode. The sample holder for the post-drying experiments with the anode active material graphite must allow one-dimensional mass transport through a backfill of the graphite. The mass-transport distance (height of the backfill) must be large compared to other mass-transport distances to ensure the governing mass-transport resistance of the sample is the one of the backfill. The experimental procedure, disclosed in chapter 2.3.2, evokes several changes of pressure in the sample. This change of pressure limits the height of the backfill. If the height of the backfill is too large, the pressure change may remove material from the backfill, which makes the sample unusable. A glass tube, which has been sealed on one end, serves as the sample holder, as indicated in Figure 2.1.

The sample holder for the cathode active material for the sorption experiments is similar. However, it must fulfill other requirements. The mass-transport distance within the sample must be small to mitigate kinetic limitation in the gas phase of the sample. An estimate of the mass transport inside the sample is shown in appendix 8.11. However, the sample's mass must be sufficiently large to detect mass changes in the ppm range. Additionally, the sample holder must be sealable for safe transfer into the sorption apparatus. Glass vials were filled with the NMC-622 according to Figure 2.1. The transfer of the sample to sorption apparatus includes the handling and sealing of the glass vials in inert condition at the technical university Munich, transport to Karlsruhe, and placement in the sorption apparatus. A brief exposure to ambient air cannot be ruled out.

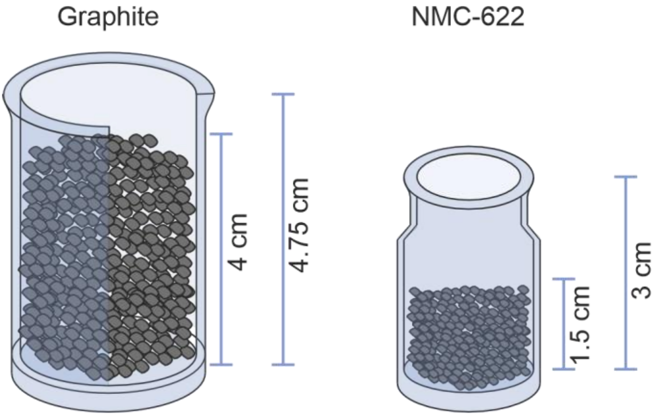

Figure 2.1: Two different sample holders were used to probe NMC and graphite. The left one is filled with graphite and allows one-dimensional mass transport through the porous structure. The right one is filled NMC-622. Both sample holders are made of glass.

2.2.2 Sample holder for electrodes

Anodes with the CMC/SBR-binder system were fabricated with the non-spherical graphite according to Kumberg et al. (Kumberg et al., 2019). The anodes with the PVDF-binder system were fabricated with spherical graphite according to Jaiser et al. (Jaiser et al., 2016). The composition of each anode is listed in Table 2.1. The anodes were coated onto copper substrate (CIVEN Metal, China). The electrodes were placed in a vacuum oven for three days to remove any excess solvent (NMP and water) from the anode. This extra drying step is necessary to reduce experimental time to determine a dry mass of the sample.

Table 2.1: Composition of the dry anodes.

Material	Unit	PVDF anode	CMC/SBR anode
Spherical graphite	wt-%	91.7	0
Non-spherical graphite	wt-%	0	93
Carbon black	wt-%	2.8	1.4
PVDF	wt-%	5.5	
CMC	wt-%	0	1.87
SBR	wt-%	0	3.73

The electrodes and active materials were characterized regarding parameters that are relevant for the mass-transport. The porosity was determined by measuring film thickness and area weight of the electrodes and calculation after Jasier et al. (Jaiser et al., 2017). The mean pore diameter was either measured via mercury intrusion pore size analyzer (PoreMaster 33, Anton-Paar, Österreich) or measured by Kumberg (Kumberg, 2022). The values are listed in Table 2.2. The data can be found in the appendix 8.1. The average pore diameter of the PVDF anode is smaller than the one of the CMC/SBR anode. This observation in combination with similar sized particles reflects in a difference in porosity.

Table 2.2: Overview of the mass-transport properties of the anodes.

Quantity	Unit	PVDF anode	CMC/SBR anode
Porosity	%	37	54
Mean pore diameter	µm	2.5	5[1]

[1] values from Kumberg (Kumberg, 2022).

For these measurements, these anodes have to be placed in a sample holder that must be able to hold enough of the anode’s active material to detect a change in mass on the scales. The upper weight limit of the scale (approx. 60 g) does not allow experiments with any kind of industrially wound daughter coils. Therefore, the geometry of such a coil must be abstracted. The mass transport through the sample must be guided through the porous structure of the anode. This is necessary to mimic the post-drying in coil format in a vacuum oven. After several iterations, the most suitable approach proved to be a compressed electrode stack. The anodes were cut, folded, and placed between two aluminum plates (Figure 2.2). The anodes were folded in a way that prevented a mass transport across the long side of the stack. The aluminum plates were perforated to reduce weight (not shown in Figure). The electrode stack was compressed with bolts and nuts. The samples were compressed until the total thickness of the compressed anode stack reached the thickness of the anode times the number of folds. The resulting compressed anode stack is impermeable on its long sides because of the copper foil. Both short ends of the anode stacks are open and allow mass transport. Therefore, the mass-transport distance of these samples is the half the length of the anode stack (4.25 cm for the PVDF anode stack and 4.0 cm for the CMC/SBR anode stack).

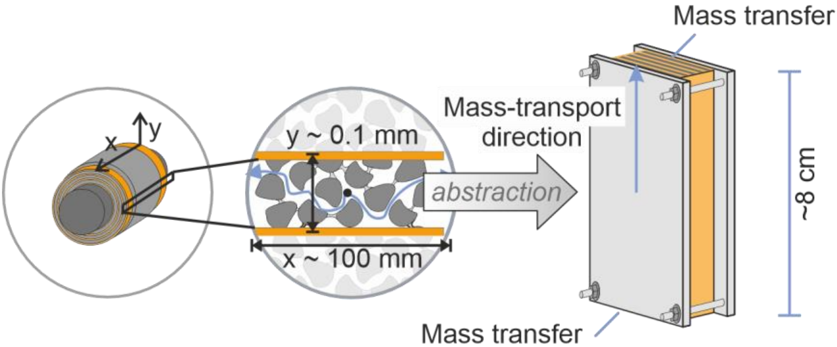

Figure 2.2: The mass transport of water through the porous structure of an electrode coil has an extended mass-transport distance through this porous structure. The left of the figure shows an anode coil with zoom to one layer of anode of the coil. Transferring this configuration into a sample suitable for the laboratory experiment resulted in compressed electrode stack of anodes. The layered electrode structure of the coil exists in the electrode stack.

2.3 Experimental setup

Experimental data of sorption and drying allow conclusions about sorption mechanisms, serve as model-validation, and yield sorption equilibria. Sorption data were obtained by various experimental setups. These setups range from manual ones, such as a desiccator and a scale, to highly automated ones, such as a magnetic suspension balance (MSB). In principle, the modus operandi is alike: gravimetrically detecting mass changes in controlled atmospheres until the mass is constant over a time interval. This procedure is repeated for multiple atmospheres, which gives a sorption isotherm. The magnetic suspension balance is flexible regarding temperature, pressure, and gas composition, but limited to probing one sample at the time. The advantage of the sorption in desiccators is a high throughput, which is especially handy to investigate slow sorption. However, compromises regarding temperature and pressure must be made.

If the detection of just moisture contents is required, the coulometric Karl-Fischer titration is widely applied in research and industry. Water is thermally desorbed from the sample and detected via amperometry in the titration solution. This measurement technique delivers quantitative results. However, depending on the water extraction from the sample, reservations can be held regarding the detection of the entire water content of the sample. Additionally, it is unsuitable to measure sorption equilibria, consider pressure dependencies, and obtain defined kinetic data.

Another experimental approach of this study is examining the mass-transport properties of various sample geometries in defined atmospheres below ambient pressure. A modification of a MSB setup was developed that enables the detection of such vacuum drying curves. In the following, the experimental setups for sorption and vacuum drying experiments are introduced.

2.3.1 Sorption

The magnetic suspension balance (IsoSORP SA, TA Instruments – Waters GmbH, Germany) is specialized for sorption experiments. This gravimetric measurement technique can probe reversible and irreversible sorption of various solvents. The MSB setup is fully automated, measuring isotherms at various temperatures. Schabel et. al. utilized a customized MSB to assess sorption equilibria of polymer-solvents systems (Schabel et al., 2003a). These measurements were conducted using the pure-vapor method. It has since been further customized to probe sorption behavior of LiB components (Eser et al., 2020b). This customization affects the periphery of the MSB, which will be discussed later.

Regardless of the customized periphery, the central piece of the setup remains the same: a scale on top of a measurement cell, connected via a magnetic suspension to a sample, as depicted in Figure 2.3.

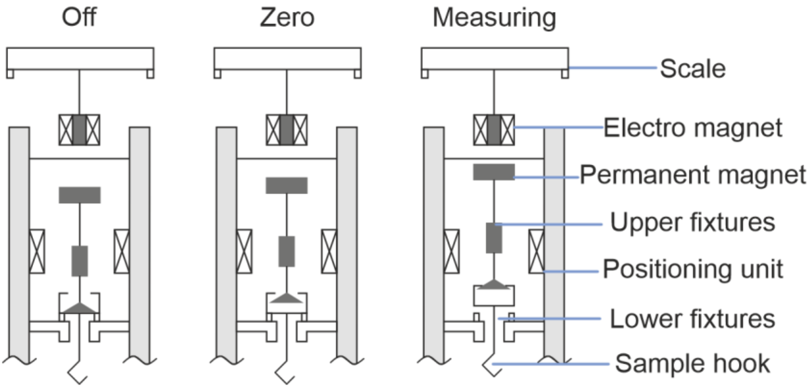

Figure 2.3: Schematic of the magnetic suspension balance. The scale is connected to a sample via a magnetic suspension. This setup enables the scale to remain unaffected by any temperature and pressure change in the measurement cell. The magnetic suspension allows the automated taring (zero) and measuring of a sample inside an isolated measurement cell.

This magnetic suspension connects the scale to a sample via several magnetic and mechanical elements. The scale is attached to an electromagnet. A permanent magnet as part of the "upper fixtures" is the counter piece to the electromagnet. These two components are the essentials of the magnetic suspension. The upper fixtures are mechanically clutched to the "lower fixtures”. Finally, the lower fixtures hook the samples. These elements have three arrangements to perform the weighing of the sample. In “**off**”-position the electromagnet is off and upper and lower fixtures rest on the dock. In this position the sample is mounted to the sample hook. The scale tares in the “**zero**” position, in which the electromagnet levitates the upper fixtures. The positioning unit controls the voltage of the electromagnet, to ensure the levitation of only the upper fixtures. The lower fixtures with the samples remain on the dock. The scale weighs the upper fixtures and tares. Periodically taring in zero position during an experiment corrects possible drift of the scale. This drift is a device-specific measuring uncertainty of the scale. In the “**measuring**” position, the electromagnet levitates both, upper and lower fixtures, and with the lower fixtures the sample as well. The scale now weighs the sample.

This configuration enables the scale to weigh samples, unaffected by pressure and temperature change in the measuring cell. However, pressure change affects the mass signal because the resolution of the scale is precise enough to detect a change in buoyancy force (compare, section: “Pure-vapor method”). In addition to the scale and magnetic suspension, a periphery provides the atmosphere inside the measurement cell. The requirements regarding the atmospheres are versatile for moisture management and post-drying research. Therefore, the periphery of the MSB is customized and adapted to meet these requirements. Two experimental setups of MSB for sorption experiments were used in combination with:

- the pure-vapor method,
- the perfusion method.

These methods are further discussed in the following. Additionally, a manual setup to conduct sorption experiments was established during the work of this thesis. This setup is introduced as well.

Pure-vapor method

The pure-vapor method uses vapor of a pure solvent to adjust the atmosphere in the measurement cell. This configuration provides experimental data to derive sorption isotherms and was established by Schabel (Mamaliga et al., 2004; Schabel et al., 2003a). The solvent enters the evacuated evaporator, which is temperature-controlled. The pressure inside the evaporator adjusts according to the liquid-vapor equilibrium of the solvent at the respective temperature. The sample is placed inside the temperature-controlled measurement cell. Prior to the sorption experiments, the mass of the sample holder and the mass of the dry sample are logged in vacuum ($p \sim 10^{-2}\ mbar$). The vacuum pump D8B (Leybold GmbH, Germany) evacuates the apparatus prior to the measurement.

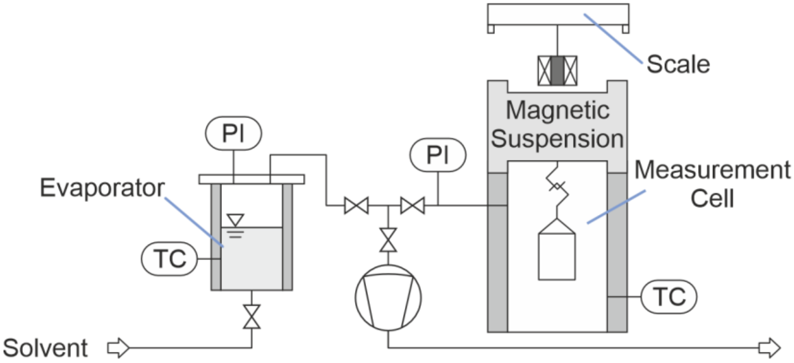

Figure 2.4: Component configuration of MSB with the pure-vapor method. A vacuum pump and an evaporator provide pure-solvent vapor in the measurement cell. Measurement cell and evaporator are temperature-controlled to adjust the solvent activity in the measurement cell.

The sorption experiments start by connecting measurement cell and evaporator. The solvent vapor fills the gas phase in the measurement cell and the sample sorbs solvent according to its sorption equilibrium. For a given solvent i, its gas phase activity a_i is a function of the evaporator temperature and the temperature inside the measurement cell, which is assumed to be equivalent to the sample temperature.

$$a_i = \frac{p_i^V\left(T_{Evaporator}\right)}{p_i^V\left(T_{Sample}\right)} \tag{1}$$

p_i^V is the vapor pressure of the solvent i. The Thermodynamics are discussed in section 3.1.1. As the activity of the solvent increases, the absolute pressure in the measurement cell rises as well. This results in an increasing Buoyancy force, detectable by the scale. This effect compromises the mass signal of the scale and must be corrected.

$$M_{Sample} = M_{Scale} + V_{Sample} \cdot \rho_{Gas} \tag{2}$$

The actual mass of the sample M_{Sample} is the sum of the scale's mass signal and weight of the displaced volume of the sample, according to equation 2. Depending on the pressure and the position of the lower and upper fixtures, the correction of the buoyancy force varies. The comprehensive post-processing necessary to account for the individual buoyancy of upper and lower fixtures during every sorption step can be found in the dissertation of Eser (Eser, 2021).

The pure-vapor method is used to determine sorption equilibria of a sample and every solvent in the theoretical activity range from 0 to 0.99. The lower limit is set by the minimal evaporator temperature and the upper limit by condensation within in the measurement cell. Each sorption step can also be analyzed regarding the sorption kinetics. The absence of any other gases in the measurement cell ensures that the mass-transport resistance during sorption is in the sample and not the gas phase. However, traces of inert gas may interfere with this assumption.

Perfusion method

Eser developed the perfusion method for the MSB inspired by Thurner et al. (Eser et al., 2020c; Thurner and Stietz, 1984). The additional gases air and CO_2 were added to the setup as part of this thesis, to investigate the sorption of cathode active materials that chemically bind CO_2. The atmosphere in the measurement cell is at ambient pressure and conditioned by mixing a water-saturated with an unsaturated gas stream, compare Figure 2.5. The combined, conditioned gas stream perfuses the measurement cell.

Air, N_2, and CO_2 supply the setup with gas. Each stream is flow-controlled by mass-flow controllers (MKS Instruments Deutschland GmbH, Germany). Air can replace nitrogen, which introduces, in addition to nitrogen, O_2 and CO_2 into the atmosphere. One Air/N_2 stream passes through a temperature-controlled saturator filled with water. The other stream enters the setup directly. Furthermore, CO_2 can be dosed into the gas stream in small quantities (200-2000 vol-ppm). The CO_2 concentration is calculated via the volume flow measured with the mass-flow controllers. A moisture indicator (MI) measures the dew-point temperature of this gas stream via a chilled-mirror dew-point indicator. The activity adjusts according to the dew-point temperature of the gas mixture and the temperature in the measurement cell, compare equation 3.

$$a_i = \frac{p_i^V(T_{DP})}{p_i^V(T_{Sample})} \tag{3}$$

It is assumed that the sample's temperature is equal to the temperature of the measurement cell. Details are discussed in section 3.1.2. Eser characterized the conditioning of the gas stream comprehensively (Eser, 2021).

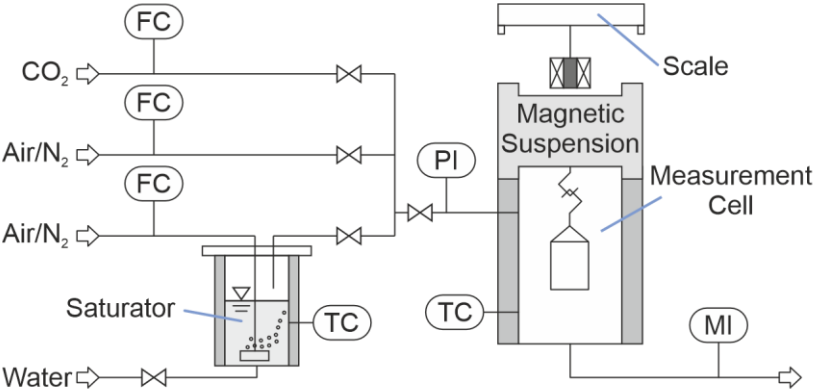

Figure 2.5: Component configuration of MSB with perfusion method. Nitrogen, air, and CO_2 can be used to perfuse the measurement cell. Mass-flow controllers mix these gases after saturating one gas stream at 19 °C. A dew-point indicator measures the water content of the gas-mixture after the cell.

The perfusion method covers the lower activity range between 0 % and 40 %. Especially, the precise adjustment of the dew-point temperature range of -50 °C to 0 °C which translates to an activity range of 0.1 % to 23 % at room temperature is an advantage of this setup. This range replicates the conditions present during the production of LiB. In contrast to the pure-vapor method, the sorption kinetics measured with this setup may be affected by the mass transport inside the sample and by the mass transport of the gas phase. Even though the sorption kinetics may differ depending on the MSB, the equilibrium is only a function of the solvent activity of the sample and therefore identical for both methods.

Sorption in desiccator

This manual setup to conduct sorption experiments has been described for example by Gnielinski (Gnielinski et al., 2013). It is, compared to the MSB setups, less flexible regarding activity range and temperature. However, the sorption in a desiccator can be parallelized – probing several samples in various atmospheres with a single scale, compare Figure 2.6.

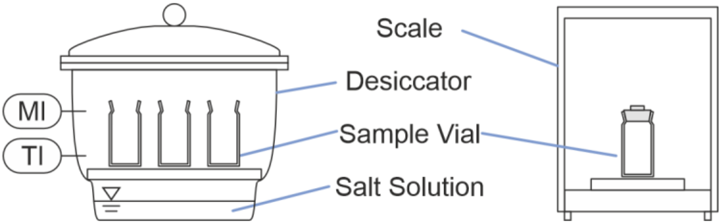

Figure 2.6: Outline of a desiccator used for sorption experiments. Temperature and moisture in the desiccator are monitored. The activity in the desiccator is adjusted by a supersaturated salt solution. Samples are placed in sample vials and periodically weighed on a high-precision scale.

Temperature and moisture inside the desiccator are logged during the experiments. The salt solution in the bottom of the desiccator is supersaturated and the relative humidity in the atmosphere above that salt solution adjusts according to the deliquescence point of the respective salt. On top of this salt solution sits a perforated disc, which allows the gas exchange within the desiccator. The samples are placed in sample vials that are sealable via ground joints. Vials and ground lids are labeled to counteract any mass fluctuations of the glassware. The sorption data are measured on a scale. Prior to weighing, the sample vials are sealed to avoid effects from the laboratory environment. The sealed sample vials are periodically weighed.

This setup is advantageous for long-term experiments with various samples. The mass-transport conditions inside the desiccator are undefined, therefore conclusion about mass-transport resistances must be drawn by comparing samples in the same desiccator. It is also advisable to investigate slow sorption processes (time scale ~ days), due to the manual measurement routine.

2.3.2 Vacuum drying

A new application for the MSB is tracking the propagation of vacuum drying. This method has been developed and established as part of this work. The periphery of the MSB was configurated to enable a constant perfusion at pressure below ambient pressure. A constant perfusion of the measurement cell avoids saturation of the gas phase during drying. The high resolution of the scale enables this setup to measure even the post-drying of electrodes, where the mass change is minimal. Figure 2.7 shows the MSB with the new periphery. As this setup was developed and optimized throughout this thesis, some experiments were conducted with a slightly different periphery. It will be annotated if this applies.

The flow- and temperature-controlled nitrogen stream enters through the bottom of the measurement cell. The samples hang in flow direction and must remain steady to obtain a clear mass signal. A rotationally symmetrical sample and an evenly distributed flow through the cell are therefore beneficial for a clear mass signal. The bed of glass spheres distributes the gas flow evenly across the cross section of the measurement cell. Experiments with larger mass flows through the cell (chapter 4) were conducted with the glass spheres. Experiments with smaller mass flows (chapter 5) were conducted with an aluminum diffusor on top of the gas inlet instead of glass spheres. Generally, the gas-spheres allow for higher volume flux through the cell, while keeping the samples steady. The pressure sensor indicates the pressure in the measurement cell during the drying. The pressure drop from the cell to pressure sensor is neglected.

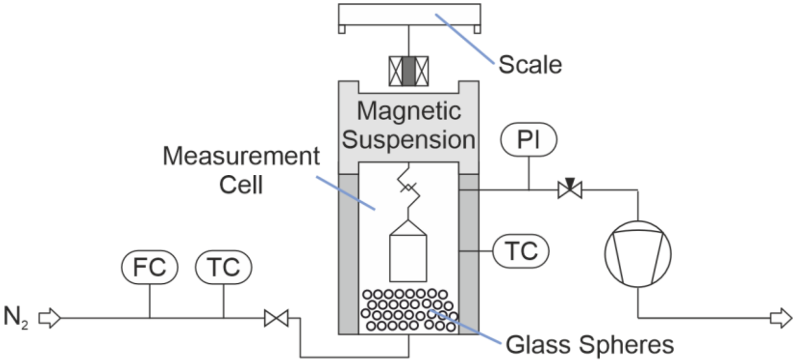

Figure 2.7: Component configuration of MSB with vacuum drying method. Nitrogen (dewpoint ≤ -65 °C) perfuses the measurement cell. The combination of a flow control prior to the measurement cell and a needle valve after the cell adjusts the pressure during the experiment. A vacuum pump provides vacuum.

The manual valve and the flow control prior to the gas inlet into the cell adjust the pressure in the measurement cell. The valve narrows the pipe, throttling the vacuum pump. The operation points of flow controller and valve were chosen to maximize nitrogen flux through the cell, while maintaining a stable mass signal from the scale. The operation points of the experiments are listed in Table 2.3. Due to the manual adjustment of the pressure, the pressure was not identical within the repeated measurements for each pressure. The range of each pressure is also listed in this table. The pressure was rounded to the first significant digit.

Table 2.3: Pressure settings for each vacuum drying experiment. The volume flow is given at each pressure.

Experiments from chapter:	5	5	4	5	5	5
Pressure rounded / mbar	800	400	200	100	40	20
Pressure range / mbar	808-817	408	209-218	100-110	40-43	20-22
Volume flux / liter/min	2.5	5.1	34	4.2	3.1	1.9
Retention time[1] / s	25	12	1,8	15	20	32

[1] The cell's volume is 1.04 liters.

The procedure to measure a vacuum drying curve starts with preconditioning the sample. All samples were preconditioned to obtain a defined starting point. The samples were exposed to vacuum at 90 °C until the mass was constant. After this preconditioning the cell's temperature was set to the temperature of the actual experiment while maintaining vacuum. Within one vacuum drying experiment the samples are exposed to various atmospheres. The scale detects a raw mass signal that is affected by these atmospheres during the experiment. This influence must be corrected to obtain a true mass over time. Figure 2.8 shows an exemplary mass signal in raw and corrected form. The raw mass signal is classified into intervals from "I1" to "I5". Each interval requires unique corrections.

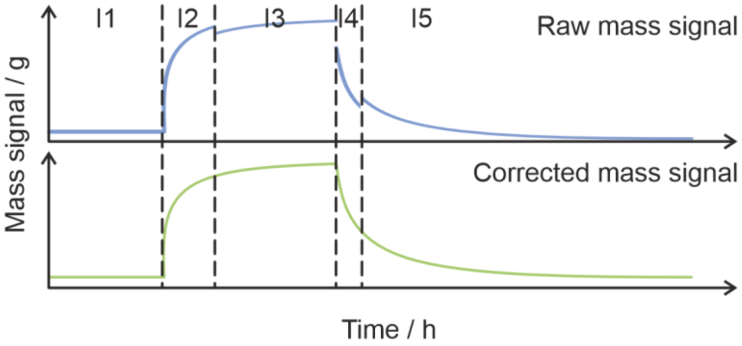

Figure 2.8: Raw mass signal of the vacuum-drying procedure in comparison to the corrected mass signal. Buoyancy and drag force affect the mass signal. This effect must individually be considered depending on the interval “I” of the experiment.

Generally, two forces affect the mass signal and must be corrected. The buoyancy force of the gas in the cell (compare chapter “Pure-vapor method”), and the drag force from the gas flow. In the first interval (I1), the sample is exposed to vacuum at the experiment’s temperature. The mass signal in I1 must not be corrected due to the absence of any gas and flow in the cell. The pure-vapor method is applied during I2 and I3, which provides a repeatable mass loading as starting point for the vacuum drying. This is necessary to obtain similar mass loadings of the samples in the ppm range, to make the vacuum drying curves comparable. The transition from I2 to I3 occurs at the first taring after the pressure change in the cell. The difference between I2 and I3 is a shift in the mass signal, which originates from the taring in zero position of the scale (compare Figure 2.3) at the new pressure. This taring corrects the buoyancy force from the upper fixtures. If gas fills the cell while the scale is in measuring position, the new buoyancy force affects the sample, the lower, and the upper fixtures of the magnetic suspension. The mass signal within the intervals I2 and I3 must be corrected via this buoyancy correction.

After I3, the vacuum drying begins abruptly. While measuring the weight of the sample, the atmosphere changes to the dry nitrogen that perfuses the measurement cell. This change in atmosphere evokes the desorption of the sample. I4 and I5 represent the part of the experiment that is referred to as vacuum drying. During these intervals the buoyancy and drag correction must be applied. The difference between I4 and I5 is the buoyancy force of the upper fixtures, the same as the difference between I2 and I3. The buoyancy force is always corrected via calculation in I4 and I5. Any efforts to calculate the drag force from geometry parameters were unsuccessful. Therefore, the drag force had to be derived from the experimental data individually for every flow setting. The difference of the dry mass from measurements at every flow setting to the dry mass from I1 can then be attributed to the drag force of the nitrogen flow. One experiment takes between 48-96 h from preconditioning to finish.

The vacuum-drying experiments of chapter 4 were repeated twice, to show repeatability of the experiments. The results are plotted in appendix Figure 8.2 and Figure 8.3. Individual experiments of the vacuum-drying experiments of chapter 5 were conducted twice to show repeatability of the measurement setup. The results are plotted in appendix Figure 8.4. In every case, the experiments showed sufficient reproducibility.

This novel procedure is to the author’s knowledge the only method to obtain time-resolved vacuum-drying curves of LiB materials and electrodes with repeatable starting points. The precision of the MSB allows the detection of mass changes in the ppm-range, which makes this procedure suitable to investigate post-drying of LiB. The following chapter gives the theory of sorption and mass transport. This theory is relevant to experiments described in this chapter and to evaluate the hypotheses in the upcoming result chapters.

3 Phase equilibria and mass transport

The equilibrium of the electrodes and the production atmosphere is the pivotal point of moisture management. The same applies to the electrode and the atmosphere in the post-dryer. These equilibria are regarded as sorption equilibria. Empirical equations and equations of state model these equilibria. A change in process conditions, e.g. temperature and humidity, evokes a shift of the thermodynamic equilibrium. Mass-transport kinetics describe the non-equilibrium period between two thermodynamic equilibria. Figure 3.1 shows some examples of phase equilibria (green) and kinetic phenomena (orange) that are relevant to this work.

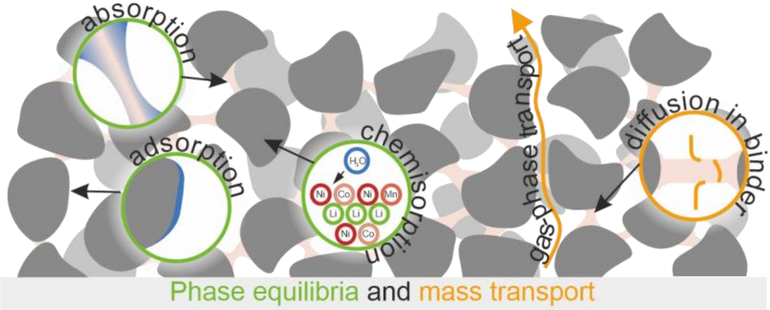

Figure 3.1: Examples of phase equilibria and mass-transport phenomena that occur during moisture management and post-drying of battery electrode.

Kinetic limitations may occur in different phases. For example, the binder CMC absorbs a significant amount of water with a kinetic that depends on the water content of the binder (Eser et al., 2020a). The gas-phase mass transport is affected by temperature and pressure and influences the post-drying in coil format (Huttner et al., 2021b). Considering cathode active materials, reaction kinetics may govern the chemical sorption of CO_2 and water. The following describes the fundamentals to these examples that are relevant for the experiments and results of this thesis.

3.1 Phase equilibria

A phase is a homogenous part of a system. At equilibrium, all intensive state variables within that phase are at equilibrium (Stephan et al., 2013). Multiple phases may coexist in a system and interact with each other. The gas-liquid phase equilibrium is relevant for the experimental setups. The gas-solid phase equilibrium (sorption equilibrium) adjusts between battery components and their surrounding atmosphere. Two phases are equilibrated, if the state variables in both phases are constant over time and space. Considerations in this thesis are mostly at isothermal and isobaric conditions. This thesis focuses on mass transport and sorption, which is driven by the chemical potential. Therefore, the following chapter discusses the chemical equilibrium.

3.1.1 Gas-liquid phase

A system of a gas and a liquid phase is in its chemical equilibrium if the chemical potential in both phases is identical and constant. If the liquid is pure, ideal, and equilibrated with its vapor phase, its chemical potential can be described via its vapor pressure (Stephan et al., 2010).

$$\mu_i^l = \mu_i^g = \mu_i^+ + R \cdot T \cdot \ln\left(\frac{p_i}{p^+}\right) \tag{4}$$

$\mu \left[\frac{J}{mol}\right]$ – chemical potential
$R \left[\frac{J}{mol \cdot K}\right]$ – gas constant
$T\ [K]$ – temperature
$p\ [Pa]$ – pressure

The chemical potential of the species i in the liquid phase l and gas phase g is a function of the reference state $+$ and the gas constant, temperature and the partial pressure p_i and the reference pressure p^+. This equation assumes that the vapor gas phase is an ideal gas (Stephan et al., 2010).

Activity describes the real behavior of a liquid fluid mixture such as polymer and solvent, as follows (neglecting the fugacity):

$$a_i = \frac{p_i}{p_i^V(T)} \tag{5}$$

a_i $[-]$ – activity component i
p_i $[Pa]$ – partial pressure component i
p_i^V $[Pa]$ – vapor pressure component i

The activity of the liquid fluid mixture can be described via quantities of the gas phase above this mixture, if the two phases are at equilibrium. Applied to the liquid vapor system, p_i is the partial pressure above the fluid mixture and the p_i^V is the vapor pressure (Stephan et al., 2010). These equations apply to the saturator and evaporator of the experimental setup (compare chapter 2.3.1). The concept of activity only applies to the samples in the measurement cell, if they are fluids e.g., polymer-solvent mixtures.

Deliquescence

If the liquid is a super-saturated salt-water solution, the activity above that solution is constant if the solution is either super-saturated or saturated (Gnielinski et al., 2013). The value of this activity is a substance property of the salt (Rockland, 1960; Rörig-Dalgaard, 2021). This feature of a salt solution can be used to create defined humid environments for sorption experiments.

3.1.2 Gas-solid phase

Molecules from a gas phase adhere to surfaces of solids according to their sorption equilibria (Butt et al., 2003). At this thermodynamic equilibrium the chemical potential of an adhered molecule is the same as the chemical potential of a molecule in the gas phase. This chemical potential can be derived from the kinetic gas theory. The binding mechanism between sorbate (adhering molecule) and sorbent (solid phase) categorizes the sorption into physical and chemical sorption. The number of molecules that adsorb to the surface is a function of the sorption energy, relative pressure of the sorptive, and temperature. The sorption energy varies for each sorption spot and may change with the amount of sorbate on the surface (sorption spots with less sorption energy are favored). Isotherms display the amount of sorbate for one temperature as a function of relative pressure (Butt et al., 2003).

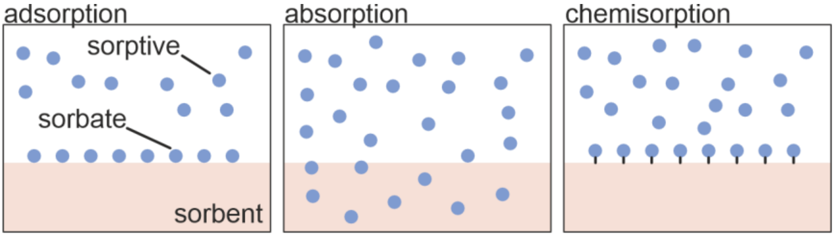

Figure 3.2: Illustration of the physical sorption mechanisms adsorption and absorption as well as chemical sorption (chemisorption). The binding mechanism differentiates between chemical and physical sorption. Whether the sorbate enters the bulk of a material distinguishes adsorption from absorption.

Relative pressure

The relative pressure, or relative vapor pressure quantifies the influence of the sorptive in a system (Butt et al., 2003). In the case of water, the relative pressure times 100 is identical to the relative humidity:

$$RH = \frac{p_w}{p_w^V} \cdot 100 \tag{6}$$

RH [%] – relative humidity
p_w $[Pa]$ – partial pressure of water
p_w^V $[Pa]$ – vapor pressure of water

The partial pressure of water p_w is divided by the vapor pressure of water p_w^V at a given temperature. The RH can be used if the sorption is studied in a pure vapor environment as present in the pure vapor method (compare section 2.3.1). If other species are present in the gas phase as well, the RH can be used under the assumption that the other species do not alter the RH and the gases behave ideal.

Scott suggested that the “Water activity is, at a given temperature, the ratio of its fugacity, f_w, in a system and the fugacity, f_w^0, of pure liquid water at the same temperature." (Reid, 2007; Scott, 1957). The fugacity is a fictional partial pressure in a real fluid mixture. Assuming ideal gas conditions yields equation 5.

Physical adsorption

Molecules that physically adsorb to a surface are attracted to this surface by van der Waals forces with a sorption energy of ~ 20 to 40 kJ/mol (Butt et al., 2003). The structure of the sorbent remains unchanged if the molecules stick to the surface.

Isotherms can be modeled and experimentally determined. Experimental data adjust the parameters of the models to replicate the experiments. IUPAC classified sorption isotherms according to their shape (Sing, 1982). The simplest isotherm form is a straight, the Henry adsorption equation (Henry, 1803; Kalam et al., 2021). A sorption constant correlates relative pressure and sorbate loading in sorbent (Henry, 1803; Ruthven, 1984). This isotherm is valid for either low sorbate loadings or small intervals of relative pressure. If suitable, equation 7 was used to approximate sorption equilibria.

$$X_w = K_w \cdot \frac{p_w}{p_w^V} \tag{7}$$

X_w $[-]$ – water loading on sorbent
K_w $[-]$ – sorption constant
p_w $[Pa]$ – partial pressure of water
p_w^V $[Pa]$ – vapor pressure of water

Describing sorption isotherms of heterogenous surfaces, as present in battery components for example, requires more sophisticated models. These models consider sorption spots with different energy levels and allow multilayer sorption. Based on the model of Langmuir, Brunauer, Emmett, and Teller derived the BET isotherm that is widely applicable (Brunauer et al., 1938; Langmuir, 1918; Ruthven, 1984). This isotherm is a function of the specific sorbent surface, and another fitting parameter. The BET-surface indicates how much surface per mass sorbent can be occupied by sorbate. Brunauer et al. provided an advanced model (equation 8), which was used in this study (Brunauer et al., 1940). Do and Eser provide more detail on sorption isotherm modeling (Do, 1998; Eser, 2021).

$$X_w = \frac{X_m \cdot k_{BET} \cdot \frac{p_w}{p_w^V}}{1 - \frac{p_w}{p}} \cdot \frac{1 + \left(n \cdot \frac{g}{2} - n\right) \cdot \left(\frac{p_w}{p_w^V}\right)^{n-1} - (n \cdot g - n + 1) \cdot \left(\frac{p_w}{p_w^V}\right)^{n} + \left(n \cdot \frac{g}{2}\right) \cdot \left(\frac{p_w}{p_w^V}\right)^{n+1}}{1 + (k_{BET} - 1) \cdot \frac{p_w}{p_w^V} + \left(k_{BET} \cdot \frac{g}{2} - k_{BET}\right) \cdot \left(\frac{p_w}{p_w^V}\right)^{n} - k_{BET} \cdot \frac{g}{2} \cdot \left(\frac{p_w}{p_w^V}\right)^{n+1}} \tag{8}$$

$X_w\ [-]$ – water loading on sorbent
$X_m\ [-]$ – water loading on sorbate as monolayer
$k_{BET}\ [-]$ – temperature dependent parameter
$g\ [-]$ – temperature dependent parameter
$(2n-1)\ [-]$ – number of sorbate layer
$p_w\ [Pa]$ – partial pressure of water
$p_w^V\ [Pa]$ – vapor pressure of water

Physical absorption

After attaching to the surface of a sorbent, the sorbate may enter the bulk of the sorbent. This absorption occurs in many polymer-solvent systems (Gracia-Medrano-Bravo et al., 2021; Saure, Schlünder, 1995; Schabel et al., 2003b; Scharfer et al., 2008). In contrast to adsorption, the sorbent and sorbate merge into one thermodynamic phase, which can be regarded as a liquid mixture. Flory and Huggins presented a model for polymer-solvent systems (Flory, 1942; Huggins, 1942). Vrentas and Vrentas advanced this model to account for glass-transition effects of polymers (Vrentas and Vrentas, 1996, 1991). The Flory-Huggins theory is commonly applied to polymer-solvent systems and has been used to describe the interaction of binder systems of LiB and their solvents (Eser, 2021). The kinetics of this sorption process can be limited by the diffusion of the sorbate into the polymeric sorbent, with solvent-concentration-dependent diffusion coefficients (Schabel et al., 2004). Even the dimensions of the sorbent affect the mechanism of this kinetic limitation. Börnhorst showed that the thickness of a polymeric film determines whether relaxation of the polymer structure or the diffusion of the sorbate governs the sorption (Börnhorst, 2021).

Chemical sorption

Compared to physical sorption, chemical sorption forms a stronger bond between sorbate and sorbent ~ $100 - 400$ kJ/mol (factor ten compared to physical sorption) (Butt et al., 2003). The surface of the sorbent structurally changes during this sorption, due to the chemical reaction. Chemisorption can be either dissociative or molecular, depending on the structure of the sorbate after the reaction. Water as a sorptive may also evoke the formation of hydrates in sorbents. Species such as LiOH form a mono hydrate (Thakker et al., 1968; Williams and Miller, 1970). Once the previously discussed equilibrium states are disrupted, a system equilibrates again, following kinetics. Some of these possible kinetics are presented in the following.

3.2 Gas-phase mass transport

A change of the chemical potential at a permeable boundary of a system evokes mass transport across that boundary and within a system. Kinetic equations describe this non-equilibrium state via gradients, expressed by derivates of e.g. the chemical potential, and the concentration over a space coordinate. Fick's law (equation 9) describes these kinetics via diffusion coefficients and the concentration gradient (Crank, 1975; Fick, 1855). Fick's law is used to describe mass transport in this thesis.

$$\dot{n}_i = -D_{i,j} \cdot \frac{\partial C_i}{\partial x} \tag{9}$$

$\dot{n}_i \left[\frac{mol}{m^2 \cdot s}\right]$ – areal molar flux of component i
$D_{i,j} \left[\frac{m^2}{s}\right]$ – diffusion coefficient of i in j
$C_i \left[\frac{mol}{s}\right]$ – concentration of component i
$x\ [m]$ – space coordinate

The areal molar flux is a function of the diffusion coefficient and the concentration gradient over the space coordinate. It is assumed that ideal gas conditions apply. If the concentrations are small enough, the mass transport can be described solely by diffusion and the integration of equation 9 yields a linear kinetic in the gas phase. If the concentration of the diffusion component is large enough that drag effects must be considered, a convection term accounts for these effects, which results in logarithmic gas-phase kinetic.

3.2.1 Mass transport in the gas phase of porous media

Pores may be randomly oriented and sized inside the porous media as is the case for battery electrodes (Froboese et al., 2017). This structure must be accounted for, to describe this gas-phase mass transport adequately. If the pore-size distribution is sufficiently large, various diffusion mechanisms may occur in the structure of an electrode. Furthermore, concentration gradients of each pore differ according to the pore's property and position. Considering these effects either requires a 3D model of the pore structure or statistically averaging the concentration quantities across the porous media. Statistical averaging of concentration quantities across the volume of the porous media reduces the complexity of modeling its mass-transport phenomena to solving one-dimensional equations of a porous bulk phase (Burganos, 1998; Burganos and Sotirchos, 1987; Kärger et al., 2012; Vu and Tsotsas, 2018; Whitaker, 1999). Volume averaging is used to model the mass transport in the gas phase of the porous media. Porosity and tortuosity simplify the structure of the porous media to scalars, to incorporate the structure into the one-dimensional equations.

Porosity

The porosity separates the volume of a system into a solid and a fluid phase (compare equation 10). The porosity weighs the transport and accumulation terms of both phases by their average appearance in the system. This consideration presupposes that the volumes of both phases are homogeneously distributed across the considered system. This concept is also applied to differentiate the micro and macro scale, see chapter 3.3.2.

$$V_f = V \cdot \varepsilon \tag{10}$$

$$V_s = V \cdot (1 - \varepsilon)$$

$V\ [m^3]$ – volume

$\varepsilon\ [-]$ – porosity

Tortuosity

The tortuosity accounts for the elongation of the mass-transport path due to curvature of pores. This effective length of the pore deviates from the length of a system, compare Figure 3.3. This Figure shows the elongation of the mass-transport distance resulting from the structure of a battery electrode. The comparison of either the straight capillary or the effective length to the length of the system gives the definition of the geometric tortuosity (equation 11).

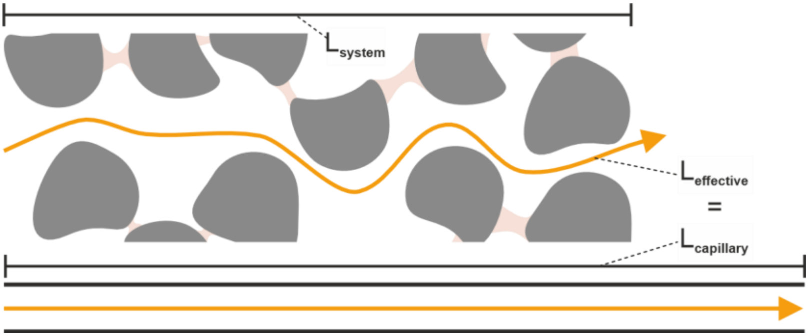

Figure 3.3: Illustration of the mass-transport distance in a porous structure versus a straight capillary of the same distance in mass-transport direction. The fraction of these two distances is the geometric tortuosity.

Tortuosity is complex and affects heat and mass transfer as well as electrical properties of porous media (Landesfeind et al., 2016; Oehler et al., 2020; Tsotsas and Martin, 1987; Zehner and Schlünder, 1973). Experimental determination of tortuosity is difficult; therefore, an abundance of correlations and simulation approaches exists to assess a media’s tortuosity.

$$\tau_{geometric} = \frac{L_{capillary}}{L_{system}} = \frac{L_{effective}}{L_{system}} \tag{11}$$

$\tau_{geometric}$ $[-]$ – geometric tortuosity

L $[m]$ – length

For flow and diffusion through porous media, the geometrical tortuosity and the tortuosity factor must be distinguished (Epstein, 1989). This distinction is necessary to remain mathematically correct. It is, however, irrelevant if the tortuosity is a fit parameter. Henceforth, the quantity referred to in equation 12 as τ is the tortuosity factor. τ equals to the geometric tortuosity squared, derivation see appendix 8.3. The diffusion coefficient of Fick's law is indexed as "effective" and accounts for these characteristics.

$$D_{eff,i,j} = \frac{\varepsilon}{\tau} D_{i,j} \tag{12}$$

$D_{(eff),i,j}$ $\left[\frac{m^2}{s}\right]$ – (effective) diffusion coefficient of i in j
τ $[-]$ – tortuosity
ε $[-]$ – porosity

The common correlations used in this study are from Zehner-Bauer-Schlünder (ZBS), Maxwell, and Brueggemann, listed respectively in equations 13-15 (Bruggeman, 1935; Maxwell, 1873; Neale and Nader, 1973; Tsotsas and Martin, 1987; Zehner and Schlünder, 1970):

$$\text{ZBS: } \frac{\varepsilon}{\tau} = 1 - \sqrt{1-\varepsilon} \tag{13}$$

$$\text{Maxwell: } \frac{\varepsilon}{\tau} = \frac{2 \cdot \varepsilon}{(3-\varepsilon)} \tag{14}$$

$$\text{Bruggeman: } \frac{\varepsilon}{\tau} = \varepsilon^{1.5} \tag{15}$$

3.2.2 Diffusion regimes

The characteristics of a gas-phase mass transport depend on temperature, pressure, and structure of a system. Depending on the gas-density, the physics of this mass transport change, which is categorized in regimes (Chambre and Schaaf, 1961; Kennard, 1938; Tsien, 1946). The Knudsen number Kn indicates whether molecules either predominately collide with the other molecules or predominately collide with the walls of the system. In the case of this thesis, this system is the porous structure of LiB electrodes. Figure 3.4 illustrates the diffusion regimes and shows the respective Kn range for each regime. The boundaries of these ranges are not sharp cut-offs and rather smooth transitions.

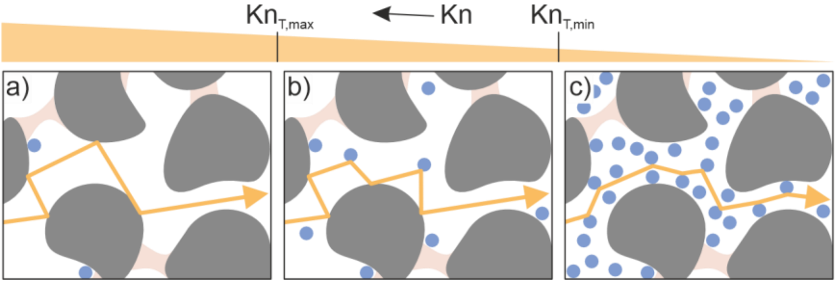

Figure 3.4: Diffusion regimes as a function of the Knudsen number. The transition Knudsen numbers $Kn_{T,max}$, $Kn_{T,min}$ are known for straight capillaries. However, they may vary as a function of the pore structure (refer to discussion in section "Transition regime" below). Molecules predominately collide – with the walls in the Knudsen regime (a) – with other molecules in the Stefan regime (c) – and with both in the transition regime (b).

The diffusion in the discontinuous molecular flow, called Knudsen diffusion, is the regime where molecules mostly collide with the solid boundaries of the porous structure. At the other end of the spectrum, the diffusion in the continuous viscous flow, here called Stefan diffusion, is the regime where molecules mostly collide with each other. In between is a transition region, where both regimes influence the diffusion (Do, 1998; Kärger et al., 2012). The Knudsen number (equation 16) quantifies the intensity of the interaction between molecules in the gas phase and with the wall (Schlünder, 1996), which determines the diffusion regime.

$$Kn = \frac{\Lambda_i}{L_C} \tag{16}$$

$Kn\ [-]$ – Knudsen number
$\Lambda_i\ [m]$ – mean free path substance i
$L_C\ [m]$ – characteristic length

The mean free path is the distance a molecule travels before colliding with another molecule (equation 17). The characteristic length is a representative geometric quantity of the porous structure, often the pore diameter. If the characteristic length is in the same order of magnitude as the mean free path, the collision probability between molecule-molecule and molecule-wall is equally likely. Temperature, pressure, molecule-, and pore-size determine the diffusion regime.

$$\Lambda_i = \frac{1}{\sqrt{2} \cdot \pi \cdot \sigma_i^2 \cdot \tilde{\rho} \cdot N_A} \tag{17}$$

Λ_i $[m]$ – mean free path component i

σ_i $[m]$ – diameter of molecule i

$\tilde{\rho}$ $\left[\frac{mol}{m^3}\right]$ – ideal gas pressure

N_A $\left[\frac{1}{mol}\right]$ – Avogadro-constant

Knudsen diffusion

If molecules do not interact with each other, they travel at their molecular speed in one direction until they hit an obstacle. The diffusion coefficient for this diffusion mechanism can be derived by a force balance of a molecule. The mean velocity of a molecule in positive x-direction is $1/4 \cdot \bar{c}_v$, which originates from the kinetic gas theory (elaboration see appendix 8.4) (Langmuir, 1913). Therefore, the diffusion coefficient is the product of the pore radius, a factor and the mean molecule velocity (compare equation 18) (Kärger et al., 2012). The Knudsen diffusion mechanism is not a function of pressure, weakly dependent on temperature (compared to continuum diffusion), and the molecular weight.

$$D_i = \frac{1}{3} \cdot r_{pore} \cdot \bar{c}_v \tag{18}$$

D_i $\left[\frac{m^2}{s}\right]$ – diffusion coefficient component i

$\bar{c}_v$ $\left[\frac{m}{s}\right]$ – mean molecule velocity

r_{pore} $[m]$ – pore radius

Stefan/Fickian diffusion

Models that describe diffusion in the continuum describe the interaction between molecules. Derivations from the Stefan-Maxwell hard-sphere model predict the diffusion coefficient in gases. However, these models offer limited accuracy, due to real temperature and pressure effects in gases (Fuller et al., 1966). Fuller, Schettler, and Giddings suggested a semi-empirical equation based on the hard-sphere model which predicts a binary gas diffusion coefficient (Fuller et al., 1966). They provide the empirical volumes as well (Fuller et al., 1969)[6]. It is based on temperature, pressure, and molecule properties. Equation 19 shows a modified version of this equation for pressure in bar (Stephan et al., 2019).

$$\frac{D_{i,j}}{m^2/s} = \frac{0.01^2 \cdot 0.00143 \cdot \left(\frac{T}{K}\right)^{1.75} \left[\left(\frac{\widetilde{M}_i}{g/mol}\right)^{-1} + \left(\frac{\widetilde{M}_j}{g/mol}\right)^{-1}\right]^{0.5}}{\frac{p}{bar} \cdot \sqrt{2} \left[(\sum \Delta v_i)^{\frac{1}{3}} + (\sum \Delta v_j)^{\frac{1}{3}}\right]^2} \tag{19}$$

$D_{i,j}\ \left[\frac{m^2}{s}\right]$ – diffusion coefficient component i in j

$T\ [K]$ – temperature

$p\ [bar]$ – pressure

$\widetilde{M}\ \left[\frac{g}{mol}\right]$ – molar mass

$\Delta v\ [-]$ – empirical diffusion volume

Transition regime

The transition between Stefan and Knudsen diffusion occurs around a Knudsen number of one. This transition is not abrupt but rather a range where discontinuum and continuum overlap. The model and data in Figure 3.5 show an example from heat transfer. It shows the span across both regimes influence the heat conduction in a porous structure made of spheres (Bauer, 1977).

---

[6] The diffusion volumes from Fuller et al., 1966 were adjusted in their publication Fuller et al., 1969.

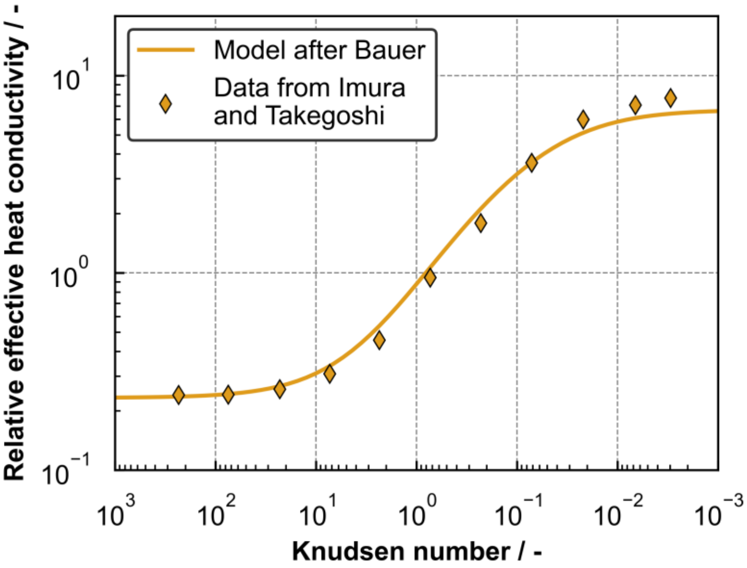

Figure 3.5: Influence of the Knudsen number on the relative effective heat conductivity of a packed bed of spheres, model after Bauer and data from Imura and Takegoshi (Bauer, 1977; Imura and Takegoshi, 1974). The heat conductivity is independent of the flow regime for Knudsen numbers of above ~ 100 and below 0.01. In between is a transition region where the heat conductivity decreases with increasing Knudsen number.

The heat conductivity of this packed bed is a function of the flow regime of the gas in the voids. The change of regimes starts to affect the conductivity at a Knudsen number of 0.01. The transition is finished at a Knudsen number of 100. Kärger suggests to account for this effect in mass transport around a Knudsen number of one (Kärger et al., 2012). The voids of a porous structure made of spheres are non-uniform with a pore-size distribution. Theoretically this distribution results in a distribution of the Knudsen number and broadens the influence of the diffusion regimes.

The similarity of heat and mass transfer suggests that similar phenomena occur during the diffusion of molecules through the porous structure of a battery electrode. The Bosanquet-equation (equation 20) was derived by Pollard and Present for long straight capillaries for diffusion in between the Knudsen and Stefan flow regimes (Pollard and Present, 1948). This model was originally proposed by Bosanquet in a classified report (Bosanquet, 1944). A modification to this equation is proposed and discussed in chapter 5, to account for the influence of non-uniform pore structure in porous media.

$$\frac{1}{D_{i,j,transition}} = \frac{1}{D_{i,j,Stefan}} + \frac{1}{D_{i,Kudsen}} \tag{20}$$

3.3 Equations of mass transport in porous structures during sorption

Partial differential equations (PDE) with time and space derivatives describe the mass transport in a system. Diffusion is regarded as the primary mass-transport mechanism during the experiments presented in this thesis. Combining the sorption equilibrium with the kinetics via the conservation of mass yields the differential equations that describe the mass transport of sorption as a function of time and space. These equations can be derived by balancing a substance that is transportable across the boundaries of this system. If the dimensions allow reducing the mass transport to one dimension, the differential form of this balance is given as follows:

$$\frac{\partial C_i}{\partial t} = D_{i,j} \frac{\partial^2 C_i}{\partial z^2} \tag{21}$$

$C_i \left[\frac{mol}{m^3}\right]$ – concentration component i

$t\ [s]$ – time

$D_{i,j} \left[\frac{m^2}{s}\right]$ – diffusion coefficient component i in j

$z\ [m]$ – space coordinate

This equation describes the concentration of component i over time and space. Equation 21 is valid in one dimension for isotropic media with a concentration-independent diffusion coefficient. A detailed derivation can be found in Crank (Crank, 1975). If the diffusion coefficient varies within the system, it must be differentiated in z-direction, as is the case in polymer/solvent systems (Eser et al., 2020a; Merklein et al., 2021; Schabel et al., 2003b; Scharfer et al., 2008).

This equation requires two boundary conditions and one initial condition to be solved (Schiesser and Griffiths, 2009). For most applications, the initial condition is the concentration at $t = 0$. The boundary conditions depend on the application and location of the phase boundary. The three options are:

1. *Dirichlet*: specifying the dependent variable. For example, if a solid and gas phase are at their sorption equilibrium.
2. *Neumann*: specifying the derivative of the dependent variable. For example, the gradient of the concentration is zero at a mass-transport barrier.
3. *Robin*: specifying the variable and its derivative in one term. For example, a flux at the phase boundary that is a function of the dependent variable.

Equation 21 has an analytical solution for constant coefficients (Crank, 1975; Kärger et al., 2012). However, if applied to real physical phenomena, these coefficients may depend on time and current concentration in the system. Accounting for these dependencies requires numerical methods to solve equation 21 (Scharfer, 2009). These methods approximate the analytical solution, which suffices for most scientific applications. In the following, Equation 21 is applied to phenomena during post-drying and moisture management. This application requires a modification of the accumulation and kinetic terms.

3.3.1 Mass transport in adsorbing systems

Equation 21 can describe the mass transport in a system that contains two phases. Applied to an electrode, these phases are the gas phase in the porous structure and the solid phase of the electrode components. They interact via adsorption of sorptive onto the surface of electrode components, which occurs during the post-drying and moisture management, (Eser et al., 2020a), compare Figure 3.6.

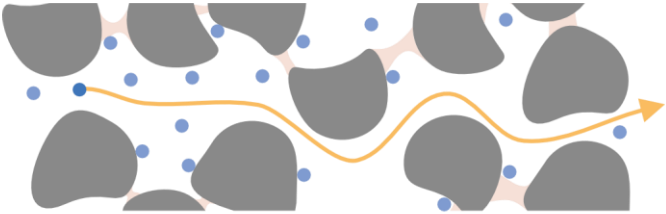

Figure 3.6: Outline of the mass transport in an adsorbing system. The dark blue molecule travels through the gas phase of the structure. The equations must account for accumulation in the gas and solid phase. The gas-phase mass transport is considered to be the dominant compared to the one on the solid's surface.

The porosity ε separates the volume of the system into the volumes solids (s) and gas (g), to mathematically consider both phases individually. This separation yields accumulation and kinetic terms for solid and gas phase.

$$\varepsilon \frac{\partial C_{i,g}}{\partial t} + (1-\varepsilon) \frac{\partial C_{i,s}}{\partial t} = \varepsilon \cdot D_{i,j} \frac{\partial^2 C_{i,g}}{\partial z^2} + (1-\varepsilon) \cdot D_{i,s} \frac{\partial^2 C_{i,s}}{\partial z^2} \qquad (22)$$

$C_i \left[\frac{mol}{m^3}\right]$ – concentration component i in gas and solid phase

$t\ [s]$ – time

$\varepsilon\ [-]$ – porosity

$D_i \left[\frac{m^2}{s}\right]$ – diffusion coefficient component i in gas and solid phase

$z\ [m]$ – space coordinate

The mass transport on the surface of the sorbent occurs parallel to the mass transport in the gas phase. In most cases, the mass transport on the surface of a sorbent is slower compared to the mass transport in the gas phase (Kärger et al., 2012). In case of two parallel mass-transport resistances, the slower one can be neglected. Therefore, the mass transport on the solid's surface is neglected.

The gas-phase mass transport and the adsorption and desorption kinetics of water and the sorbent occur in serial. The adsorption and desorption kinetics to the surface of the graphite particles is considered fast compared to the gas-phase mass transport. Scholl et al. showed this for activated carbon (Scholl et al., 1993). In case of two serial mass-transport resistances, the faster one can be neglected. Therefore, the adsorption and desorption kinetics are neglected.

The concentration quantities are converted to the sorptive loading of the solid and molar fractions in the gas phase in equation 23 (assuming ideal gas conditions apply). The diffusion coefficient is the effective diffusion coefficient, discussed in chapter 3.2.

$$\varepsilon \cdot \widetilde{M}_i \cdot \tilde{\rho}_G \frac{\partial \tilde{y}_{i,g}}{\partial t} + (1 - \varepsilon) \cdot \rho_s \cdot \frac{\partial X_{i,s}}{\partial t} = D_{eff,i,j} \cdot \widetilde{M}_i \cdot \tilde{\rho}_G \frac{\partial^2 \tilde{y}_{i,g}}{\partial z^2} \tag{23}$$

$\widetilde{M}_i \left[\frac{g}{mol}\right]$ – molar mass of component i
$\tilde{\rho}_G \left[\frac{mol}{m^3}\right]$ – molar gas density
$\tilde{y}_{i,g} \left[\frac{mol}{mol}\right]$ – molar fraction component i in gas
$X_{i,s} \left[\frac{g}{mol}\right]$ – mass loading i in solid phase
$\rho_s \left[\frac{g}{m^3}\right]$ – density solid
$D_{eff,i,j} \left[\frac{m^2}{s}\right]$ – effective diffusion coefficient i in j

This equation must be transformed into an equation with only one dependent variable instead of the currently two (molar fraction and solids loading). This transformation is necessary to solve the equation numerically. The dependency between the concentration in the gas phase and the concentration of the solid phase allows the transformation. The two quantities corelate via the sorption equilibrium. The conversion can be achieved by multiplying the time derivative of the molar gas fraction by the derivative of the activity by the activity. This derivative of the activity is mathematically one and does not alter the equation. The same applies to the derivative of the solids loading by the solids loading.

$$\partial \tilde{y}_{i,g} = \frac{\partial \tilde{y}_{i,g}}{\partial a_i} \cdot \frac{\partial a_i}{\partial X_{i,s}} \cdot \partial X_{i,s} = \frac{p_i^V}{p} \cdot \frac{\partial a_i}{\partial X_{i,s}} \cdot \partial X_{i,s} \tag{24}$$

a_i [$-$] – activity component i
p_i^V [Pa] – vapor pressure of component i
p [Pa] –pressure

The rewritten derivatives in equation 24 can be replaced by the equation for the liquid-vapor phase equilibrium and the sorption equilibrium. The Rault-Dalton equation gives a constant (for isothermal, isobaric conditions) expression for the liquid-vapor equilibrium. The sorption equilibrium can be a non-linear function (compare chapter 3.1.2). This makes its derivative variable, which makes numerical methods necessary to solve the equation. The derivative is numerically solved by a second order approximation.

Alternatively, if the sorption equilibrium is unknown, a constant sorption coefficient can also correlate activity and sortive loading of the solids.

$$\partial \tilde{y}_{i,g} = \frac{K}{\widetilde{M}_i} \cdot \partial X_{i,s} \tag{25}$$

$K \left[\frac{g}{mol}\right]$ – constant sorption parameter

$\widetilde{M}_i \left[\frac{g}{mol}\right]$ – molar mass component i

The boundary conditions: Dirichlet, Neumann, and Robin are applied to the boundaries as appropriate according to the experiment. A comprehensive derivation of this equation with the applied boundary conditions in each chapter can be found in the appendix 8.5.

Equation 23 in combination with either equation 24 or 25 describes mass-transport phenomena with predominantly adsorption mechanisms and the primary resistance in the gas phase of the porous structure.

3.3.2 Mass transport in absorbing systems

In a system where adsorption and absorption occur, as outlined in Figure 3.7, multiple transient mass-transport phenomena can be relevant to the overall mass transport of a system. The example in this Figure shows the mass transport in the gas phase and the mass transport in the binders. Literature shows that the mass transport of water in binder polymers can be slow (Eser, 2021). Therefore, it is possible that both mechanisms must be considered to describe the mass transport of this entire system. The micro and macro scale are introduced to classify both mass transports. These scales have different coordinate systems and can be coupled via the same time scale.

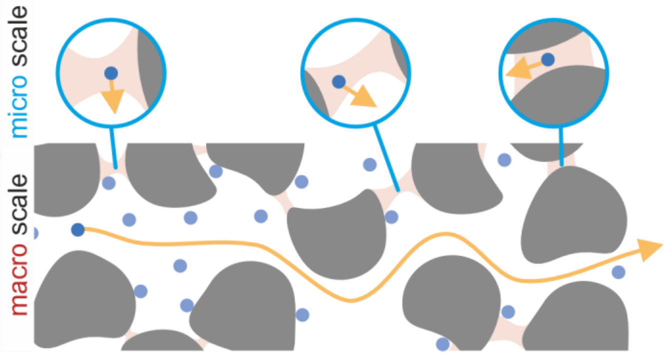

Figure 3.7: Outline of the mass transport through an absorbing porous structure. The mass transport in the absorbing phase (e.g., binder phase) is coupled with the adsorbing structure. If both resistances contribute to the mass transport of the entire system, a model with two scales is necessary to model moisture management and post-drying processes.

Micro and macro scale are named according to the mass-transport distance relative to each other. In case of an electrode, the mass transport on macro scale is gas-phase mass transport, and the mass transport on micro scale can be either binder diffusion or chemical sorption in cathode active material. Subdividing the volume of an electrode introduces the micro and macro scale to the equation 26.

$$\Phi \cdot \frac{\partial C_{i,Ma}}{\partial t} + (1-\Phi) \cdot \frac{\partial C_{i,Mi}(z)}{\partial t} = \Phi \cdot D_{eff,i,j} \cdot \frac{\partial^2 C_{i,Ma}}{\partial z^2} \qquad (26)$$

$\Phi\ [-]$ – volume fraction of the macroscale

$C_{i,Ma/Mi}\ \left[\frac{mol}{m^3}\right]$ – concentration of the macroscale/microscale

$z\ [m]$ – space coordinate of the macroscale

$D_{eff,i,j}\ \left[\frac{m^2}{s}\right]$ – effective diffusion coefficient i in j

The volume of the macro scale divided by the system's volume is the fraction Φ. This fraction splits the simulation volume in micro and macro scale. The accumulation of component i occurs in micro and macro scale. The terms of the mass transport of the macro scale are split into two phases according to equation 23. This is necessary to account for adsorption on macro scale. The accumulation term of the mass transport on micro scale depends on the space coordinate of the macro scale. The scales are coupled in between two mesh points of the macro scale. This means that every grid point of the macro scale minus one has an individual micro-scale accumulation term. The kinetic term on macro scale is independent of the micro-scale mass transport in direction of z. There is no mass transport in z-direction on micro scale.

The accumulation term of the mass transport on micro scale is unique for every grid point in z-direction. These accumulation terms on micro scale couple the micro- and macro-scale PDE. For every grid point in z-direction exists a set of PDE, initial, and boundary conditions for the respective micro scale (compare Figure 3.7). The PDE for the micro scales is indexed by k, compare Equation 27.

$$\frac{\partial C_{i,k,Mi}(z)}{\partial t} = \frac{\partial}{\partial x_k}\left(D_{i,Mi} \cdot \frac{\partial \mathrm{C}_{i,k,Mi}}{\partial x_k}\right) \tag{27}$$

$k[-]$ – index of the macro-scale grid point

$C_{i,k,Mi}$ $\left[\frac{mol}{m^3}\right]$ – concentration on micro scale

x_k $[m]$ – space coordinate on micro scale at k

$D_{i,Mi}$ $\left[\frac{m^2}{s}\right]$ –diffusion coefficient of i on micro scale

The space coordinate x is indexed by k, which ranges from 0 to the number of mesh points in z-direction $n_z - 1$. The concentration at the boundary of micro and macro scale is calculated according to either the sorption equilibria or a sorption constant. If the mass transport on micro scale is polymer diffusion, the diffusion coefficient $D_{i,Mi}$ is a function of the space coordinate. A more detailed derivation and implementation of equations 26 and 27 can be found in appendix 8.5.

4 Mass transport on micro and macro scale in electrodes[7]

Multiple mass-transport resistances such as macropore and micropore resistances occur during the sorption in porous structures (Kärger et al., 2012). Additionally, the mass transport in an electrode may be affected by a combination of sorption kinetics of the electrode's individual components. Therefore, it is likely that a combination of transport resistances affects the overall mass transport of e.g. water inside the electrode during post-drying. This means that the sorption kinetics as well as mass-transport resistances mutually affect the overall mass transport in an electrode. The terminologies micro and macro scale are introduced to characterize these sorption kinetics and mass-transport resistances according to their length scales. Under which circumstances the consideration of both scales is necessary can be assessed by comparing simulation to experiments. This comparison requires developing a suitable numerical routine as well as experiments. Hypothesis 1 is formulated as follows:

Describing the overall mass transport in the composite structure of electrodes requires the modeling of the sorption on micro and macro scale as coupled transient mass transport.

A novel mass-transport model is developed to describe the coupled transient mass-transport phenomena. This model builds on the equations, initial, and boundary conditions from section 3.3.2. Figure 4.1 sketches the numerical structure of the coupled partial differential equations (PDE) as implemented in the solver. The mass transport on both scales is solved in one dimension. The scales are coupled in between two grid points of the macro scale. Details can be found in the documentation of the solver "d03ppf"("NAG Library,"

---

[7] Data presented in this chapter are published as a peer-reviewed article.

2017). Therefore, the number of micro-scale PDEs is equal to the number of mesh points on macro scale minus one. Numerical efficiency is increased by accumulating grid points close to the phase boundaries. The structure of this model enables the consideration of multiple mass-transport mechanisms with their individual dependencies on process parameters. It can also be adjusted to various geometries.

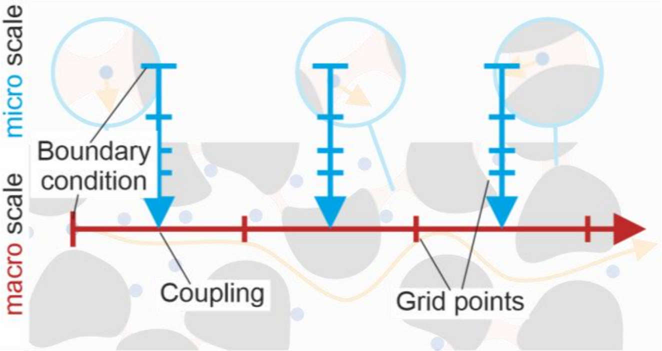

Figure 4.1: Sketch of the mass transport through an absorbing porous structure. The mass transport in the absorbing phase on micro scale, e.g., binder phase is coupled with the adsorbing structure on macro scale. If both resistances contribute to the mass transport of the entire system, a model with two scales is necessary to model moisture management and post-drying processes.

It is assumed that the sorption in an electrode is isothermal[8], due to water contents below 5000 wt-ppm in the electrode. Eser showed that the temperature change during sorption of water in an anode ($\Delta T = 6\ K$) is small compared to e.g. zeolites ($\Delta T = 40\ K$) (Eser, 2021). The water content in an electrode is the weighted sum of the water content in each electrode component (Eser, 2021). Therefore, the water content in an electrode is distributed on micro and macro scale. The following considers mass transport during a two-scale sorption process: adsorption of water on the active material and

---

[8] From an industrial perspective, this assumption must be challenged, for example in the heating phase during post-drying.

absorption of water in the binder of an anode. Subsequently, the mass transport on micro scale could be diffusion within inner pores of particles and the kinetics of chemical sorption in e.g. cathode active material.

Whether a mass-transport model that couples two transient mass-transport resistances on micro and macro scale can be applied to the overall mass transport of water in an electrode is assessed in the following (hypothesis 1). This evaluation is conducted for two anodes with different binder systems. The gas phase between the particles is the mass-transport resistance on macro scale and diffusion of water in the binder is the mass transport on micro scale. As a first step of validating hypothesis 1, a suitable characteristic quantity to assess the influence of the mass transport on micro and macro scale must be found. Additionally, the model must be checked for plausibility by comparing boundary cases and considering gradients of the mass transport on the individual scales. Subsequently, the model must be modified to account for the weight distribution of the components on micro and macro scale as well as the water distribution in the anodes to assess the influence of weight and water distribution. Eventually, the simulation results must be compared to experiments to validate hypothesis 1. These results must be critically discussed with present literature on electrode sorption.

4.1 Characterizing the coupled mass transport

The characterizing quantities of the mass-transport arrangement of water in an electrode must describe the system unambiguously and should include:

- The two phases (solid and gas phase) on macro scale (compare section 3.3.1)
- The mass-transport resistance on micro scale
- The mass-transport arrangement on micro and macro scale

Dimensionless numbers such as the Biot-number of mass transport as well as diffusion times appear appropriate. Originally, the Biot-number characterizes two resistances, the external and internal heat-transfer resistance of a system.

However, a modification of the Biot-number can also be used for the mass transport. This modified Biot-number will be referred to as Bi', which was derived by Buss (Buss, 2017). Bi' accounts for the mass-transport resistance in gas and liquid/solid phase as well as the concentration gap at the phase boundary. The following prerequisites must be given for the Bi' to be applicable:

- Constant diffusion coefficient in the bulk phase
- Constant mass-transfer coefficient in the gas phase
- Omitting the coupled two-scale mass-transport arrangement

Figure 4.2 shows the mass-transport arrangement inside an anode and the abstraction to characterize the mass transport via Bi'. If Bi' is applied to the mass-transport arrangement inside the composite structure of anodes, this arrangement must be simplified. The mass transport on micro and macro scale is abstracted to a series of two mass transports. Any external mass-transport resistance outside the porous structure is not considered.

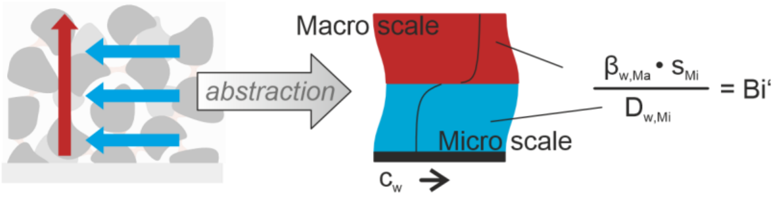

Figure 4.2: Illustration of the abstraction of the mass-transport arrangement in an electrode that is necessary to characterize this mass transport via the Biot-number of mass transport.

In consequence, the dimensionless Bi' represents a series of two mass-transport resistances. In this case, the two resistances are the one on micro scale (blue) in sequence with the one on macro scale (red). This simplification omits:

- The composite structure with spatially separated micro scales
- The influence of these micro scales on each other

- The accumulation of water in the particles and gas phase on macro scale

This simplification would be just if the mass transport on macro scale was fast compared to the mass transport on micro scale. However, in this case a comparison of the mass-transport resistances on micro and macro scale would not be necessary. The Biot-number can be applied to the drying of free-standing anodes, e.g. during a roll-to-roll process, to assess if the interparticle gas phase or the external gas phase predominates the drying, as done by Eser (Eser, 2021). While this consideration is feasible for free-standing anodes, this consideration cannot take the transient mass-transport arrangement on micro and macro scale into account. If the transport distance on macro scale increases, for example during storage, handling, and post-drying in coil format, it is likely that the mass transport on macro scale influences the overall mass transport inside the electrode. It is the objective to model the mass transport of water in electrode coils during storage, handling, and post-drying. Therefore, the application of the Biot-number Bi’ to the mass-transport arrangement on micro and macro scale appears unsuitable as a characterizing number.

A characterizing quantity for transient mass transport is the diffusion time. Börnhorst used the diffusion time to compare diffusion to relaxation, a competing transport mechanism, within polymer nanolayers via the Diffusion-Deborah number (Börnhorst, 2021; Börnhorst et al., 2021). A similar approach can also be applied to the mass-transport arrangement inside an electrode. The mass-transport mechanisms on micro and macro scale are then considered as competing transport mechanisms. Figure 4.3 shows how the composite structure of the anode is abstracted to define diffusion times of the mass transport on micro and macro scale.

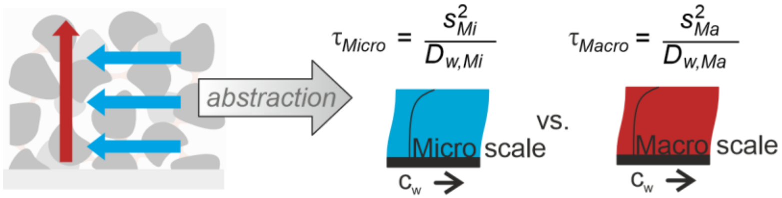

Figure 4.3: Illustration of the mass-transport arrangement in the composite structure of an electrode and the diffusion times of the mass transport on micro and macro scale. The anode is regarded as a system with the mass-transport resistance on micro and macro scale. The fraction of the resulting diffusion times determines which mechanism predominates.

The diffusion times τ_{Micro} and τ_{Macro} represent a time that is proportional to the respective diffusion process. These times can be used to compare the time scales of both diffusion processes. τ_{Micro} includes the mass-transport distance and the diffusion coefficient of water on micro scale. In this case, the mass transport on micro scale is the diffusion of water in the binder polymer. As this micro scale's mass-transport distance and diffusion coefficient depend on water content, simplifications are necessary to obtain constant τ_{Micro}:

- All the polymer structures have the same effective mass-transport distance
- The diffusion coefficient of solvent in the polymer is independent of the solvent loading of the polymer[9]

τ_{Macro} includes the mass-transport distance and the effective diffusion coefficient on macro scale. The mass-transport distance on macro scale is the distance a water molecule must travel to leave the electrode structure. This distance could be the length of an electrode stack. The effective diffusion coefficient on macro scale is the diffusion coefficient of the mass transport through the gas phase of the electrode. It must also include the sorption

---

[9] This simplification is necessary for a scalar value of the diffusion time on micro scale. This simplification is not necessary if the diffusion time on micro scale is a function of the solvent concentration, which depends on time and space.

constants of the mass transport on micro and macro scale. That is the main difference between the micro and macro scale. Every molecule that leaves or enters the micro scale must pass through the macro scale, due to the structure of the electrode.

Essentially, τ_{Micro} regards the micro scale pretending the macro scale does not exist and τ_{Macro} combines both scales into one scale. Therefore, if the mass transport on macro scale is fast compared to the mass transport on micro scale, the mass transport on micro scale is unaffected by the mass transport on macro scale. However, if the mass transport on micro scale is fast, compared to the one of the macro scale, water on the micro scale must still travel through the macro scale. Therefore, the water content on micro scale must be included in the diffusion coefficient on macro scale via a sorption constant. This diffusion coefficient can be derived by solving equation 27 with an accumulation term on micro scale that is only time-dependent, see appendix 8.5.

The ratio of both diffusion times shows which diffusion process predominates the overall mass transport. If this ratio is approximately one, both mechanisms affect the mass transport within the anode. If τ_{Micro} is greater than τ_{Macro} the mass transport on micro scale affects the mass transport of the anode stronger than the one on macro scale. The reverse applies if τ_{Micro} is smaller than τ_{Macro}. Any mass-transport resistance outside the anode structure is disregarded by considering the here defined diffusion times. This proposed comparison of diffusion times appears to describe the mass-transport characteristic of the composite anode. It will indicate whether the proposed mass-transport model is suitable to describe the mass transport of water in an electrode (hypothesis 1). The applicability of comparing the diffusion times must be tested by considering boundary cases of the model.

$$\begin{aligned} &\tau_{Micro} \ll \tau_{Macro} \rightarrow \text{Macro-scale controlled} \\ &\tau_{Micro} \gg \tau_{Macro} \rightarrow \text{Micro-scale controlled} \end{aligned} \tag{28}$$

4.2 Evaluating the Two-Scale-Model with boundary cases

This section theoretically verifies the numerical model, henceforth Two-Scale-Model, for the sorption in the composite structure of an electrode. If this model replicates the boundary cases of the mass transport on pure micro and macro scale correctly, it is an indication that it is correctly implemented. Furthermore, the applicability of the diffusion times can be evaluated by considering their ratio. If the results of the Two-Scale-Model with $\tau_{Micro} \ll \tau_{Macro}$ and $\tau_{Micro} \gg \tau_{Macro}$ match the results of the single scale models, these diffusion times characterize this mass-transport arrangement correctly. These assessments are conducted with a model system of an anode structure that has equal distribution of water on its micro and macro scale. Additionally, the volume on micro and macro scale is equally distributed (vol-% 50:50).

Macro-scale-controlled desorption

Figure 4.4 shows the comparison of the Two-Scale-Model to the solution of a simulation that purely considers the mass transport on macro scale. The micro scale's diffusion time is varied while the macro scale's diffusion time is kept constant. This is necessary to maintain comparability to the boundary case. The solution of pure macro-scale simulation solely regards the mass transport through the porous structure of the electrode and assumes that the entire amount of solvent is in the gas phase and on the particles on macro scale.

The concentration of the water is plotted on the y-axis over time on the x-axis. Absolute numbers are irrelevant for this consideration, therefore $C_{water,0}$ marks the start concentration prior to desorption and $C_{water,\infty}$ the equilibrium concentration. Likewise, the time starts at zero and propagates until the end of the plot. The red line marks the solution of the pure macro-scale desorption, which is equivalent to Fick's second law of diffusion. The black lines mark the solutions of the Two-Scale-Model with the respective ratio of the diffusion times. The solutions of $\tau_{Micro} \neq \tau_{Macro}$ were calculated with either τ_{micro} one order of magnitude greater or smaller than τ_{macro}.

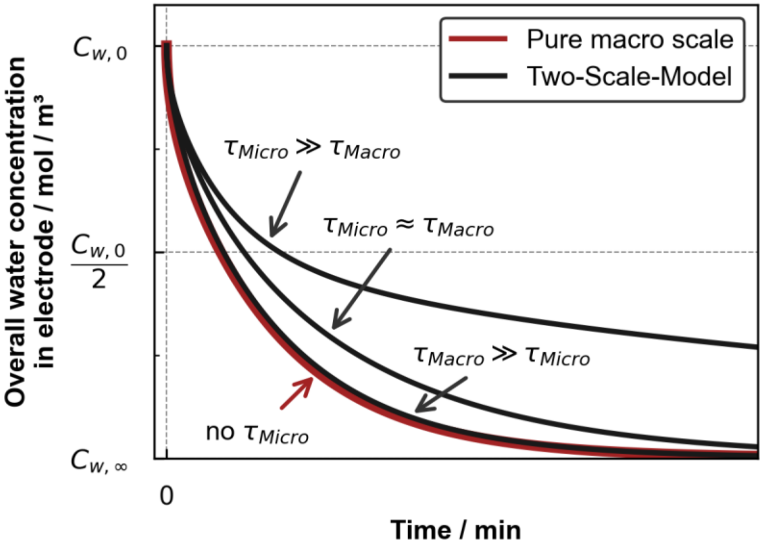

Figure 4.4: Simulated desorption of the Two-Scale-Model and pure macro scale. τ_{Micro} varies. If τ_{Macro} is 10-times larger than τ_{Micro}, the influence of the sorption on micro scale on the overall sorption is neglectable. For the other cases, the solution of the Two-Scale-Model differs from the solution of the pure macro scale. At the end of the plot, the simulation with $\tau_{Macro} \gg \tau_{Micro}$ reaches the equilibrium, while the simulation with $\tau_{Micro} \gg \tau_{Macro}$ is still desorbing. Data reprinted with permission from (Heckmann et al., 2026a).

The simulation with $\tau_{Macro} \gg \tau_{Micro}$ propagates like the solution of the pure macro-scale simulation. This observation shows that the mass transport on micro scale can be omitted if its diffusion time is one order of magnitude smaller than the one on macro scale. The simulation of the Two-Scale-Model with $\tau_{Micro} \approx \tau_{Macro}$ has a different shape than the pure macro-scale simulation. This circumstance shows that at equal diffusion times on both scales, the solution of the Two-Scale-Model differs from a solution of Fick's second law of diffusion. This observation is confirmed by the solution with $\tau_{Micro} \gg \tau_{Macro}$, which further deviates from the pure macro-scale solution with significantly increased desorption time and different shape. At the end of the plotted simulation time, the pure macro-scale simulation reaches its equilibrium. At the same time, the simulation with $\tau_{Micro} \gg \tau_{Macro}$ is still desorbing.

Micro-scale-controlled desorption

Figure 4.5 displays the comparison of the Two-Scale-Model to the simulation of pure micro scale. The time scale and concentration of this Figure and Figure 4.4 is the same. The macro scale's diffusion time is varied while the micro scale's diffusion time is kept constant, to maintain comparability to the boundary case. The solution of the pure micro-scale simulation solely regards the mass transport in the polymer structure. This simulation has the same diffusion time and solvent loading as the mass transport on micro scale of the Two-Scale-Model. The micro-scale volume with respect to the entire simulation domain is 50 vol-% (the rest is macro-scale volume). Plotting the results of the Two-Scale-Model on the same axis as the results of the pure micro-scale simulation requires scaling the pure micro-scale results. This adjustment is necessary because the water on macro scale does not penetrate the micro scale and must therefore not be considered in the simulation of the pure micro scale. Unlike, for the simulation of the pure macro scale where the water on micro scale penetrates the macro scale. This scaling factor is 50 %, which is the volume fraction of micro scale in the Two-Scale-Model. Therefore, the initial concentration of the pure micro-scale simulation in the following Figure is $\frac{c_{w,0}}{2}$. The amount of solvent on macro scale should not affect the mass transport on micro scale, if the mass transport on macro scale is sufficiently fast.

The simulation with $\tau_{Micro} \approx \tau_{Macro}$ is the same as the one in Figure 4.4. The solution with no τ_{Macro} is the fastest desorbing boundary case with no mass-transport resistance on macro scale. Comparing the $\tau_{Micro} \gg \tau_{Macro}$ to the simulation with no τ_{Macro} shows that the ratio in diffusion time of 10 represents the boundary case with small differences in the beginning. This difference originates from the presence of the mass-transport resistances on macro scale. Despite being fast compared to the mass transport on micro scale, the one on macro scale affects the desorption in the beginning. This observation combined with the boundary case from Figure 4.4 shows that the

Two-Scale-Model returns solutions for the desorption of the mass-transport arrangement in an electrode that differ from the solution of pure micro and macro scale. Whether the solution of the Two-Scale-Model is correct will show the comparison to experiments later. While the simulated desorption for $\tau_{Micro} \gg \tau_{Macro}$ is mostly governed by the mass transport on micro scale, using the Two-Scale-Model is still necessary to describe the entire desorption propagation.

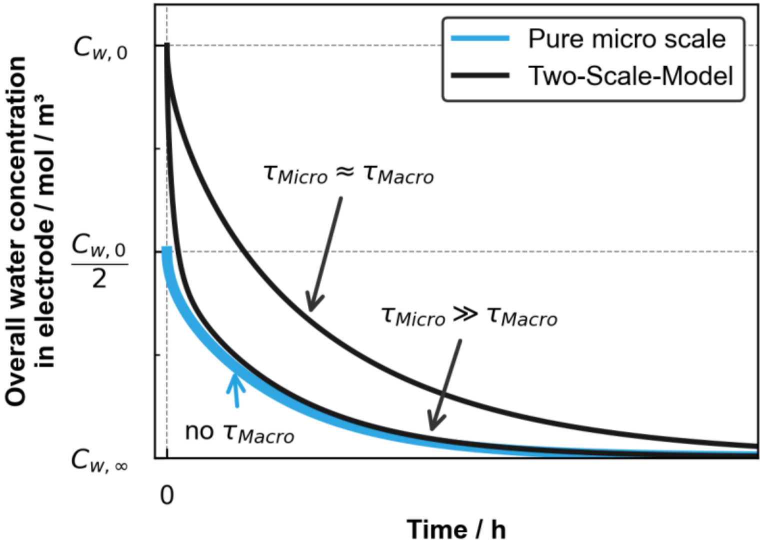

Figure 4.5: Simulated desorption of the developed Two-Scale-Model and pure micro scale. τ_{Macro} varies. For $\tau_{Micro} \approx \tau_{Macro}$, the solution of the Two-Scale-Model differs from the solution of the pure micro scale. If $\tau_{Micro} \gg \tau_{Macro}$, the influence of the macro scale on the overall sorption is neglectable. Data reprinted with permission from (Heckmann et al., 2026a).

Gradients during desorption

The gradients of the concentration on micro and macro scale give further information about the functionality of the Two-Scale-Model. Additionally, these gradients show which scale's mass transport predominantly affects the overall mass transport in the electrode. Figure 4.6 shows the concentration and implicitly the gradients on micro and macro scale of the results from Figure 4.4. The mass-transport resistance on macro scale is constant, while the resistance on micro scale changes. Both scales have identical initial concentrations. Therefore, there is no concentration shift at the boundary of the micro and macro scale.

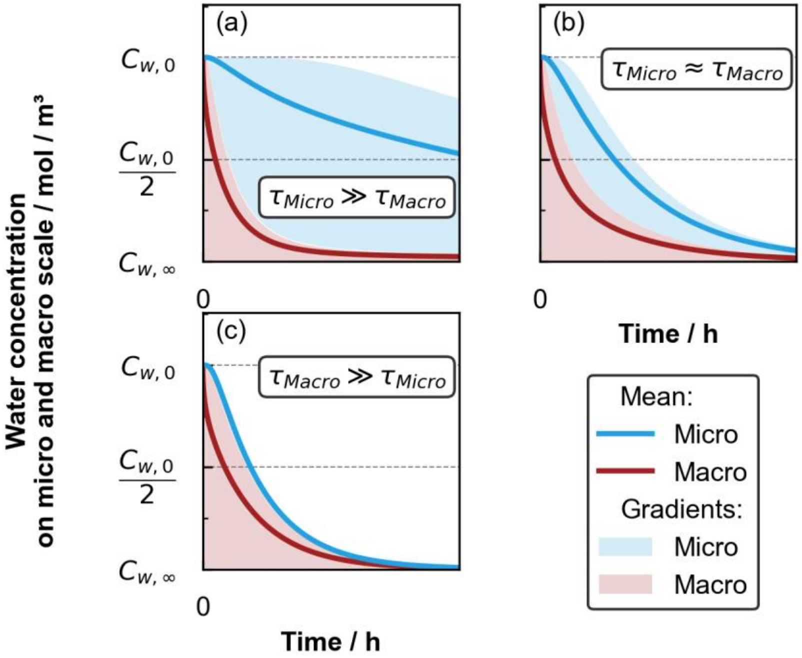

Figure 4.6: Display of the concentrations on micro and macro scale from the simulations shown in Figure 4.4. τ_{Micro} varies. The concentration difference indicated by the colored areas implicitly shows the concentration gradients during the desorption. The concentrations on micro scale are represented by the micro scale that desorbs slowest. The colored area indicates which scale's mass transport governs the mass transport of the electrode. Data reprinted with permission from (Heckmann et al., 2026a).

The concentration is plotted over time from initial to final equilibrium concentration. The concentrations of each desorption simulated with the Two-Scale-Model from Figure 4.4 are plotted in the subplots a, b, and c. Solid lines show the average concentration on each scale and the colored areas show the minimal and maximal concentration on each scale. Implicitly, the colored areas show the concentration gradients on each scale. The structure of the electrode requires the implementation of several micro-scale PDEs in the simulation. Only the slowest desorbing micro scale of the entire simulation was chosen to represent the mass transport on micro scale (compare Figure 4.1), for the sake of lucid presentation.

The gradients match the results of the integral consideration of the simulation results from Figure 4.4. If the concentration gradients on micro scale are small compared to the ones on macro scale, the desorption is unaffected by the micro scale's mass transport. Even though the effect is small, the mass transport on macro scale is affected by the diffusion time on micro scale. This is noticeable by the quicker depletion of the concentration on macro scale, if the micro scale's mass transport is slow (subplot a). The fact that micro scale's mass transport impedes the water from reaching the macro scale explains this phenomenon.

Summary of evaluating the Two-Scale-Model

Considering the boundary cases and the gradients of the solution from the Two-Scale-Model allows the following conclusions for the mass-transport arrangement:

- The Two-Scale-Model correctly replicates the boundary cases of the pure single-scale mass transport
- The diffusion times determine which scale predominates the mass transport relative to each other
- For $\tau_{Micro} \approx \tau_{Macro}$, the mass transport on micro and macro scale mutually affects the mass transport in the Two-Scale-Model. Outside this range, the consideration of single-scale mass transport suffices

- The Two-Scale-Model is required for $\tau_{Micro} \gg \tau_{Macro}$ to describe the entire desorption
- The distribution of the diffusion times also determines the shape of the sorption curves

The diffusion times can characterize the mass-transport arrangement. The Two-Scale-Model has proven to replicate boundary cases. It provides solutions for sorption curves in cases where the diffusion times on micro and macro scale are in the same order of magnitude. These solutions differ from the one-dimensional models. Therefore, the Two-Scale-Model will be compared to desorption experiments. This comparison will show whether this model is a suitable candidate to describe the mass transport during sorption of water in an electrode (hypothesis 1).

4.3 Applying the Two-Scale-Model to LiB anodes[10]

So far, the simulations with the Two-Scale-Model regarded structures with equal water distribution on micro and macro scale. Regarding this model structure was necessary to leave out any influence of the water distribution inside the electrode on the mass-transport evaluation. In the chapter, the Two-Scale-Model is modified to account for a water distribution of LiB anodes as reported by Eser et al. and Heckmann et al. (Eser et al., 2020c; Heckmann et al., 2022). The desorption of water from two anodes will be simulated with the Two-Scale-Model:

- A PVDF anode with most of the water adsorbed to the active material (spherical graphite)
- A CMC/SBR anode with most of the water absorbed in the binder structure (CMC/SBR)

---

[10] Philipp Barbig dedicated his master’s thesis to the application of the Two-Scale-Model to the post-drying of LiB anodes, focusing on sample preparation and micro-scale modelling.

The difference between the anodes is the absolute amount of water absorbed in the anode’s binder system and the distribution of the absorbed water among the components. Figure 4.7 shows the weight distribution of the components of both anodes and the respective amount of water that each component holds. The distribution of water in the component is modeled via the superposition principle. This superposition of the sorption equilibria is based on Eser and Kachel (Eser et al., 2020c; Kachel et al., 2013). The distribution of water in the anode is a prediction based on this model. These predictions also serve as a basis for the simulation with the Two-Scale-Model.

Depending on the composition of an anode, the water distribution among micro and macro scale is very different. The water sorption behavior of the individual components in the PVDF anode shows that the active material and carbon black, which account for about 94 wt-% of the total mass, are responsible for 89 % of water uptake in the entire anode. This anode holds most of the water in the active material, thus on macro scale. Therefore, the PVDF anode poses a system that is expected to be less affected by mass transport on micro scale compared to the CMC/SBR anode. This anode has a similar weight distribution of its components. However, the water distribution within the active material (macro scale) and the binder structure (micro scale) is inversed compared to the PVDF anode. Eser et al. showed the hydrophilic behavior of the CMC/SBR binder system, which is responsible for ~ 90 wt-% of the water uptake. Therefore, the CMC/SBR anode poses the system, where the mass transport on micro scale is expected to predominate the mass transport of this electrode.

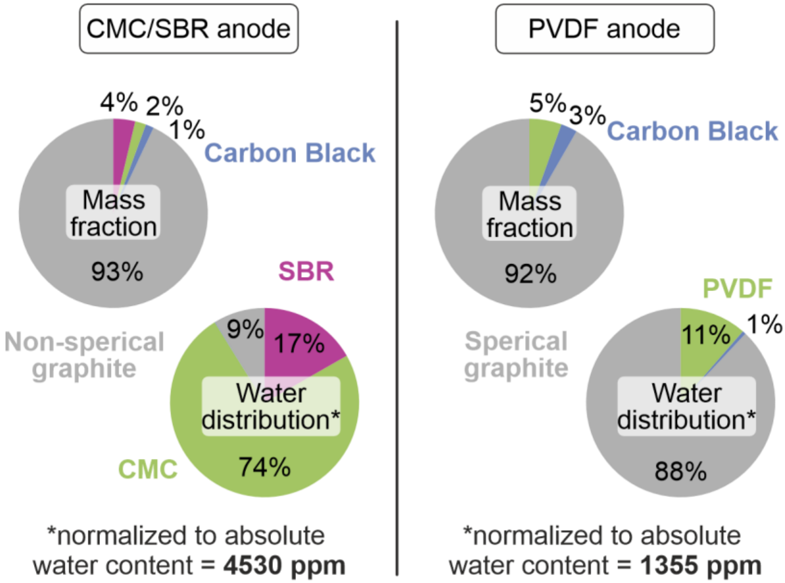

Figure 4.7: Component and water distribution in wt-% of anodes with a CMC/SBR and PVDF binder system. The water distribution is modeled after the superposition principal from Kachel et al. and Eser et al. (Eser et al., 2020c; Kachel et al., 2013). The component distribution of both anodes is similar. However, the water distribution greatly depends on the binder system. The water distribution in the CMC/SBR anode is disproportional to its weight distribution of the components. The water distribution in the PVDF anode is proportional to its weight distribution of the components.

These two anodes serve as validation-samples to evaluate the applicability of the Two-Scale-Model to the sorption of water in anodes (hypothesis 1). The applicability of the Two-Scale-Model must be evaluated by comparing its results to the experimental desorption of these anodes while drying. First, the influence of the water distribution inside the anode is theoretically assessed. Afterwards, the experiments are evaluated and compared to the results of the Two-Scale-Model. The Two-Scale-Model will be implemented with the mass transport of water through the structure of the active material on macro scale. The water content of the carbon black is added to the water content of the active material. The mass transport of water in the binder structure is the mass transport on micro scale. In case of the CMC/SBR anode, the water in the CMC and SBR will be combined on the micro scale. This means that the water uptake of both binders is considered, and they will be implemented as one mass transport on micro scale.

Assessing the effect of water distribution

The data in Figure 4.8 show the water distribution of the CMC/SBR anode and a simulated desorption curve of this anode with two ratios of the diffusion times.

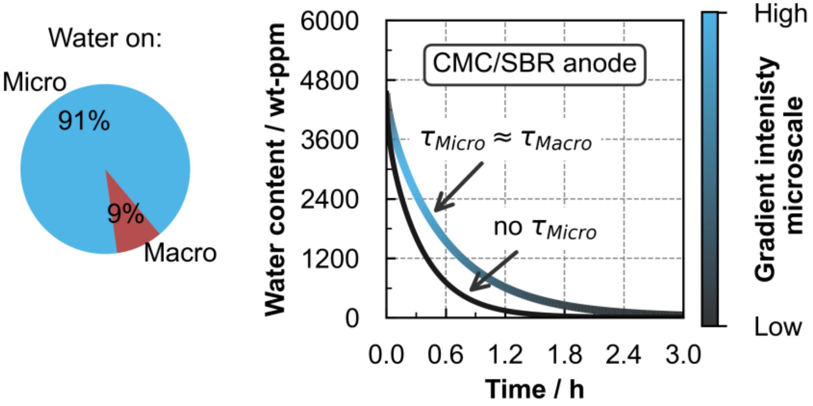

Figure 4.8: Water distribution in the CMC/SBR anode among the scales as pie-chart. Simulated desorption curve according to this water distribution with the Two-Scale-Model. The concentration gradient intensity indicates during which part of the desorption the mass transport on micro scale affects the process.

Derived from the data in Figure 4.7, the water that rests in the active material and carbon black is attributed to the macro scale. The water sorbed in the CMC/SBR is counted to the micro scale. The pie-chart displays this distribution in wt-%. The plot next to the pie-chart shows the simulated desorption curve of water from a CMC/SBR anode with no τ_{Micro}, which is equivalent to a pure macro scale simulation, and $\tau_{Micro} \approx \tau_{Macro}$. The water mass loading of the anode is plotted over time. The difference of the minimal and maximal concentration on micro scale at every time step normalized by the initial concentration on micro scale indicates the current concentration gradient intensity. This gradient intensity on micro scale is indicated by the intensity of blue. These concentration gradients develop in the beginning of the desorption and fade towards the end. The gradient intensity on micro scale does not give information about the concentration gradients on macro scale.

The desorption curve obtained with the simulation with no τ_{Micro} represents a desorption process where the mass transport on macro scale is limiting. The mass-transport parameters on macro scale were chosen in the order of magnitude of a diffusion coefficient of the gas phase in a porous structure. The desorption curve simulated with the Two-Scale-Model with $\tau_{Micro} \approx \tau_{Macro}$ is slower. This deceleration begins at the very beginning of the desorption when the concentration gradients in micro scale are fully developed.

The data in Figure 4.9 show the simulation results of the desorption of water from the PVDF anode, like Figure 4.8. The distribution of the water in the components on micro and macro scale inside the PVDF anode is inverse to the distribution inside the CMC/SBR anode. Therefore, the influence on the overall mass-transport resistance is expected to be small. This expectation is confirmed by the comparison of the desorption curves simulated with no τ_{Micro} and $\tau_{Micro} \approx \tau_{Macro}$. The propagation of both solutions is similar even when the concentration gradients on micro scale are developed. A small deviation can be observed when the gradients on micro scale are most intense. Comparing the CMC/SBR anode to the PVDF anode shows that with the same diffusion time ratio the distribution of water within the anode affects mass transport within the anode. More water on micro scale decelerates the mass transport within the anode.

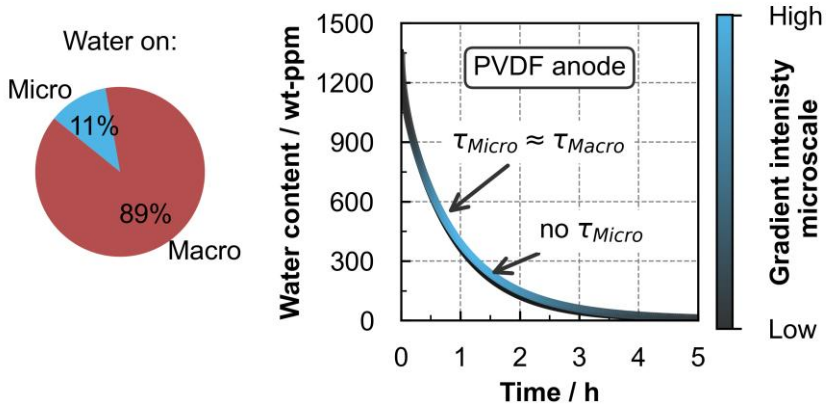

Figure 4.9: Water distribution in the PVDF anode among the scales as pie-chart. Simulated desorption curve according to this water distribution with the Two-Scale-Model. The concentration gradient intensity indicates during which part of the desorption the mass transport on micro scale affects the process. Data reprinted with permission from (Heckmann et al., 2026a).

Desorption experiments of CMC/SBR and PVDF anodes

Comparing the results of the theoretically derived Two-Scale-Model to experiments is crucial to prove the model's applicability to the sorption of water in anodes (hypothesis 1). Obtaining this experimental data requires a suitable measurement setup as well as a sample with a geometry that is affected by mass-transport phenomena on micro and macro scale. The measurement setup has been established as part of this thesis, which is the magnetic suspension balance that can be perfused at pressures below atmosphere (compare chapter 2.3.2). The sample resembles the geometry of either anode coils or compressed cell stacks (compare chapter 2.2.2). Multiple anodes are compressed between two aluminum plates to ensure a defined mass-transport path through the structure of the anodes rather than voids in between the anode sheets. The pure-vapor method (chapter 2.3.1) is used to load the samples with water. The samples were equilibrated to a relative humidity of 55% at a temperature of 80 °C. The measurement setup allows an immediate switch to the vacuum drying, which abruptly initiates desorption of water from the sample (details see chapter 2.3.2).

The data in Figure 4.10 show the desorption of water from the CMC/SBR anode stack at 80 °C and 200 mbar. The water content in wt-ppm is plotted on the y-axis over time in hours. The x-axis is shifted and shows values smaller zero, which is the time before the desorption was initialized and shows the equilibrium water content of the sample at 80 °C and 55 %-RH. Data points after zero on the time axis show the desorption of water from the CMC/SBR anode due to the perfusion of the measurement cell with dry nitrogen.

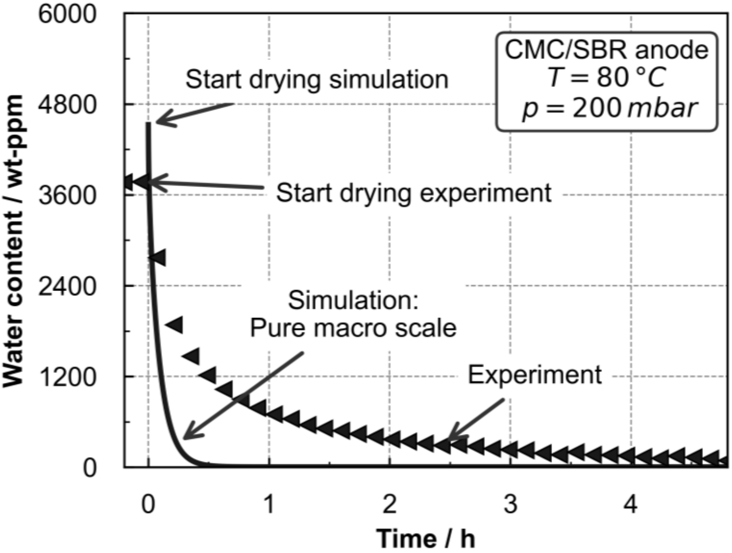

Figure 4.10: Desorption experiment of a CMC/SBR anode stack, preparation compare chapter 2.2.2. The simulation of pure macro scale's mass transport has no fitting parameters. The simulation estimates the initial mass loading of the electrode with a deviation of 17 %. The experiment desorbs slower than anticipated by the simulation. This could be caused by the mass-transport resistance on micro scale of the CMC/SBR anode.

The Figure contains experimental data and the results of a pure macro-scale simulation. The experimental mass loading decreases until it approaches zero after five hours. As comparison to this experimental desorption serves the simulation of the pure macro scale. This simulation assumes that the only limiting mass transport in the electrode stack is the gas-phase mass transport in the porous structure. The characteristics of this electrode stack are approximated with a porosity of 54 %, average pore diameter of 5 µm, and a transport distance of 4 cm (compare 2.2.2). The model of the effective diffusion coefficient of rarefied gases takes temperature and pressure of the experiment into account (discussed in Chapter 5.3). The porosity-tortuosity correlation is approximated with the equation after Zehner, Bauer, and Schlünder (Zehner and Schlünder, 1970). The start of the simulation was approximated with superposition of separately determined sorption equilibria (compare Figure 4.7). Therefore, the simulation of mass transport on macro scale does not have any fitting parameters and shows an expectation for the gas-phase mass transport in the porous structure.

Comparing simulation and experiment shows that the simulation considering pure macro scale has shortcomings. The modeled loading prior to drying is overestimated by 17 %, compared to the experiment. While the superposition of sorption equilibria returns accurate results at low RH, a decreasing accuracy at higher RH has been observed by Eser et al. (Eser et al., 2020c). Additionally, aging of the electrode has been reported to reduce the amount of absorbed water (Kosfeld et al., 2023). Regardless of the higher initial loading of the simulation, the simulated desorption curve reaches the equilibrium faster than the experiments. The experimental desorption decelerates before reaching the equilibrium and transitions into a linear decrease after ~ 1.5 hours. This behavior cannot be described by a single constant diffusion coefficient because the shape of the desorption curves differs. This conclusion is possible, because the shape of the desorption curve does not change by varying the diffusion coefficient, only the time of desorption changes. This comparison is like the results from Figure 4.8, where a pure macro-scale simulation is compared to a simulation with $\tau_{Micro} \approx \tau_{Macro}$.

The desorption of solvent from polymer films expresses a similar desorption curve with a decelerated mass transport towards lower solvent loadings. This phenomenon has been observed by Eser et al., 2020a; Schabel et al., 2004; Scharfer et al., 2008; Siebel et al., 2017. A solvent-concentration dependent diffusion coefficient is responsible for the decelerated desorption towards lower solvent concentrations. Applied to the composite structure of an electrode, a concentration-dependent diffusion coefficient could fit the measured drying. However, this fit would not provide a phenomenological replication of the mass transport on micro and macro scale. Therefore, the desorption of water from this CMC/SBR anode stack must be described with a model that takes other mass-transport resistances into account, such as the one on micro and macro scale. A concentration-dependent diffusion coefficient could still be applied to mass transport in a polymer phase on micro scale (Eser et al., 2020a).

The data in Figure 4.11 show the desorption experiments of the PVDF anode as well as a simulation considering mass transport on pure macro scale. The modeled initial mass loading of the anode is overestimated by 10 % compared to the experiment. Henceforth, the initial loading in the simulations will be proportionally reduced to match experimentally observed loading prior to drying. This will allow a more accurate comparison of simulation and experiment. Compared to the desorption of the CMC/SBR anode the desorption time is shorter. The simulated desorption curve desorbs in the same order of magnitude as the experimental data. Prior to reaching the equilibrium, simulation and experiment decouple and the experimental desorption decelerates transitioning into a linear decay.

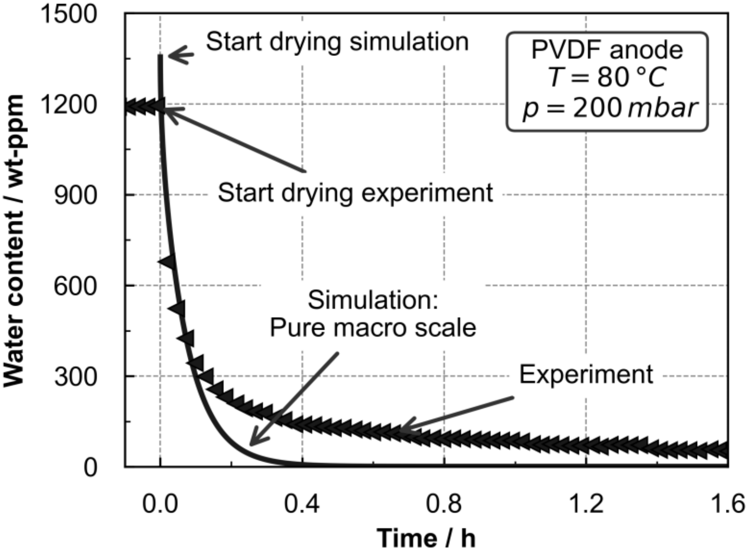

Figure 4.11: Desorption experiment of a PVDF anode stack, preparation compare chapter 2.2.2. The simulation of pure macro scale's mass transport has no fitting parameters. The simulation estimates the initial mass loading of the electrode with a deviation of 10 %. The initial desorption of water from the electrode can be replicated by the simulated desorption. The experimental results desorb slower than anticipated by the simulation towards the end of the experiment. This could be caused by the mass-transport resistance on micro scale of the electrode. Experimental data reprinted with permission from (Heckmann et al., 2026a).

This shows that even though most of the water in this electrode is expected on macro scale, the simulation of the pure macro scale describes the experiment only in the beginning. This mass transport on macro scale is simulated with mass-transport properties from Table 2.2 without any fitting parameters, like the simulation in Figure 4.10. Parameters such as tortuosity are unknown and were approximated with a model. Furthermore, the pore-diameter of the structure was chosen according to the most likely pore size by mercury intrusion measurements. It is possible that this pore size is not the relevant pore diameter to the mass transport. However, the initial desorption occurs in the same order of magnitude with plausible transport parameters of the gas phase in the porous structure. Still, comparing these experiments to simulation, even the PVDF anode requires a more complex simulation model to replicate the entire desorption. These experimental results further motivate the consideration of the Two-Scale-Model and provide the experimental basis the evaluation of this model in the next chapter.

Comparing the Two-Scale-Model to experiments

The comparison of results from the Two-Scale-Model to the previously discussed experiments will show the suitability of the Two-Scale-Model to describe the sorption behavior of water in the anodes (hypothesis 1). This hypothesis is validated if there are parameters for the mass transport on micro and macro scale that describe the experimental data. First, this model is implemented with constant diffusion coefficients on both scales. This implementation will show whether the Two-Scale-Model replicates the desorption of water from anodes with constant mass-transport resistances on micro and macro scale.

The data in Figure 4.12 show the experimental results and the pure macro-scale simulation from Figure 4.11 compared to the simulation results of the Two-Scale-Model. The water distribution among the anode's micro and macro scale and the initial loading is modeled after the superposition principle of sorption equilibria (compare Figure 4.7). However, the previous figures showed a discrepancy between the loading according to the superposition principle and the initial loading of the experiment. For comparability between simulation and experiment, the initial loading of the simulation was adjusted to the initial loading of the experiment. This adjustment does not affect the water distribution proposed by the superposition principle. The ratio of the diffusion times was fitted to best replicate the experimental desorption curve. Other anode properties were not modified to fit the experiments. Varying τ_{Micro} while keeping the macro scale's mass-transport resistance constant, effectively finds a pair of constant resistances on micro and macro scale that best describe the experimental desorption.

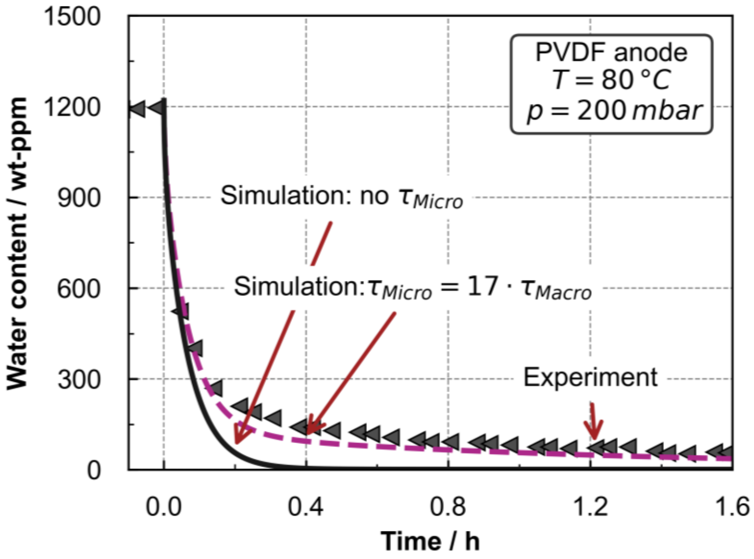

Figure 4.12: Comparison of the experiment and the pure macro-scale simulation (no τ_{Micro}) from Figure 4.11 to the simulation of the Two-Scale-Model proposed in this thesis. The desorption curve of the PVDF anode can be described with the Two-Scale-Model with constant mass-transport resistances in both scales. The diffusion time of the micro scale must be an order of magnitude larger than the diffusion time of the macro scale to replicate the slow drying at the end of the experiment. Data reprinted with permission from (Heckmann et al., 2026a).

The modeling of the desorption of water from the PVDF anode improves by using the Two-Scale-Model. This model replicates the experimental desorption with $\tau_{Mirco} = 17 \cdot \tau_{Macro}$. The modeled and experimental desorption propagate congruently. The modeled desorption matches the initial fast desorption as well as the slow desorption towards the lower water contents. This result shows that the Two-Scale-Model with constant mass-transport resistances is suitable to describe the PVDF anode's desorption. In this case the mass-transport resistance on micro scale is slower by one order of magnitude than the one on macro scale. Considering the structure of this anode, the mass-transport resistance on micro scale may either be in the PVDF-binder, the inner porosities of the active material, or a combination of both. The origin of this resistance cannot be assessed at this point.

The data in Figure 4.13 show the experimental results and the pure macro-scale simulation (no τ_{Micro}) from Figure 4.10 compared to the simulation results of the Two-Scale-Model. The same adjustment of the initial loading of the simulation, as describes prior in Figure 4.12, has been made in this figure as well. Comparing the simulation of $\tau_{Micro} \gg \tau_{Macro}$ and with no τ_{Micro} shows that the experiment is represented by neither of the two boundary cases. The experiment lies in between the two boundary cases. Modeling the desorption curve of water from the CMC/SBR anode improves by using the Two-Scale-Model. The Two-Scale-Model can replicate the experimental desorption with a ratio of the diffusion times of 5 with less deviation than the simulation with no τ_{Micro}. This shows that the mass-transport resistance on micro scale must be larger than the mass-transport resistance on macro scale. In the beginning, the model matches the desorption and overestimates the desorption speed after hour one of the experiment. This circumstance is an indication that the Two-Scale-Model with a constant mass-transport resistance does not suffice to replicate the entire desorption of water from the CMC/SBR anode.

Comparing the results of the Two-Scale-Model for the PVDF and CMC/SBR anode shows that both electrodes have different sorption behaviors. Most of the water is in the polymer structure on micro scale of the CMC/SBR anode. This distribution affects the overall mass transport right at the beginning of the experiment. Only 10 % of the water is in the polymer structure on micro scale of the PVDF anode. Therefore, the desorption is only affected at lower mass loadings of water. The mass-transport resistances on micro scale of the PVDF anode affect the desorption curve later compared to the CMC/SBR anode. The micro scale's diffusion time of the PVDF anode is 3.2 h, while the micro scale's diffusion time of the CMC/SBR anode is 1.1 h. Compared to this difference, the macro scale's diffusion times of both anode stacks are similar (12 and 14 min, PVDF and CMC/SBR anode). The effects of the water distribution on the scales and the influence of the different mass-transport resistances on micro scales overlap.

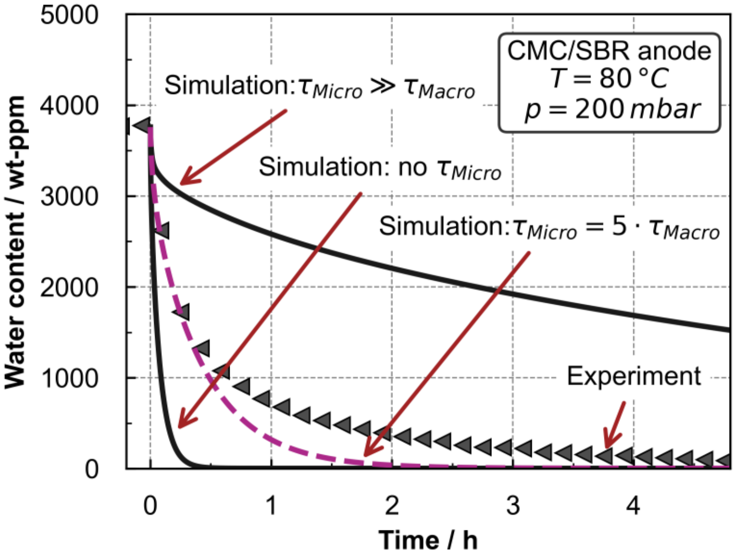

Figure 4.13: Comparison of the experiments and the pure macro-scale simulation (no τ_{Micro}) from Figure 4.10 to the simulation the Two-Scale-Model proposed in this thesis. The experimental desorption curve propagates in between the simulated desorption curves with $\tau_{Micro} \gg \tau_{Macro}$ and with no τ_{Micro} . A suitable description of the initial desorption rate can be achieved with $\tau_{Micro} = 5 \cdot \tau_{Macro}$. This simulation overestimates the rate of desorption in the middle of the plotted experimental time.

The Two-Scale-Model can replicate the desorption of water from the PVDF anode with constant mass-transport resistances, validating hypothesis 1 for this case. However, the quality of the fit for the CMC/SBR anode did not suffice. Considering findings from Eser et al., it is plausible that the polymer matrix inside an electrode, which is the mass transport on micro scale in this anode, has a concentration-dependent diffusion coefficient. The same phenomenon is widely known in polymer film drying (Merklein et al., 2021; Schabel et al., 2007; Scharfer et al., 2008; Siebel et al., 2017). As a next step, a concentration-dependent diffusion coefficient and, therefore, variable mass-transport resistances were incorporated into the Two-Scale-Model. These results, shown in Figure 4.14, will verify if the Two-Scale-Model can also replicate the desorption of the CMC/SBR anode.

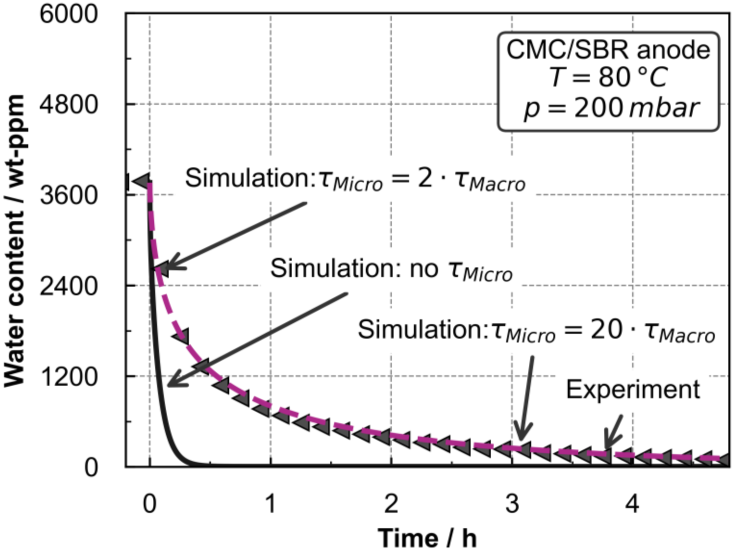

Figure 4.14: Comparison of the experiment from Figure 4.10 to the simulation of the Two-Scale-Model proposed in this thesis. The desorption of the CMC/SBR anode can be described with the Two-Scale-Model with constant mass-transport resistances on macro scale and a variable mass-transport resistance on micro scale. The diffusion time of the micro scale ranges across one order of magnitude to replicate the experiment. The diffusion time of the micro scale is calculated with the spatial average of the variable mass-transport resistance on micro scale.

The data in Figure 4.14 show the desorption curve of the CMC/SBR anode and the pure macro-scale simulation (no τ_{Micro}), the same as in Figure 4.10. The Two-Scale-Model with constant mass-transport resistances on macro scale and a variable mass-transport resistance on micro scale can replicate the experimental desorption. The results of the Two-Scale-Model follow the shape of the experiments over the entire desorption time. The variable mass-transport resistance reflects in the τ_{Micro}, which therefore changes with time. The mass-transport resistance on micro scale increases with decreasing water content of the polymeric binders. This means the desorption of water from the anode stack is controlled by the mass-transport resistance on micro scale at the end of the desorption. The complete propagation of the ratio between τ_{micro} and τ_{macro} is plotted in Figure 8.6 in the appendix. This result shows that the Two-Scale-Model can simulate the desorption of water from an anode with a CMC/SBR-binder system, validating hypothesis 1. The mass-transport resistance on micro scale must be variable to match the experiment for this CMC/SBR anode.

Contextualizing of the results for CMC/SBR anode and literature

It is likely that the variable mass-transport resistance on micro scale originates from the polymeric binders. Both, CMC and SBR express concentration-dependent water diffusion coefficients (Eser et al., 2020a). This means that the mass transport decelerates towards low mass loadings, which is the case during post-drying. The evaluation in the following compares mass-transport resistance on micro scale found in this study to mass-transport resistance of water in CMC after Eser. This is conducted by comparing the micro scale's diffusion time of the simulation from Figure 4.14 to the mass-transport properties of the CMC-film properties from Eser (Eser, 2021). This diffusion time on micro scale is the fraction of the mass-transport distance squared and the diffusion coefficient. The diffusion coefficient obtained from CMC-films by Eser are converted to diffusion times by assuming mass-transport distances. The results of this comparison are plotted in Figure 4.15.

The data of this Figure show the diffusion times of water in CMC and the micro scale's diffusion time found in this study on the y-axis. The range plotted on the x-axis is the relevant water content range on micro scale suggested by the results of the Two-Scale-Model from Figure 4.10. The models from Eser are temperature adjusted to the experimental temperature of 80 °C. τ_{CMC} shows diffusion times obtained from the diffusion coefficients of water in CMC from Eser and a mass-transport distance of 1 and 10 µm. The τ_{Micro} from the Two-Scale-Model obtained from the results in Figure 4.14 lies above the diffusion time obtained with a mass-transport distance of

10 µm. The effective mass-transport distance on micro scale must be 14 µm to be in line with the diffusion coefficient of water in CMC. This means, the Two-Scale-Model with the published parameters for the diffusion coefficient of water in CMC can replicate the desorption curve of the anode stack with an effective mass-transport distance on the micro scale of 14 µm. This mass-transport distance appears large, considering the thickness of an electrode at ~100 µm. These results show that mass-transport resistance on micro scale in an anode stack requires further research to make bulk mass-transport properties applicable.

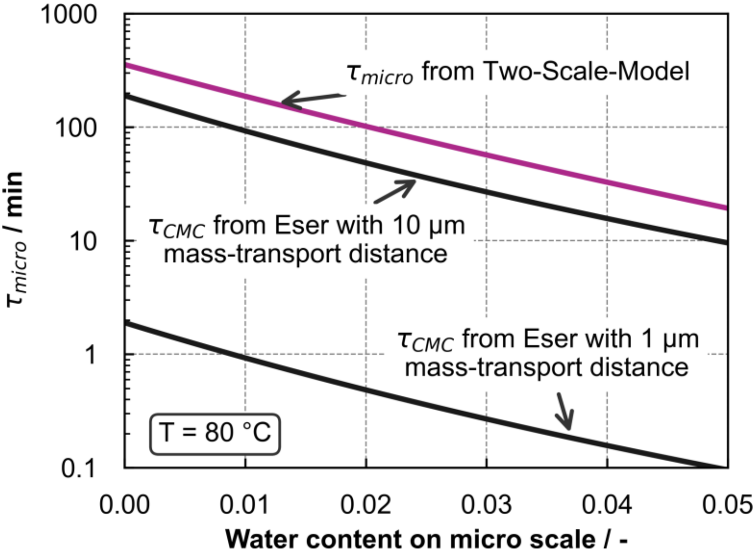

Figure 4.15: Diffusion times obtained from diffusion coefficients of water in CMC after Eser in black (Eser, 2021) compared to the diffusion time of water on micro scale obtained from Figure 4.14. The diffusion times propagate similarly and are shifted on the y-axis. The effective mass-transport distance on micro scale must be 14 µm to be in accordance with the diffusion coefficient data from Eser.

If the mass-transport resistance on micro scale is water concentration-dependent, the Two-Scale-Model can describe the desorption of water from the CMC/SBR anode stack. This could be explained by the concentration-dependent diffusion coefficient of solvents in polymers. However, this effect might be overlapped by other physical effects that may occur during the desorption of solvent from polymers:

- Distribution of the effective mass-transport distance in the polymer structure
- Multiple mass-transport mechanisms within the polymers, e.g., diffusion, relaxation etc.
- An interference of the mass transport in multiple components on micro scale

Theoretically, all these factors can be incorporated into the Two-Scale-Model. However, this incorporation can only be target-oriented, if further experiments are available. These experiments must isolate mass-transport mechanisms on micro scale from mechanisms on macro scale to unambiguously determine acting mechanisms and their transport parameters.

Applying the Two-Scale-Model to industrial vacuum-coil drying shows that a larger mass-transport distance on macro scale (coil-length) increases the macro scale's diffusion time. The micro scale's diffusion time remains unaffected. Therefore, in sufficiently large coils the mass transport on macro scale would be the limiting factor. Vice versa, if the mass-transport distance on macro scale decreases significantly, for example in a R2R post-drying process, the limiting mass-transport resistance would be on micro scale. This conclusion holds true, if there are no external mass-transport resistances. Furthermore, the temperature must be the same as the temperature of the experiments in this study. As mass-transport resistances on micro and macro scale have different dependencies on temperature, the mass-transport limitation may shift from one scale to another at other temperatures.

The overall mass transport of water in an anode can be modelled with the Two-Scale-Model, which validates hypothesis 1:

- A novel phenomenological mass-transport model, the Two-Scale-Model, was developed, to account for micro- and macro-scale sorption.
- The diffusion time characterizes the mass transport in the composite structure of an anode.
- The Two-Scale-Model proved to return plausible results in a boundary case consideration.
- The effects of the water distribution among micro and macro scale on the overall transport properties of the anode stack were ascertained.
- The Two-Scale-Model replicates the desorption curves of anode stacks, where most of the water is adsorbed on the active material with constant mass-transport resistances.
- The Two-Scale-Model replicates the desorption curves of anode stacks, where most of the water is in the polymer structure. Due to the complex sorption behavior of the CMC/SBR-anode, it is necessary to enable a variable micro-scale mass-transport resistance.

To the authors knowledge, the Two-Scale-Model is the first approach to simulate sorption of water inside battery electrodes that accounts for multiple mass-transport mechanisms. The fact that the Two-Scale-Model accounts for the mass transport on micro and macro scale individually allows the transfer to other geometries. These geometries could either be coils of electrodes or cell stacks during vacuum post-drying (longer mass-transport distance on macro scale) and R2R post-drying of electrodes. The structure of the model enables the incorporation of multiple mass-transport mechanisms on each scale as well.

However, establishing the model is only the first step to a holistic description of the sorption processes inside the composite structure of an electrode. The models of the scales must be assessed individually. The findings of this chapter indicate that the transfer of the mass-transport parameters from the polymer films investigated by Eser et al. to the complex microstructure inside electrodes requires further research. Furthermore, the mass transport on macro scale must be investigated in a less complex structure to find a suitable model for the gas-phase mass transport, regarding the vacuum post-drying. In the following, a model to describe the mass transport on macro scale will be probed.

5 Mass transport in porous structures towards vacuum[11]

The porous structure of battery electrodes poses a mass-transport resistance for water and other molecules during moisture management and post-drying of electrodes. This mass-transport resistance is especially pronounced if the mass-transport distance is in the range of cm, as it is the case during storage and post-drying in coil format and as stacked electrode. The post-drying in coil-format is usually carried out in vacuum, to accelerate the mass transport in the gas phase of the porous structure.

The gas-phase mass transport in the porous structure is regarded as the mass transport on macro scale in the previous chapter. So far, the mass-transport resistance on macro scale was kept constant, by constant temperature, pressure, and sample configuration. This chapter focuses on this mass transport at various process parameters and the modeling of the diffusion in the gas phase of a porous structure during the drying of this structure. The structure of an electrode is approximated by a backfill of the anode's active material, graphite. This is the same active material that is used in the PVDF anode from the previous chapter. Therefore, the particle size distribution of the backfill and the active material of the PVDF anode is the same. However, the backfill only resembles the structure of the PVDF anode, because the binder and additives of the anode alter the anode's structure compared to the backfill (compare Figure 8.1). Regardless, the experiment with the single-component system of a backfill has no influencing mass-transport parameters from the binder and additives, compared to the complete electrode. These experiments are guided by hypothesis 2:

---

[11] Data presented in this chapter are published as a peer-reviewed article.

A model for mass transport in the Stefan-Knudsen transition regime can be used to describe the mass transport inside the gas phase of an electrode structure at low pressure.

The validation of such a model must be carried out by comparing experiments to a simulation. The simulation uses the model mentioned in hypothesis 2 to describe the mass transport in the gas phase of the porous structure. The simulation regards diffusion as mass-transport mechanism. The experiments must be conducted under variation of the process parameters, pressure and temperature, as well as the structural parameters, porosity and length, to demonstrate validity of the simulation. The simulation describes the mass transport inside the porous structure with a one-dimensional transport equation that takes the various characteristics of porous structures into account. A mass balance of water inside the backfill of graphite is the basis for the simulation. This mass balance takes the accumulation of water in the gas phase and the sorption of water in the graphite into account. Figure 5.1 shows the simulation domain and boundary conditions.

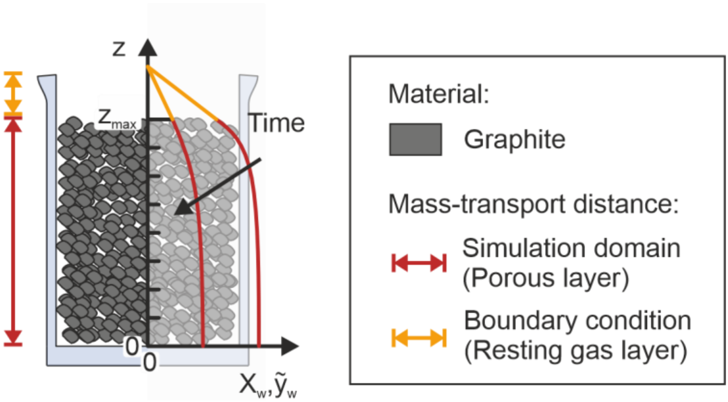

Figure 5.1: Schematic of the graphite backfill in the sample vial. The height of the backfill is the mass-transport distance (red) through the porous layer, and the resting gas layer on top is described by the boundary condition (yellow). The concentration profiles show the desorption occurring during the drying experiment.

The simulation domain is the height of the backfill in the sample vial. The gas-phase mass transport through the porous structure is the kinetic term. The mass transport on the surface of the solid phase is assumed to be slow compared to the mass transport through the gas phase of the porous structure. As the direction of both mass transports are parallel to each other, the one on the surface of the particles is neglected. This assumption is common during the modeling of sorption processes in porous structures (Kärger et al., 2012). The desorption kinetics of water from the surface of the particles into the gas phase is assumed to be fast compared to the gas-phase mass transport through the porous structure. This has been shown for water adsorption in activated carbon pellets (Scholl et al., 1993). Therefore, these desorption kinetics, which is serial to the gas-phase mass transport, can be neglected. The boundary condition (resting gas layer, Figure 5.1) considers the mass transport through the gas layer on top of the porous structure. It is assumed that the relative humidity above this resting gas layer equals the relative humidity of the gas, purging the cell. The sorption equilibrium relates the mass loading of the solid phase to the relative humidity in the gas phase (see appendix 8.7). Equation 23 shows this mass balance with accumulation and kinetic terms. A thorough derivation of Equation 23 can be found in appendix 8.5. A comparison of the numerical solution to the analytical solution of Equation 23 as an initial validation can be found in appendix 8.8.

Each of the following chapters considers one unknown mass-transport characteristic, while the other unknown characteristics are either constant or do not affect the mass transport of water in the backfill. First, the applicability of the boundary condition and the tortuosity of the structure must be assessed. Afterwards the effect of a pressure reduction on the diffusion regimes and the effective pore diameter can be probed. The drying gas for all following experiments was nitrogen.

5.1 Geometric influence on mass transport

A validation of the boundary condition applied to the resting gas layer on top of the backfill determines if the physics of this condition are appropriate. If the simulation correctly accounts for a variation in backfill height, the boundary condition can be validated (compare Figure 5.1). The mass-transport distance of the Robin boundary condition that accounts for the mass transport through the resting gas layer changes if the height of the backfill changes. Accordingly, the influence of the boundary condition increases if the height of the backfill decreases. Therefore, if the simulation (compare Equation 23) in combination with the Robin boundary condition correctly replicates the experiments, the simulation is verified. The data in Figure 5.2 show the experimental results with the respective simulation of the height variation in the backfill.

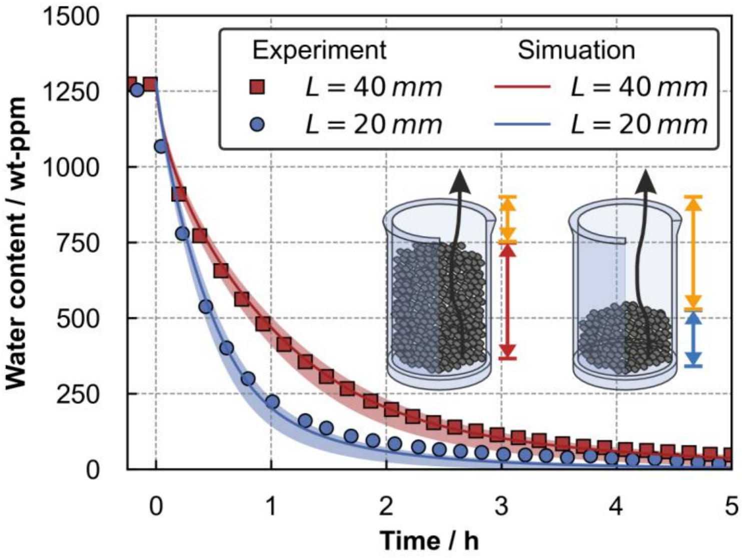

Figure 5.2: Mass-transport distance variation: Drying of a backfill of anode active material. The experiments were conducted at 30 °C, 800 mbar, a porosity of 61 %, and a height of the backfill of 40 mm and 20 mm. The sample with 20 mm backfill-height desorbs faster compared to the sample with a backfill height of 40 mm. The simulations replicate the experimental desorptions. The colored areas indicate the confidence interval of the simulation due to uncertainties of substance data and sorption equilibrium. Experimental data reprinted with permission from (Heckmann et al., 2023).

Figure 5.2 displays water content over time. The data points prior to zero show the mass loading of the backfill as markers that adjusts at a RH of 50 %. The drying starts at zero hours, when the sample is suddenly exposed to nitrogen with a dew-point temperature of -65 °C. The nitrogen flow that is constantly purging the measurement cell provides constant boundary conditions for drying. As expected, the water content decreases upon exposure to the nitrogen flow. The time window of five hours shows the interval where most water desorbs from the backfill. The experiments displayed show the drying of samples with 40 mm and 20 mm mass-transport distance as red and blue markers, respectively.

The respective simulations have matching colors as solid lines. The porosity-tortuosity correlation of Zehner-Bauer-Schlünder is used for the simulations, which will be discussed in the following chapter. The simulation of drying with a 40 mm backfill height replicates the experiments. The results of simulation and experiment obtained from the sample with a backfill height of 20 mm are similar. However, the simulation replicates the experiment accurately in the beginning of the drying, with decreasing accuracy in the end. This deviation may result from either another mass-transport resistance or other phenomena that are not incorporated in the simulation. This discussion will continue in the following sections. The colored areas show the minimal and maximal extent to which the simulation deviates from the simulation marked by the solid line due to uncertainties in substance data and sorption equilibrium (compare appendix 8.7). In the following, only the solid lines will be plotted.

Prior to the drying experiment the following quantities are determined and used in the simulation. The height of the backfill is measured. The porosity is accessible by comparing the volume of the solid phase in the sample via its weight and density to the entire volume of the sample. The diffusion coefficient of water in the gas phase is implemented according to the model after Fuller, Schettler, and Giddings. The only fit parameter is the tortuosity, which is approximated by the ZBS model (discussed in the next chapter). The mass-transport distances in the porous structure change and, therefore, also the mass-transport distance in the resting gas layer (compare schematic in

Figure 5.2). Thus, the fact that both simulations match their respective experiments validates the boundary condition of the simulation model.

It shows that the boundary condition is applicable to the resting gas layer. The expected dependency of the drying time on the mass-transport distance: $t_{drying} \sim s^2$ can only be implicitly shown. Equation 23 has this dependency, however it is altered by the elongated mass transport of the boundary condition. So far, the boundary condition of the sample is validated.

5.2 Structural influence on mass transport

The influence of the porous structure on the mass transport originates from the porosity and the tortuosity. Unlike porosity, tortuosity cannot be accessed gravimetrically and volumetrically and is subject of many studies and discussions. The (diffusional) tortuosity is a geometrical quantity. In many cases the tortuosity remains a parameter that is either fitted or obtained from models. The average pore diameter and the tortuosity of the backfill in Figure 5.1 are unknown quantities. Therefore, one quantity must be determined while the other does not affect the experiment. This situation occurs in the Stefan (continuum/fickian) diffusion regime, where molecule-molecule interactions dominate the mass transport, and the pore diameter of the structure has little effect on mass transport. As the pore diameter that is relevant for the mass transport is unknown, it must be estimated to assess the diffusion regime. The pore diameter was estimated via Mercury intrusion from anodes with the same active material and Mercury intrusion data for the active material itself (compare Figure 8.1 in the appendix). Both experiments yield similar results with the most frequent pore size by volume of the pores between 2 and 3 µm. This pore-diameter range results in Knudsen numbers between 0.08 and 0.06 at 800 mbar and 30 °C, which indicates mass transport in the Stefan regime.

Drying experiments with mass transport in the Stefan regime are shown in Figure 5.3. The two samples for the following experiment were prepared from the same anode active material with two porosities. Both samples each have a unique tortuosity, which is necessary to validate the ZBS model for this structure. The samples were prepared by incrementally adding and homogenously compacting a predefined amount of active material. All samples must have the sample backfill height in total.

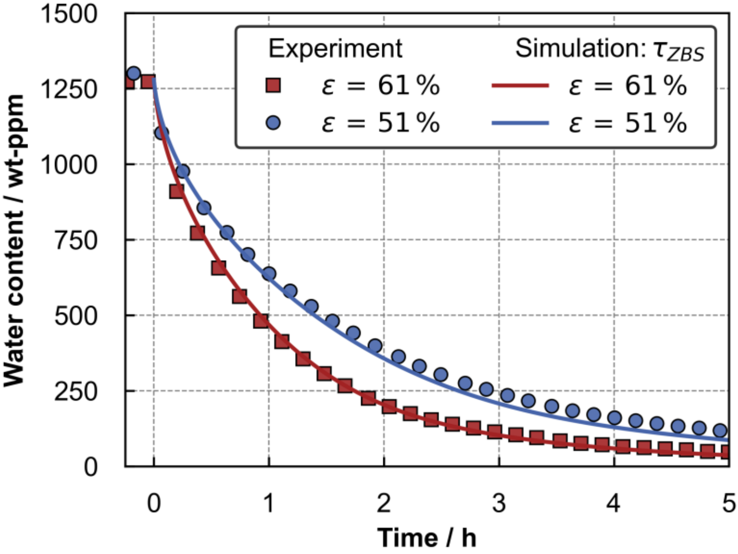

Figure 5.3: Porosity variation: Drying of backfills of anode active material. The experiments were conducted at 30 °C, 800 mbar, porosities of 51 % and 61 %, and a height of the backfill of 40 mm. The simulations use the tortuosity correlation of Zehner-Bauer-Schlünder. The sample with larger porosity desorbs faster compared to the backfill with the lower porosity. The simulation with the modeled values of the tortuosity replicates the desorption of both backfills. Experimental data reprinted with permission from (Heckmann et al., 2023).

The data of Figure 5.3 show the drying of a backfill compacted to a porosity of 51 % and 61 %. The sample with a porosity of 61 % dries quicker than the experiment with a porosity of 51 %. This effect can be explained by the larger volume available for the molecules during mass transport. Both simulations with the tortuosity correlation of ZBS replicate the experiments. A comparison of the simulation with other porosity-tortuosity models can be found in the appendix 8.8. This result shows that within the porosity range of 51 % to 61 % the correlation of ZBS adequately describes the influence of the porosity on the tortuosity in the backfill of anode active material. This model was originally developed for heat transfer in backfills of spheres, which could explain why its approximation is adequate for the mass transport in the spherical graphite. However the model was originally derived for monomodal particles, which is not the case for the spherical graphite.

It can be argued that the simulation with the ZBS tortuosity model does not perfectly match the experiment. For example, the fitted value of the tortuosity in the backfill with a porosity of 51 % is 1.85, while the ZBS correlation gives 1.7. This difference has a small effect on total effective diffusion coefficient (porosity/tortuosity of 0.28 versus 0.3). Therefore, the accuracy of the ZBS model suffices.

Establishing the tortuosity of the porous structure in the Stefan regime was necessary because the influence of the pore diameter on mass transport is small in the Stefan regime. This step determines the structural influence of the structure on mass transport. The tortuosity correlation of ZBS proved feasible for this porous structure, which will be used for any further simulation in this chapter. It must be noted that this conclusion cannot be generalized for porosities outside the considered range as well as for other porous structures made of this active material such as electrodes. For each new porous structure, the tortuosity must be determined individually by such measurements.

The previous two chapters show that the mass transport on macro scale – the mass transport through a porous structure that resembles a LiB electrode – can be modeled with the presented simulation at a pressure close to ambient pressure. This makes the model applicable to sorption and desorption processes during handling and storage. Considering the mass transport during vacuum drying requires experiments at lower pressure. The simulation model is evaluated at Knudsen numbers in the transition regime in between continuum and discontinuum.

5.3 Stefan-Knudsen Transition Model

A model for the effective diffusion coefficient that describes the diffusion in the gas phase of a porous structure made of particles must account for several effects:

- Volume reduction of the gas phase by the solid phase (ε)
- Elongation of the transport distance in the gas phase (τ)
- Velocity distribution of the molecules in the gas phase ($\overline{v}$)
- Change of diffusion regime induced by pressure change (Kn)
- Pore-size distribution due to the particle-size distribution

The effects have individual dependencies on system and process parameters. The porosity reduces the simulation domain to the accessible volume for gas-phase mass transport. The tortuosity is the geometric property of the porous structure and describes the elongation of the mass-transport distance. Tortuosity should be constant regardless of diffusion regime and process parameters (Reyes and Iglesia, 1991). Others found that the tortuosity depends on the diffusion regime (Burganos, 1998). The following results are interpreted assuming that tortuosity does not change with the diffusion regime. The velocity distribution of gas molecules is accounted for by the equations for the diffusion coefficients. The Bosanquet equation approximates the diffusion coefficient for the transition between diffusion regimes. This equation reciprocally adds the diffusion coefficients of Knudsen (discontinuum) and Stefan (continuum/fickian) diffusion (compare equation 20 (Bosanquet, 1944; Krishna and Van Baten, 2012; Pollard and Present, 1948; Scott and Dullien, 1962)). This equation was developed for cylindrical pores and agrees with experimental data and simulation. The Stefan-Knudsen transition model (SKT-model) is based on this Bosanquet equation. Figure 5.4 shows the effective diffusion coefficient for one pore diameter, the characteristic length ($L_{characteristic}$), calculated with the proposed Stefan-Knudsen transition model.

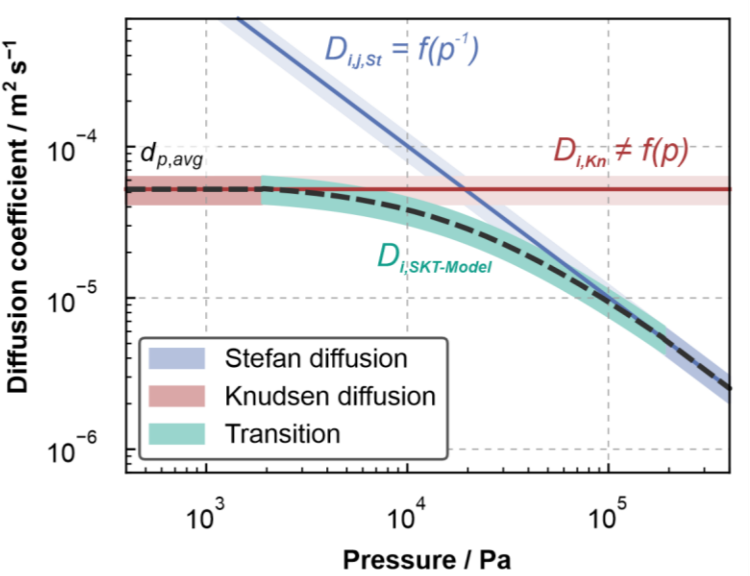

Figure 5.4: Diffusion coefficient of water in either nitrogen (Stefan) or vacuum (Knudsen) plotted over pressure for an exemplary pore diameter of 0.7 µm. The Stefan diffusion coefficient is the Fuller-, Schettler-, and Giddings-model and the Knudsen diffusion coefficient after Knudsen. The diffusion coefficient of the transition is calculated with a modified Bosanquet equation. Reprinted (adapted) with permission from (Heckmann et al., 2023).

The graphs in Figure 5.4 show the diffusion coefficient of water in a pore over pressure logarithmically. The diffusion coefficient in the Knudsen regime is not a function of pressure but of the pore diameter and temperature. The Stefan diffusion coefficient (continuum) increases towards low pressure and is also a function of temperature. The transition between these regimes is calculated with a modification of the Bosanquet equation. This modification introduces parameters that allow shifting the transition between Stefan and Knudsen regime.

The pore-size distribution of the porous structure can be accounted for by an average pore size and by multi-dimensional simulation approaches. The diffusion coefficient depends on the pore diameter in the transition and Knudsen regime. Therefore, when using the multi-dimensional simulation approach, the diffusion coefficient in the transition and Knudsen regime is distributed as well. Reducing the pore-size distribution to a single characteristic length, which is necessary for a one-dimensional simulation, omits the distribution of the diffusion coefficient. Figure 5.5 shows the variation of the diffusion coefficient according to a pore size distribution.

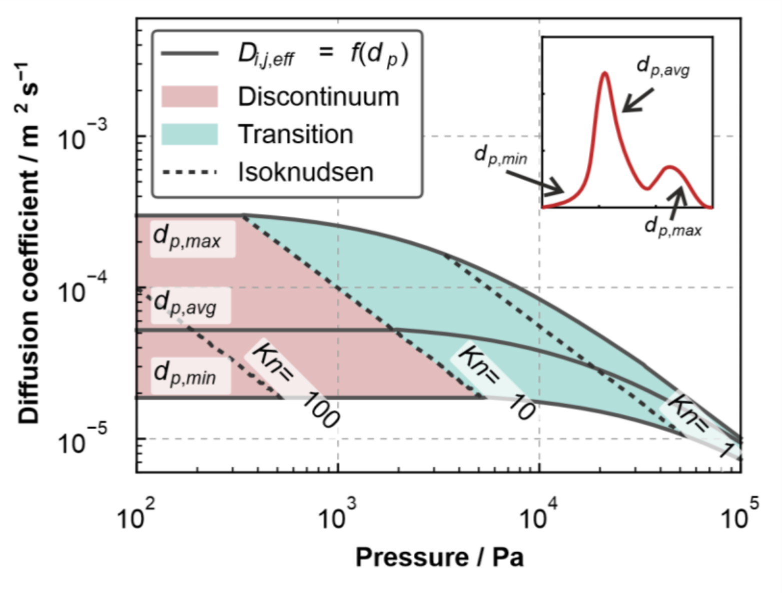

Figure 5.5: Diffusion coefficient of water in nitrogen in the Knudsen regime and the transition regime plotted over pressure for exemplary pore diameters of 0.25, 0.7, and 4 µm (min, avg, and max). The Knudsen diffusion coefficient is calculated after Knudsen and the transition diffusion coefficient with a modified Bosanquet equation. The pore-size distribution evokes a diffusion coefficient distribution. Reprinted (adapted) with permission from (Heckmann et al., 2023).

The graphs in Figure 5.5 show the diffusion coefficient of water in a pore over pressure logarithmically, like Figure 5.4 but on a different scale with the same pore diameter $d_{p,avg}$. The colored area spans the range of diffusion coefficients that occur in a porous structure with a pore-size distribution between $d_{p,min}$ and $d_{p,max}$. The lines of equal Knudsen numbers show that the mass transport of water in the gas phase of the structure occurs in transition and Knudsen regime at the same pressure. It is hypothesized that for a structure with the same average pore diameter but difference in the pore-size distribution, the effective diffusion may not be identical. Porosity and tortuosity account for the geometrical changes due to the changing pore-size distribution but cannot account for effects of the changing diffusion coefficient distribution. The idea is to introduce parameters into the Bosanquet equation that account for the change in diffusion coefficient distribution rather than adjusting tortuosity or average pore diameter. Equation 29 shows the proposed equation:

$$D_{i,eff} = \begin{cases} \frac{\epsilon}{\tau} D_{i,j,St}, & Kn < Kn_{Tmin}, \\ \left(\frac{1 - \frac{Kn_{Tmin}}{Kn}}{\frac{\epsilon}{\tau} D_{i,Kn}} + \frac{1 - \frac{Kn}{Kn_{Tmax}}}{\frac{\epsilon}{\tau} D_{i,j,St}} \right)^{-1}, & Kn_{Tmin} < Kn < Kn_{Tmax}, \\ \frac{\epsilon}{\tau} D_{i,Kn}, & Kn > Kn_{Tmax}. \end{cases} \tag{29}$$

The terms $\frac{Kn_{Tmin}}{Kn}$ and $\frac{Kn}{Kn_{Tmax}}$ weigh the diffusion coefficients of the Stefan and Knudsen diffusion regime, which reduces the offset at the transition points. The Knudsen transition fit parameters Kn_{Tmax} and Kn_{Tmin} allow adjusting the influence range of the transition between Stefan and Knudsen regimes. In the following, the model will be tested with the transition values of $Kn_{Tmin} = 0.1$ and $Kn_{Tmax} = 10$. It must be noted that the diffusion coefficient of the SKT-model with these transition values is alike the diffusion coefficient of the Bosanquet equation. However, the idea is that the SKT-model with a suitable combination of transition values and characteristic lengths may describe the diffusion in a large spectrum of porous structures. This spectrum could range from porous membranes to backfills made of particles of various particle size distributions. This chapter aimed to discuss this idea. The following chapter aims to compare the model to experimental data of one backfill. A full evaluation of this model for multiple structures will not be provided here.

5.4 Pressure influence on mass transport

The pressure during drying influences the diffusion regime within a porous structure, which is quantified by the Knudsen number. If the pressure is low enough and the mass transport takes place in the Knudsen regime, the diffusion coefficient of a molecule in the gas phase of a porous structure is not a function of pressure. For the industrial application of vacuum post-drying of electrodes in coil format, this phenomenon may limit the acceleration potential of pressure reduction. This expectation can be confirmed by:

- either measuring identical drying curves at two different pressures, low enough to evoke mass transport in the Knudsen regime,
- or validating the SKT-model (compare chapter 5.3) in the transition range, which includes the deceleration of mass transport towards low pressure.

The experimentally available pressure range in combination with the samples' pore diameter does not enable experiments necessary for confirmation 1. However, it is possible to dry the backfill made of anode active material in the transition range. Therefore, the validation of the SKT-model (confirmation 2) will be carried out. This form of validation requires the comparison of experiments and simulation, which enables the validation of the modeled effective diffusion coefficient by the experiment. If the simulations with the SKT-model describe the experiments at different pressures, the model is validated. The pressure ranges from 800 to 20 mbar at 30 °C. Table 5.1 lists three pressures with the respective Knudsen number and possible diffusion coefficients of water in a porous structure with an average pore diameter of 2 µm. The average pore diameter of 2 µm was chosen based on the mercury intrusion porosimetry of the graphite (compare Figure 8.1 in the appendix).

Table 5.1: Pressure with the respective Knudsen number, the effective diffusion coefficient of water in a porous structure with an average pore diameter ($L_{characteristic}$) of 2 µm and a porosity of 61 % ($D_{SKT,water}$), the effective diffusion coefficient of water in nitrogen, and the effective Knudsen diffusion coefficient of water in a 2 µm pore.

Pressure / mbar	Knudsen number / -	$D_{water,SKT}$ / m^2 s^{-1}	$D_{water,N_2,Stefan}$ / m^2 s^{-1}	$D_{water,Knudsen}$ / m^2 s^{-1}
20	3.3	1.3e-4	5.0e-4	1.5e-4
100	0.7	6.7e-5	1.0e-4	1.5e-4
800	0.08	1.3e-5	1.3e-5	1.5e-4

20 mbar of pressure result in a Knudsen number of 3.3 in the average pore, allocating the mass transport in the transition regime. This number is by a factor of 3 smaller than the Knudsen transition number (10). However, the comparison of the expected diffusion coefficients shows that the difference between the diffusion coefficient of Knudsen and the one of the SKT-model is small. Therefore, this pressure is not ideal to show the necessity of the SKT-model. Likewise, the pressure of 800 mbar with a Knudsen number of 0.08 evokes a diffusion in the Stefan regime. This means the diffusion coefficient of the transition model and the Stefan diffusion coefficient is the same. Therefore, this pressure is also unsuitable to test the SKT-Model.

For the average pore diameter of 2 µm, the 100 mbar-pressure drying falls into the transition region. With a Knudsen number of 0.7, it is close to the logarithmic middle between minimal and maximal Knudsen transition. This Knudsen number reflects in the diffusion coefficients. The three expected diffusion coefficients are different from each other and the one of the SKT-model is slowest. Therefore, the simulation with the Stefan and Knudsen diffusion coefficient is expected to suggest a quicker drying than experimentally observed, while the simulation with the SKT-model matches the experiment best. These results are displayed in Figure 5.6.

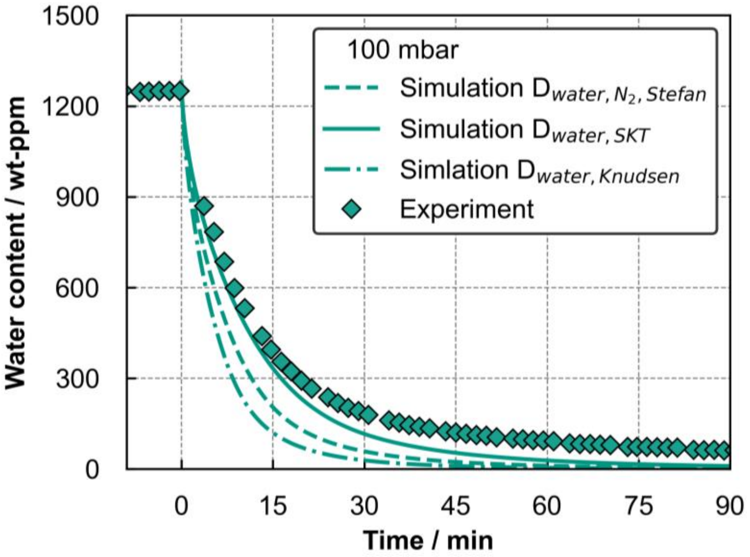

Figure 5.6: Drying of a backfill of anode active material. The experiments were conducted at 30 °C, 100 mbar, a porosity of 61%, and a height of the backfill of 40 mm. The simulation with the transition model (SKT-model) matches the experiment best. Pure Stefan and pure Knudsen diffusion coefficients predict a faster desorption than experimentally observed. The water content of the simulation with the Knudsen diffusion coefficient reaches 300 wt-ppm after 10 minutes while the simulation with the SKT-model predicts 600 wt-ppm after 10 minutes. This prediction of the simulation with the SKT-model matches the experimentally measured water content in the sample best. Experimental date reprinted with permission from (Heckmann et al., 2023).

The data in Figure 5.6 show the water content over time in minutes. For the drying at 100 mbar, the simulation results with the Stefan and Knudsen diffusion coefficient are both faster compared to the experiment. The simulation with the SKT-model provides the best replication of the experiment out of the three simulations. However, while this simulation matches the experiment above 300 wt-ppm, the accuracy decreases with increasing time. Focusing on the drying above 300 wt-ppm, these results show that the simulation with the SKT-model that takes the transition between the mass-transport regimes into account is necessary to describe the drying. It indicates that the average pore-diameter is suitable to approximate the mass transport in the porous structure.

The shape of the drying curve at 100 mbar resembles the drying curve of the PVDF anode in Figure 4.11. This resemblance is worth mentioning because the active material of the PVDF anode is the same as of the backfill. Like the drying of the backfill in Figure 5.6, the drying of the PVDF anode could not be described with a single constant diffusion coefficient. This means that the reason for the deviation towards the end of the experiment could be a second mass transport resistance as discussed in the previous chapter. The decreasing accuracy of the simulation with the SKT-model at 100 mbar can be further investigated by plotting the water content logarithmically. The slope of an arbitrary drying curve simulated with one constant diffusion coefficient is approximately a straight on a logarithmic scale. Therefore, if the experiments deviate from a straight, it indicates that multiple mass-transport resistances are at work. Figure 5.7 shows the drying experiments and respective simulations on a logarithmic scale. This Figure also shows the drying results for other pressures, to provide further evidence that the SKT-model is applicable.

The data in Figure 5.7 display the water content logarithmically over time in minutes, showing the initial slope of the drying curves. The Figure also shows the time frame, where the drying experiments at the lowest three pressures deviate from their simulations. The initial slope of the drying curve is a function of the drying pressure. The desorption of water is quicker for lower pressures. The initial slope of the drying curve at 20 and 40 mbar are closest together, which indicates the dominance of the Knudsen regime. The simulations with the SKT-model match the initial slope of the experimental drying curves. The simulations of the three lowest pressures deviate from the experiment below a mass loading of 300 wt-ppm.

The acceleration of the initial slope in the drying curve by pressure reduction matches the expectations of the diffusion coefficient modeled by the SKT-model (compare Figure 5.5). The increase of this diffusion coefficient by pressure reduction is larger for Knudsen numbers below 1 than for Knudsen numbers above 1. This theory is confirmed by the initial slope of the drying curves. The drying at 100 mbar has an average Knudsen number of ~0.7, and the acceleration of the drying from 800 to 100 mbar is larger than the acceleration from 100 to 20 mbar.

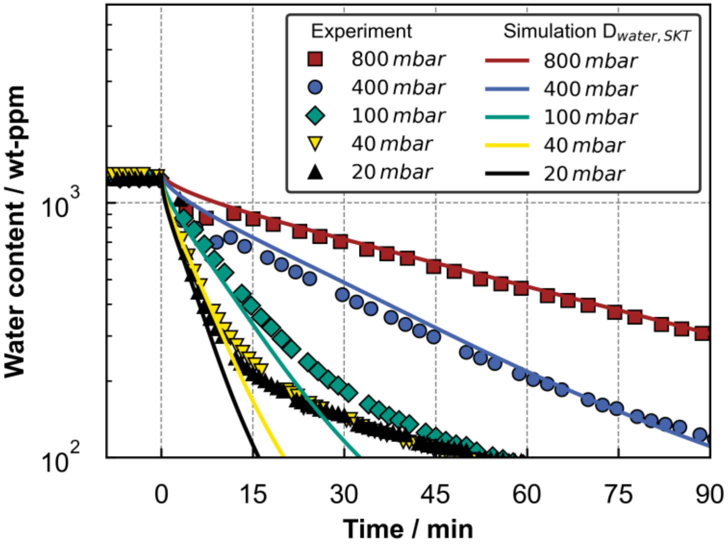

Figure 5.7: Pressure variation: Drying of a backfill of anode active material. The experiments were conducted at 30 °C, pressures of 800, 400, 100, 40, and 20 mbar, a porosity of 61%. The desorption at 100 mbar is the same as displayed in Figure 5.6. The simulations match the experiments in the beginning of drying for all pressures. The simulation predicts a faster desorption than experimentally observed below a water content of 300 wt-ppm for 20, 40, and 100 mbar. The drying curves of the experiments at low pressures have two slopes in a logarithmic plot, which indicates that multiple mass-transport resistances act. Experimental data reprinted with permission from (Heckmann et al., 2023).

The fact that the simulations with the SKT-model match the drying experiment initially at five pressures in the Stefan-Knudsen transition region suggests that the initial slope of the drying curves origins from the mass-transport resistance in the gas phase of the porous structure. The SKT-model uses an average pore diameter of 2 µm, which allows the simulation of the initial slope of the drying curves at all pressures. This result shows that this average pore-diameter in combination with the minimal and maximal Knudsen transition numbers enables the SKT-model to replicate the mass transport in the gas phase of the porous structure.

The unexpected deviation of the simulation of the drying curves at pressures 20, 40, and 100 mbar from the experiments indicates a second mass-transport resistance that affects the drying. The simulation with one mass-transport resistance is approximately a straight on a logarithmic water-loading scale (with constant coefficients). The experiments of the three lowest drying pressures follow that straight until a water content of ~ 300 wt-ppm. Surpassing this water content, the experimental drying decelerates. After a transition the water content decreases as a straight again, which could be a second mass-transport resistance. Emphasizing the deviation of simulation and experiment, Figure 5.8 shows the drying curves on linear scale at 400 and 40 mbar and their respective simulation on a larger time scale, compared to Figure 5.7.

The data in Figure 5.8 show the water content in wt-ppm over time in hours linearly. The experimental drying curves at 400 and 40 mbar are plotted with their respective simulations. These data confirm the observation of the previous Figure at larger time scale. The drying at 400 mbar can be described by the simulation with one mass-transport resistance. The drying at 40 mbar cannot holistically be described with a simulation with only one single mass-transport resistance. This simulation deviates below 300 wt-ppm of water content.

The experimental results confirm that a second mass-transport resistance affects the system only at pressures below 100 mbar. This means that:

- either the mechanism of this mass-transport resistance is activated at a certain pressure,
- or that the second mass-transport resistance only affects the drying if the drying is sufficiently fast.

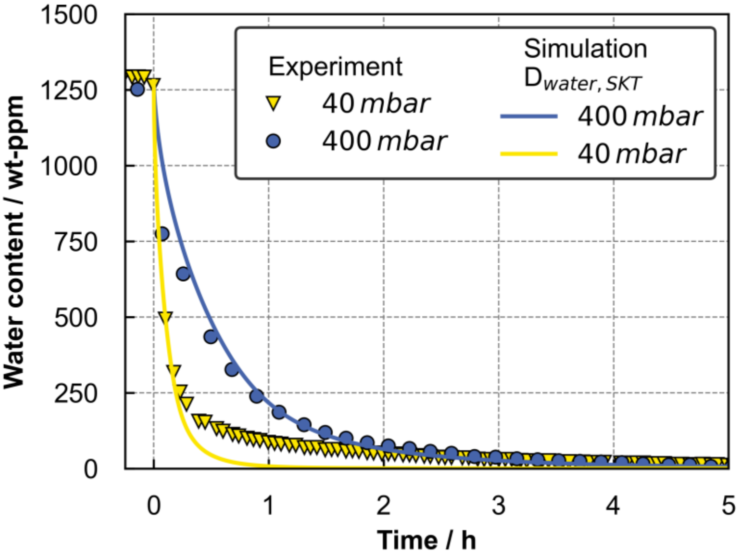

Figure 5.8: Drying of a backfill of anode active material. The experiments were conducted at 30 °C, 40 and 400 mbar, and a porosity of 61 %. The experiments and simulations are the same as display in Figure 5.7 on a linear y-scale. The quality of the experimental replication by the simulation decreases at low water contents at 40 mbar. The simulation predicts a faster desorption than experimentally observed. Experimental data reprinted with permission from (Heckmann et al., 2023).

One explanation for the observed phenomenon could be an external mass-transport resistance, e.g. due to a saturation of the measurement cell with water. The exchange of gas in the cell occurs at least twice per minute. An estimation of a saturation based on the desorbed water from the sample shows that this scenario is unlikely. Additionally, the gas exchange rates are different for every pressure, yet the second mass-transport resistance seems identical for every pressure. This phenomenon is also observed in drying experiments of anodes with the same active material, obtained with a different sample and higher gas exchange rates in the measurement chamber. This circumstance suggests that the second mass-transport resistance originates from a material property rather than saturation of the measurement cell.

Another explanation for the origin of the second mass-transport resistance could be the mass transport of water through inner pores of the active-material particles. The results of the porosimetry show one peak at 2 µm and another peak at 250 nm pore diameter (compare appendix 8.1). The overall volume of these pores is smaller by a factor of ten compared to the peak at 2 µm. The mass-transport regime in these pores would start in the transition regime, close to the Knudsen regime ($Kn = 7$ at 100 mbar) and range to the Knudsen regime ($Kn = 33$ at 20 mbar). Determining mass-transport properties such as an effective diffusion coefficient is not possible as porosity and tortuosity of this inner structure are unknown. Qualitatively however, this resistance would be approximately independent of pressure in the pressure range where it was observed. An estimation of the second mass-transport resistance with the Two-Scale-Model from chapter 4 is plotted in Figure 5.9.

The Two-Scale-Model describes a coupled mass transport, discussed in the previous chapter 4. If the second mass-transport resistance observed for low pressures, compare Figure 5.8, is indeed a mass-transport resistance within the particles, the Two-Scale-Model should describe the drying with the same diffusion time on micro scale for all pressures. The data in Figure 5.9 show the result for five pressures. The Two-Scale-Model can replicate the entire desorption of the graphite backfill by using a transition model for the gas-phase mass transport in the porous structure and the same constant diffusion time on micro scale for all pressures. While this is a good indication that the second mass-transport resistance is a plausible theory to explain the observed drying curves, it is not sufficient to draw final conclusions, due to the unknown inner particles structure.

Concluding this chapter, the pressure variation showed that the SKT-model is necessary, like the Bosanquet equation, to describe the mass transport in the gas phase of a porous structure. The investigated backfill made of graphite resembles a battery electrode, which constitutes the resistance on macro scale of water in LiB electrodes. The simulation with an average pore diameter in combination with the Knudsen transition values replicated the first part of all drying experiments. Therefore, if the mass-transport mechanism in this porous structure is diffusion, the Knudsen diffusion coefficient limits the achievable mass-transport acceleration by pressure reduction. The experiments from one porous structure cannot prove whether the SKT-Model is necessary or not. Experiments with other porous structures are necessary to determine the SKT-Model's necessity. The drying at low pressures showed that a second slow mass-transport resistance affects the drying after the mass transport of the gas phase in the porous structure.

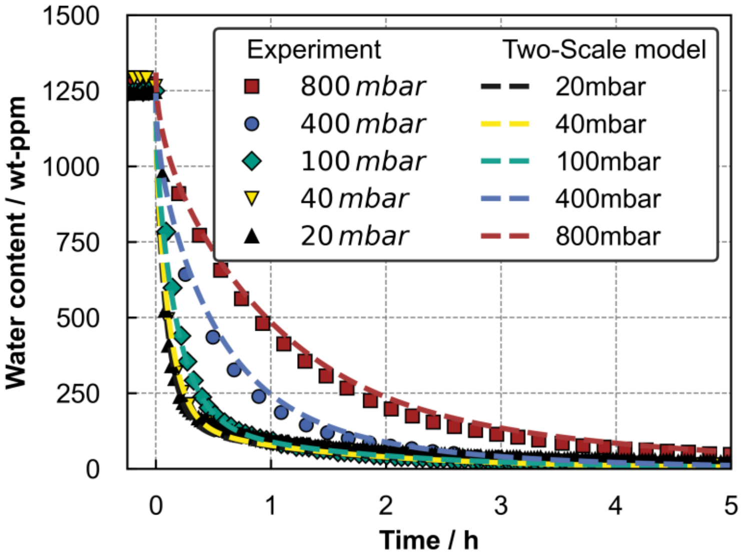

Figure 5.9: Experimental drying of the backfill made of anode active material compared to simulation with the Two-Scale-Model. This model can replicate the experimental drying with the same diffusion on micro scale at every pressure. This shows that a second mass-transport resistance in the graphite is plausible. Experimental data reprinted with permission from (Heckmann et al., 2023).

6 Sorption of water and CO_2 in cathode active material[12]

The previous chapters regarded a sorption model for electrodes as well as the mass transport on macro scale by probing anodes, and the active material of anodes. The sorption of water on micro scale in graphite anodes has been characterized regarding equilibria and their respective kinetics (Eser, 2021). In contrast, the sorption of water and CO_2 in the cathode active materials (CAM) requires additional research, regarding moisture management and post-drying. Substances in the air, namely water and CO_2, may chemically react with the CAM. Commonly discussed products of the reactions between water and CO_2 and layered oxide crystals of e.g. $Li[Ni_{0.6}Co_{0.2}Mn_{0.2}]O_2$ (NMC-622) are hydroxides and carbonates. The following general equations show these reactions with M abbreviating metal (Sicklinger et al., 2019).

$$MO + H_2O \rightarrow M(OH)_2 \tag{30}$$

$$MO + CO_2 \rightarrow MCO_3 \tag{31}$$

Most authors attribute the majority of the hydroxide and carbonate formation to lithium (Renfrew et al., 2019; Schuer et al., 2022; Shkrob et al., 2017; Wood et al., 2020). Other authors discuss the hydroxide and carbonate formation of nickel and also other transition metals (Chen et al., 2023; Sicklinger et al., 2019). While the chemical reactions between the CAM and water and CO_2 from the atmosphere as well as the characterization of the reaction products are known, knowledge about the kinetics relevant for the production processes of LiB is absent. The following chapter will focus on mass-uptake kinetics of the CAM “lithium-nickel-manganese-cobalt-oxide” (mostly NMC-622), aiming to determine governing kinetics of NMC-622

---

[12] Data presented in this chapter are published as a peer-reviewed article. This publication is a collaboration between the TFT from KIT and the iwb from the Technical University of Munich.

exposed to various atmospheres containing water and CO_2. The following hypothesis will be either verified or falsified.

The reaction kinetics of NMC-622 with water and CO_2 *determine the mass-uptake kinetics of this cathode active material.*

Eser et al. characterized the sorption of water in the additives in cathodes, which is a necessary basis for the interpretation of the upcoming results (Eser, 2021). They found that the additives of cathodes physically sorb water, which excludes these additives from being responsible for the chemical sorption of water in a cathode. Initially, the sorption behavior of cathodes in humid air must be considered to show a fundamental difference to the sorption behavior of anodes in humid air. Subsequently, the sorption behavior of the active material NMC-622 must be assessed individually in different atmospheres to isolate the sorption of the water and CO_2 in NMC-622. The reversibility of the mass uptake in the different atmospheres supports conclusions about sorption mechanisms.

The following discussions assume that the products of the chemical sorption reported by Zou et al. are lithium hydroxide and lithium carbonate, in accordance with other studies (Schuer et al., 2022; Zou et al., 2020). In particular, their observation that the lithium hydroxide layer passivates, while the lithium carbonate layer does not, is crucial to the discussion of the following results.

6.1 Sorption of water and CO_2 in NMC-622 and NMC-811 cathodes[13]

The sorption mechanisms of water in graphite anodes are adsorption and absorption (Eser et al., 2020c). This fact has been shown for atmospheres made of water and nitrogen. In contrast to the physical sorption of water in

---

[13] Aliénor Potthoff dedicated her master’s thesis to the investigation of the sorption behavior of water and CO_2 in cathodes of LiB.

anodes, the CAM NMC has been shown to chemically interact with water and additionally with CO_2 (Kosfeld, 2024; Schuer et al., 2022; Shkrob et al., 2017; Wood et al., 2020; Zou et al., 2020). The following experiment aims to show that the sorption behavior of anodes is unaffected by the presence of CO_2 in humid air. Additionally, the experiment aims to demonstrate the general difference between the sorption behavior of graphite anodes and NMC-cathodes in humid air. Figure 6.1 shows this long-term sorption experiment of two NMC-cathodes with PVDF binder and one graphite-anode with CMC/SBR binder in humid air. The experiment lasted several months at room temperature and a relative humidity of 72%.

The data in Figure 6.1 show the mass uptake over time in days. In contrast to figures in this thesis of physical sorption of water, the y-axis shows the general mass uptake because water and CO_2 chemically react with the cathodes. Therefore, it cannot be distinguished which molecules attach. The time scale of this experiment in a desiccator is large (exposure time ~ 100 days) compared to sorption experiments in the MSB (exposure time ~ 5 days), which demonstrates the difference between the sorption mechanisms of the electrodes. The relative humidity of 72 % at room temperature is rather high, intentionally emphasizing sorption effects. Each data point of the cathodes is the average of three samples and each data point of the anodes is the average of two samples. The samples and sample containers have the same geometry, to avoid any influence on the mass uptake.

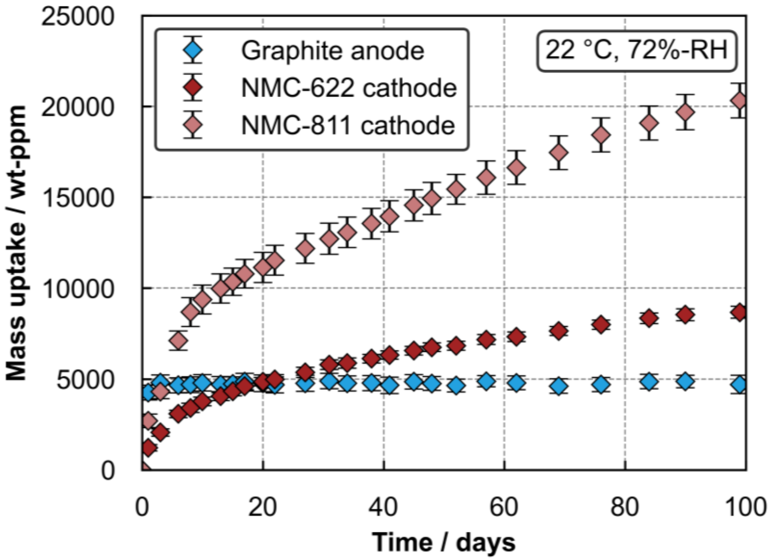

Figure 6.1: Sorption experiments of graphite anodes with a CMC/SBR-binder system, NMC-622 and NMC-811 cathodes with a PVDF binder system. The anode expresses a sorption-curve characteristic for physical sorption. The mass uptake of the cathodes prevails with changing rates over time. The chemistry of the active material affects this mass uptake. Experimental data reprinted with permission from (Heckmann et al., 2026b).

The anodes reach the equilibrium within two days, which is fast compared to the cathodes. This observation confirms kinetic data from Eser, who showed that anodes physically ab- and adsorb water (Eser et al., 2020b). The presence of oxygen and CO_2 does not affect this equilibrium. If the mass loading of the anodes remains constant over time, the humidity and temperature in the desiccator must be constant. Therefore, the anodes also serve as additional control to assure constant humidity and temperature conditions in the desiccator.

The cathodes behave differently, the mass uptake of the NMC-622 and NMC-811 cathodes is initially slower than the mass uptake of the anodes.

However, the mass uptake of the cathodes continues and exceeds the one of the anodes. Both cathode samples do not reach an equilibrium with the humid air inside the desiccator within three months. This result shows that the sorption mechanisms of the anode and the cathode occur on different time scales (days vs. months). This circumstance indicates that the sorption of water and CO_2 in the cathodes is slower compared to the physical sorption of water in the anodes.

Further analysis of the kinetics of the mass uptakes shows that the mass transport of water to the surface of the electrodes does not limit the mass uptake of the cathodes. If this was the case, the cathodes would adsorb water at least as fast as the anodes. The cathodes take up mass slower than the anodes even though they react with CO_2 as well. This shows that the mass transport of water to the surface of the cathode does not limit the cathodes mass uptake. The NMC-811 sorbs water and CO_2 quicker than NMC-622. This circumstance indicates that the reactions on the surface limit the mass uptake for this sample geometry and active material morphology. If the mass transport of CO_2 to the surface of the CAM was limiting, the mass-uptake rate should not be a function of the material chemistry. Therefore, the material properties are decisive for the mass-uptake rate.

This experiment shows the fundamental difference between sorption of water in graphite anodes and sorption of water and CO_2 in NMC cathodes. The results show that a humid atmosphere (72 %-RH) evokes a larger mass uptake in the cathodes compared to the CMC/SBR anode. The kinetics of the sorption show that the CAM chemistry affects the uptake rate and amount of mass uptake. This observation indicates that the reaction kinetics of the cathode with water and CO_2 determine the mass uptake (hypothesis 3). Based on the different time scale on which the sorption of water and CO_2 in the NMC cathodes occurs and knowledge from literature, this large mass uptake is attributed to chemical sorption. This chemical sorption originates from the CAM rather than other components of the cathode (Eser, 2021). Therefore, the active material will be probed individually in the following. All following experiments were conducted with CAM in powder form.

6.2 Sorption behavior of NMC-622 in humid air vs humid nitrogen[14]

The atmosphere composed of air with a RH of 72 % results in a large mass uptake of the cathodes. However, the time scale and the humidity of the experimental data plotted in Figure 6.1 are large compared to industrially relevant production processes. In the following the sorption behavior of the CAM NMC-622 at lower relative humidity is considered in addition to the influence of the gas-phase composition. As CO_2 is an educt of the chemical reaction of hydroxides to carbonates, the change in atmosphere composition is expected to change the sorption characteristics. The data in Figure 6.2 show the sorption behavior of NMC-622 in a nitrogen-water atmosphere compared to humidified air.

Figure 6.2 displays the mass uptake to 400 wt-ppm over time to four days. The temperature is 30 °C with a RH of 2.3 %, which is equivalent to a dew-point temperature of -20 °C. The sorption was measured with the perfusion sorption apparatus. The sorption behavior of NMC-622 in humidified nitrogen has a different characteristic compared to the sorption behavior of NMC-622 in humidified air. The mass uptake in humidified nitrogen rises to 50 wt-ppm within the first hours and then the uptake decelerates, which results in a final mass uptake of 60 wt-ppm. The mass uptake in humidified air also has a steep rise in the first hours. This mass uptake also decelerates; however, the slope of the uptake curve is large and continues over the period of the experiment.

---

[14] Lukas Madlindl dedicated his master's thesis to the investigation of the sorption mechanisms of water and CO_2 in the cathode active material NMC-622.

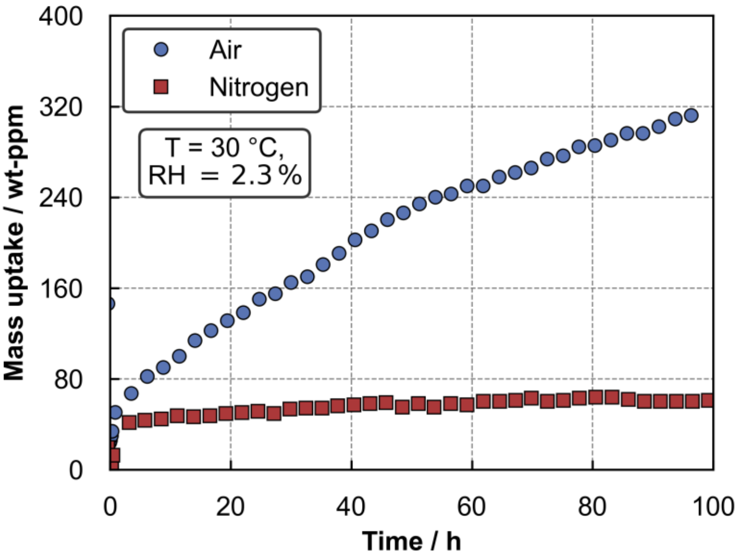

Figure 6.2: Sorption behavior of the CAM NMC-622 as powder in the humidified atmospheres nitrogen and air. The characteristics of the mass uptake depend on the atmosphere. At 2.3 %-RH, the contact with air with ~ 400 vol-ppm of CO_2 and ~ 20 vol-% O_2 results in a larger mass uptake rate compared contact with nitrogen as 2.3 %-RH. Lou et al. showed that this difference in mass uptake must result from the presence of CO_2. Experimental data reprinted with permission from (Heckmann et al., 2026b).

Results from Zou et al. and others suggest that the sorption of water and CO_2 in NMC-622 origins from the chemical reaction of NMC-622 with water and CO_2. If the exposure to humidified nitrogen evokes a chemical reaction to hydroxides, the total amount of reacted CAM would only result in a mass gain of 50 wt-ppm. According to Zou et al. the formation of lithium hydroxide is self-passivating, which could explain the constant mass at the end of the experiment. It is also possible that other sorption mechanisms are responsible for the mass uptake. The sorption behavior of the NMC-622 in air with ~ 400 vol-ppm CO_2 could be explained by the formation of lithium carbonate.

This reaction is not passivating and continues for an extended period (compare Figure 6.1).

This experiment shows that the atmosphere is decisive for the characteristics of sorption. A further analysis of this experiment gives information about the mechanisms that are responsible for the sorption process. The energy that is necessary to desorb sorbate from sorbent is larger for chemical sorption than for physical sorption. Therefore, the samples from Figure 6.2 were exposed to different temperatures in dry (dew-point temperature of -65 °C) nitrogen. Figure 6.3 shows the results of this desorption.

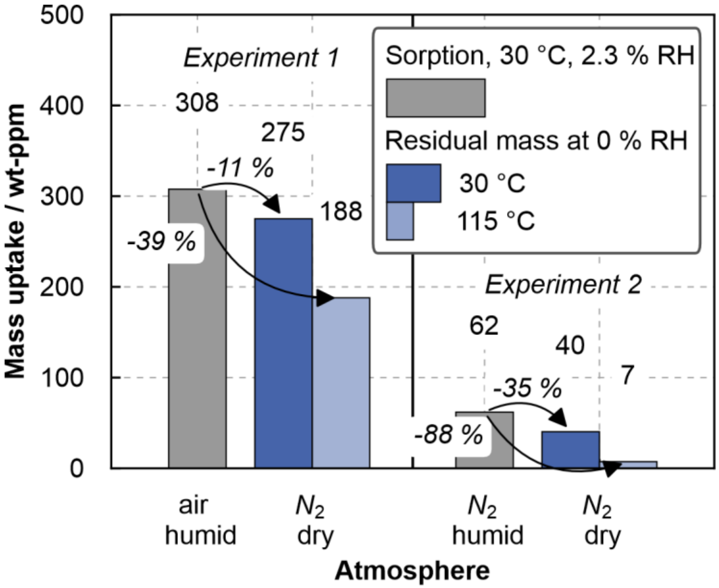

Figure 6.3: Desorption of the samples from Figure 6.2. These samples were exposed to dry nitrogen until their weight was constant, at first at 30 °C followed by 115 °C. Both temperatures are below the degradation temperatures of lithium oxide and lithium carbonate. While almost all the mass that sorbs in humidified nitrogen desorbs, ~ 60% of the mass that sorbs in humidified air does not desorb. Experimental data reprinted with permission from (Heckmann et al., 2026b).

The data in Figure 6.3 show the mass uptake at the end of the experiments from Figure 6.2 after desorption at 30 °C, and after desorption at 115 °C. After exposure to humidified air, 11 % of the mass uptake desorbs at 30 °C and 39 % desorbs at 115 °C. In contrast, after the exposure to humidified nitrogen, 35 % of the mass uptake desorbs at 30 °C and 88 % desorbs at 115 °C. The 30 °C provide sufficient energy to desorb lightly bound physically sorbed species. The degradation temperature of lithium hydroxide and lithium carbonate are ~ 400 °C and ~ 725 °C, respectively, according to Sicklinger et al. (Sicklinger et al., 2019).

This observation shows that the sorption mechanisms of the mass uptake of NMC-622 in humidified air and nitrogen are not the same. The CO_2 content of 400 vol-ppm in ambient air suffices to change the sorption mechanism. The chemical sorption in form of carbonates is likely. Unexpected is the desorption of the mass uptake in nitrogen. If the mass uptake originated from the chemical sorption in the form of lithium hydroxides, the mass uptake should not be mostly reversible as observed. Therefore, other mechanisms appear to be responsible for the mass uptake of NMC-622 in humidified nitrogen. These results raise two questions:

1. Which sorption mechanism is responsible for the reversible mass uptake of NMC-622 in humid nitrogen at 115 °C?
2. Which components form during the exposure of NMC-622 in air that do not decompose at 115 °C?

The formation of hydrates in the NMC-622 crystal is discussed as a possible explanation to question 1 in one of my publications[15]. Question 2 will be assessed via a calculation based on the mass uptake observed during exposure of NMC-622 in air. Zou et al. suggest that lithium reacts to hydroxides and carbonates. Sicklinger et al. conducted TGA measurements that suggest

---

[15] This experimental study showed a large water uptake of NMC-622 after the surrounding atmosphere exceeded a certain RH. A calculation showed that the formation of LiOH hydrates is thermodynamically possible. The reversibility of the water uptake confirmed some aspects of the hypothesis that hydration of LiOH is responsible for the water uptake, while other aspects were falsified. Further detail can be found in the publication (Heckmann et al., 2024).

that nickel reacts to basic nickel carbonate. The gravimetric results can be compared to a mass balance based on the reaction equations of the NMC-622 with water and CO_2. The chemical reactions are:

$$Li_2O + H_2O \rightarrow 2LiOH \tag{32}$$

$$2LiOH + CO_2 \rightarrow Li_2CO_3 + H_2O \tag{33}$$

$$3NiO + CO_2 + 6H_2O \rightarrow NiCO_3 \cdot 2Ni(OH)_2 \cdot 4H_2O \tag{34}$$

The following assumptions and data are necessary to obtain the results shown in Figure 6.4:

- The entire mass uptake after the desorption at 115 °C originates from the chemical reactions
- The mass uptake based on the lithium reactions is calculated assuming that 50 mol-% of the mass uptake originates from reactions 32 and 50 mol-% of the mass uptake originates from reaction 33
- A uniform grid parameter of 2.89 Å[16] is assumed for the crystal lattice in NMC-622
- The BET-surface of the NMC-622, obtained from the manufacturer, is used to quantify surface atoms

Two scenarios are plausible: either the chemical reactions are passivating, which would result in a reaction on the surface of the NMC-622 crystal, or the reaction eventually deteriorates the entire crystal and transforms all the Li and Ni into hydroxide and carbonate. The grid parameter and BET-surface of the NMC-622 estimate how many atoms of Li and Ni are present on the surface of the active material particles. The chemical formula gives the overall mass fractions of the elements. If the mass of atoms either on the surface of the particles or on the surface and bulk match the mass uptake during the experiment for either chemical reaction, it would indicate which species form and where they form.

---

[16] This is a simplification because the NMC-622 crystal has orientation-dependent grid parameters.

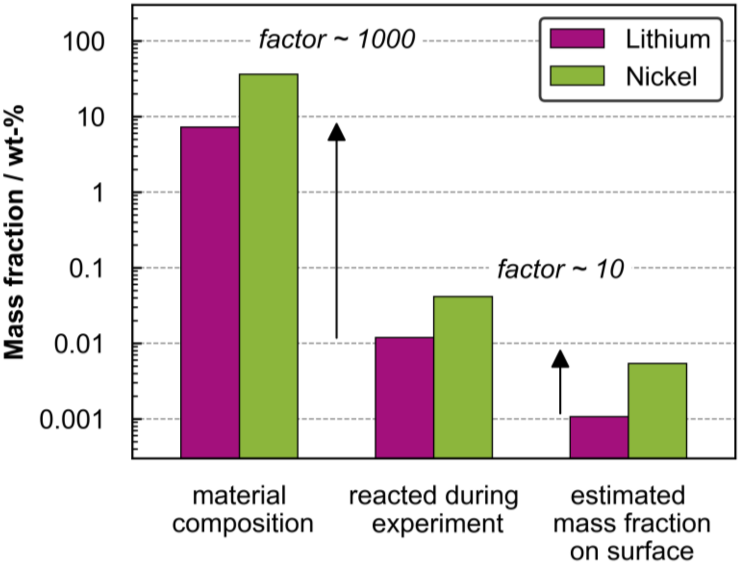

Figure 6.4: Mass balance for the sorption of water and CO_2 in NMC-622 from Figure 6.2. According to the reaction equations from literature, only a small fraction of the available Li and Ni reacts during the experiment. However, the atoms on the surface of the NMC-622 do not suffice to explain the gravimetrically observed mass uptake. Experimental data reprinted with permission from (Heckmann et al., 2026b).

The data in Figure 6.4 show the mass fractions of the entire NMC-622 crystal as well as the mass fraction of the surface atoms of Li and Ni. The bars in the middle show the mass of the consumed Li and Ni by the chemical reactions 32-34 based on the experimental mass uptake. The mass fractions range across several orders of magnitude and are plotted on a logarithmic y-scale. Compared to the entire Li and Ni content in NMC-622, the reacted mass of Li and Ni is ~ 1000-times smaller. Compared to the Li and Ni atoms on the surface, the number of reacted atoms is ~ 10-times greater. The estimates don't match for either element, therefore, conclusions about which species form are not possible. However, it is possible to conclude that the surface atoms do not suffice to explain the mass uptake that remains after the 115 °C desorption. Therefore, crystal layers beneath the surface must be affected by the degradation. The degradation after four days in humid air with a dew-point temperature of -20 °C affects a very small fraction (0.1 wt-%) of the overall mass in the NMC-622.

The sorption behavior of NMC-622 in humid air versus humid nitrogen expresses distinct characteristics regarding mass-uptake rate and reversibility of the mass uptake. During exposure to humid nitrogen, the NMC-622 reaches an equilibrium within four days and the mass uptake is mostly reversible at 115 °C, indicating that no hydroxides form. The mass uptake during exposure of NMC-622 in humid air continues for four days and is not reversible at 115 °C, indicating that either hydroxides, carbonates, or both, form. Overall, the mass uptake in air at a relative humidity of 2.3 % (dew point temperature of -20 °C) is small after four days, considering the available number of atoms in the NMC-622. Building on these results, the influence of the CO_2 content in the gas phase on the mass uptake will be evaluated.

6.3 Sorption behavior of NMC-622 under variable CO_2 concentration

The previous results show general characteristics of the sorption behavior of NMC-622 under humid conditions with and without CO_2. The dependency of the mass uptake on RH and CO_2 content in air must be understood to determine critical kinetics for the detrimental mass uptake. The long exposure experiments, plotted in Figure 6.1 and Figure 6.2, show that the mass-uptake rate remains positive for an extended period of time. This makes it experimentally challenging to measure until an equilibrium is reached. Therefore, in additional experiments, the CO_2 content was varied by artificially mixing pure gases. As there is no indication in literature that NMC-622 reacts with O_2, and to isolate the effects of water and CO_2 on the mass uptake, artificial atmospheres were mixed without O_2. The CO_2 content in the artificial gas is adjusted via the set-point values of the mass-flow controllers. Figure 6.5

displays data of the mass uptake of NMC-622 in humidified nitrogen with additional CO_2 over a period of four days.

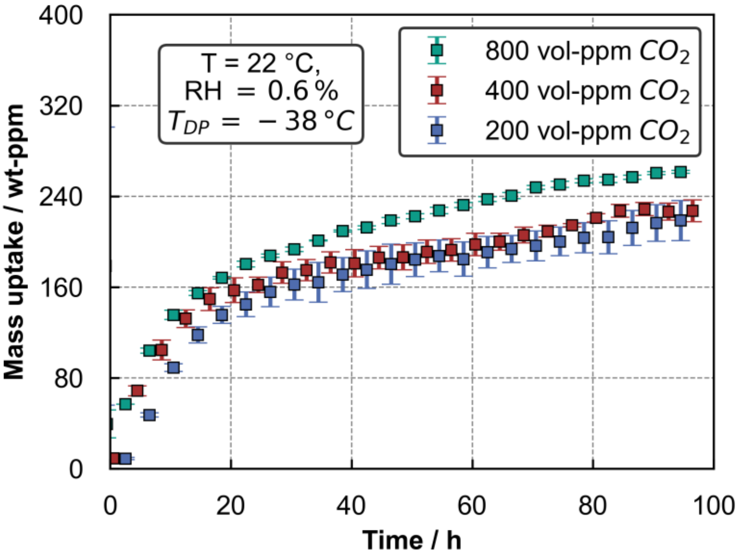

Figure 6.5: Exposure of NMC-622 to a humidified nitrogen-CO_2 atmosphere. The CO_2-content varies. The mass uptake at a dew-point temperature of -38 °C at 22 °C sample temperature is small over four days. The CO_2 content affects the mass uptake of the NMC-622. Experimental data reprinted with permission from (Heckmann et al., 2026b).

The atmospheric conditions are close to room temperature and the dew-point temperature is -38 °C[17]. This dew-point temperature results in ~160 vol-ppm water in the atmosphere. The CO_2 content in the atmosphere varied between 200 vol-ppm and 800 vol-ppm. Each data point is the average of two measurements with the respective standard error. The mass uptake increases with increasing CO_2 content in the atmosphere. The data points of 200 vol-ppm

---

[17] Close to the industrial standard dew-point temperature of -40° C for NMC-622 cathodes.

CO_2 rise the slowest and approach the mass uptake at 400 vol-ppm CO_2 towards the end of the experiment. The mass uptake at 400 and 800 vol-ppm CO_2 are alike in the beginning of the experiment and the mass uptake at 800 vol-ppm CO_2 rises further towards the end. Considering the error bars, the measurements of the mass uptake at 200 and 400 vol-ppm CO_2 are not significantly different, as the error bars overlap. The measurement of the mass uptake at 800 vol-ppm CO_2 is significantly different to the other measurements.

The results plotted in Figure 6.5 show that the CO_2 concentration of the gas phase affects the mass uptake of NMC-622 at a dewpoint of -38 °C. This is indicated by the mass uptake of NMC-622 during exposure to atmospheres with 800 and 400 vol-ppm CO_2. The reduction to 200 vol-ppm CO_2 in the atmosphere follows the trend. The error bars of the measurements with 200 vol-ppm are large compared to the other experiments. It is possible that the gas-mixing was flawed because the volume flow of CO_2 was close to the limit of the mass-flow controller. The effect of the CO_2 concentration reduction is small compared to the overall mass uptake. The variation of the CO_2 concentration in the atmosphere had little effect on the mass uptake of the NMC-622 at a dewpoint temperature of -38 °C. This observation shows that either the mass transport of CO_2 to the surface of the active material particles or the reaction to carbonates limits the mass uptake. As a first estimation: doubling the gradient of the mass transport would double the uptake rate. This is not observed by increasing the CO_2 concentration from 400 to 800 vol-ppm. Calculating the transient gas-phase mass transport inside the sample shows that theoretically sufficient CO_2 molecules are available on the surface of the NMC-622 to absorb a larger amount of mass (compare appendix 8.11) than experimentally observed. These circumstances indicate that the reaction limits the mass uptake during the sorption.

The low water content in the atmosphere during this exposure could also influence the mass uptake and its kinetics. If the availability of water on the NMC-622’s surface was limiting the mass uptake, the CO_2 content should not affect the mass uptake at all. Even though the difference in mass uptake of the NMC-622 in atmospheres with CO_2 concentrations of 400 and 800 vol-ppm was small, the difference was observed. A possible explanation are the reaction equations 33 and 34. According to them, water is a product of the carbonate reaction, which could then again react to hydroxides.

A comparison of these results to the results from Figure 6.2 is only qualitatively possible because the dew-point temperature, RH, and temperature are different. The overall mass uptake during the exposure to all three CO_2 concentrations from Figure 6.5 is smaller than for exposure to air (see Figure 6.2). It is remarkable that the transition to the slower mass-uptake kinetic in this experiment is delayed, compared to Figure 6.2. These observations cannot be evaluated without further experiments. However, the experiments shown in this Figure do not equilibrate, the sorption characteristic is similar (two distinct kinetics) as for the NMC-622 exposed to air from Figure 6.2.

The differences between the sorption behavior of NMC-622 in humid air and humid nitrogen were shown. The reaction to carbonates is not passivating, which gravimetrically confirms the optical observations of other studies. Further assessment on which component in the gas phase affects the kinetics indicates that CO_2 limits the mass uptake. The following findings of the sorption experiments with water and CO_2 indicate that chemical sorption of CO_2 is the limiting kinetic of the mass uptake in NMC-622 (hypothesis 3):

- The chemistry of the CAM in NMC-811 and NMC-622 cathodes affects the mass-uptake rate in humid air. As both cathodes were exposed to the same atmosphere for the same time, it can be concluded that the reaction kinetics on the CAM limit the mass uptake. The mass uptake did not cease after three months, indicating that the chemical reaction does not passivate.
- The reaction to either hydroxides or carbonates or both could limit the mass uptake of NMC cathodes in humid air. NMC-622 exposed to an atmosphere with a dew-point temperature of -38 °C and various CO_2 concentrations expresses a small dependency of that mass uptake on the CO_2 concentration in the atmosphere. As theoretically more CO_2 molecules could attach to the surface of the NMC-622 than experimentally observed, it is concluded that the reaction to carbonates is a limiting kinetic.

7 Summary and Outlook

The results of this thesis are summarized in the following. Each of the hypothesis formulated in the beginning will be addressed individually. Subsequently, ideas to further advance the research in the field of moisture management and post-drying during the production of LiB will be formulated.

7.1 Summary

The hypotheses that guided the research of this thesis aim to understand the sorption of water and CO_2 in the electrodes of LiB. Ultimately, this understanding can support a demand-oriented moisture management and post-drying for an ecological and economical electrode production. A comprehensive simulation of these sorption processes can transfer research results to application in industry. Therefore, the focus in this thesis is modeling and experimentally investigating sorption processes.

The desorption of water from LiB electrodes during post-drying cannot be replicated by simulations that consider mass transport on only one scale. Therefore, it was hypothesized that a model that simulates two scales is necessary to describe the mass transport of e.g. water in an electrode (hypothesis 1). A numerical model, called the Two-Scale-Model, was developed to describe the overall mass transport in the composite structure of a LiB electrode. This model accounts for sorption on micro and macro scale and its respective mass-transport resistances in multiple phases and two directions. These mass transports are numerically coupled as a system of multiple PDEs. The diffusion time of the mass transport on each scale proves to be applicable to quantify the influence of the scale's mass-transport resistance on the overall mass transport of water in an electrode. Comparing the results of the Two-Scale-Model for the boundary cases of micro- and macro-scale-controlled mass transport to results of single-scale simulations shows the applicability of the diffusion times. Additionally, this comparison proves the correct implementation of the PDE system. After this theoretical consideration, the Two-Scale-Model was compared to vacuum drying experiments of PVDF and CMC/SBR anodes. The Two-Scale-Model provides a phenomenological simulation to model the vacuum drying with the mass transport of water through the porous electrode structure on macro scale and e.g. the mass transport of water in the binder on micro scale. A sample holder was developed that allows a time-resolved measurement of the drying propagation while resembling mass transport through an industrial coil. It was shown that the Two-Scale-Model is necessary to describe the mass transport of water in an electrode, which validates this first hypothesis for both anodes. The drying of the PVDF anode can be modeled with plausible mass-transport parameters for the gas phase within the porous structure of the electrode and a constant mass-transport resistance on micro scale. The drying of the CMC/SBR anode was also validated, however with a variable mass-transport resistance on micro scale. This behavior has been previously observed for the binder polymers of the CMC/SBR anode as well.

Having found a suitable Two-Scale-Model for the overall mass transport of water in an electrode, the second hypothesis probes the mass transport of water in the gas phase of the porous structure in an electrode (the mass transport on macro scale) in detail. Regarding post-drying in coil format under vacuum, the diffusion regimes of the gas phase as a function of pressure were investigated. Hypothesis 2 states that describing the mass transport of water through the gas phase in the porous structure of an electrode at low pressures requires a model that considers the mass transport in the Stefan-Knudsen transition regime. Initially, an experimental routine was developed to measure time resolved drying curves at vacuum conditions between 20 mbar and 800 mbar. A backfill made of graphite (the anode active material) serves as a porous structure that resembles an electrode. Experiments were evaluated by comparing them to a numerically solved water mass-balance of the sample. The experiments at 800 mbar can be described by the simulation for two mass-transport distances and two porosities. The comparison of the experiment and simulation at 800 mbar shows that the mass-transport resistance can be described by the diffusion of water through the gas phase of the porous structure. Experiments at pressures down to 20 mbar show that diffusion regimes change in the porous structure. This observation is accounted for by a transition model between Stefan (Fickian) and Knudsen diffusion. The Stefan-Knudsen-Transition (SKT) model is proposed to advance the Bosanquet equation, which allows the adjustment of the transition region between Stefan and Knudsen regime. Drying experiments between 20 and 800 mbar show that the SKT model is necessary to account for the mass-transport acceleration at low pressure correctly, using the Bosanquet equation is also possible. This result validates hypothesis 2: A transition model is necessary to describe the diffusion within a porous structure that resembles a LIB electrode. The accuracy of the simulation to describe the experiment decreases for low pressure. A second mass transport such as the one of water in the gas phase of inner pores of the graphite was discussed and considered plausible. From a technical perspective these results show: if the diffusion through the porous structure governs the mass transport during post-drying, the process can only be accelerated until Knudsen diffusion occurs.

Chapter six regards the sorption on micro scale of NMC-cathodes. This sorption can deteriorate the CAM and decrease performance of the LiB. The focus of this chapter is the chemical sorption of water and CO_2 on the active materials of the cathodes. Several sorption experiments provide data to evaluate if the reaction kinetic of NMC-622 with water and CO_2 determine the mass-uptake kinetics of this cathode active material (hypothesis 3). Long-term sorption in a desiccator at 70 %-RH shows the fundamental difference between the sorption behavior of an CMC/SBR anode as well as NMC-622 and NMC-811 cathodes. The chemistry of the cathode active material determines the mass-uptake rate of water and CO_2 in the cathodes. High nickel-content has the largest mass-uptake rate. As the sorption conditions of all samples were identical, the chemistry of the cathode active material must be responsible for the difference in mass-uptake rate. This observation indicates that the chemical reactions on the surface of the CAM restrict the mass-uptake rate. Additionally, the composition of the gas phase strongly affects the sorption behavior. The sorption in humid atmosphere without CO_2 shows a passivating effect. This gravimetrical result confirms visual observations from literature. The passivation effect vanishes when CO_2 is in the atmosphere. All sorption experiments with NMC-622 in humid atmospheres with CO_2 showed a constant mass uptake. An estimation based on possible reaction equations suggests that the mass uptake affects more than just the surface of the NMC, if CO_2 is in the atmosphere. A variation of the CO_2 content in the gas phase slightly influences the mass-uptake rate. This suggests that the reactions with CO_2 on the NMC are a limitation of the mass uptake. Whether the reaction kinetics of NMC-622 with CO_2 are the only limitation of the mass uptake of NMC-622 cannot be ascertained at this point. The results show that the CO_2 content in the atmosphere and the chemistry affect the mass uptake. However, other effects, such as lithium leaching of the NMC-crystal could also be a limiting factor.

The results of this thesis advance research regarding the sorption behavior of LiB electrodes during production and especially post-drying. The classification of the mass transport during sorption on micro and macro scale allows the distinction between various sorption mechanisms. The experiments and modelling of the vacuum drying of porous structure allow the simulation of post-drying processes controlled by macro-scale mass transport. The results of the sorption behavior of NMC-622 reveal governing kinetics of the sorption and show the difference to the sorption behavior of anodes. These results enable a phenomenological description of the sorption processes in electrodes, which allows the simulation of sorption in various electrodes and geometries.

7.2 Outlook

The previously summarized advances in the research of sorption during moisture management and post-drying during the production of LiB electrodes provide the basis for ample ideas for subsequent investigation.

The Two-Scale-Model requires further work regarding the modeling of the mass transport on micro scale. The results show that the experimentally determined diffusion time on micro scale did not align with literature data. The obvious difference between literature and these experiments is the structure of the polymer on micro scale itself. Literature provides mass-transport data for films made of the binder polymer, while the binder forms a network of random structures in the electrode. This geometrical difference could affect the mass-transport properties of the water in the polymer. Investigating the anodes without the influence of the mass transport on macro scale may isolate the mass transport on micro scale and allow conclusions about the effective mass-transport distance of water in a binder network. This would be possible by investigating free-standing electrodes at defined drying conditions.

The modeling of the mass transport on macro scale in this study was facilitated by simulating the diffusion of water through the porous structure of the electrode. The results show that transition models between Stefan (Fickian) diffusion and Knudsen diffusion are necessary to explain the experiments. An idea that modifies the Bosanquet equation is proposed, discussed, and successfully applied to the experiments in this thesis. However, experiments to show the necessity of the SKT-model rather than the Bosanquet equation cannot be provided in this study. Experiments that are a direct measurement of the diffusion coefficient must be carried out for multiple porous structures to provide this data.

The sorption experiments with the NMC-622 cathode active material allow first conclusions about restricting process parameters. Nevertheless, further experiments and especially models are necessary to enable the simulation of this sorption and desorption behavior. In the case of the NMC-622, reaction limitation and mass-transport resistances could both affect the sorption. The modeling of these effects would enable a degradation prediction for these moisture sensitive cathode active materials.

References

Altvater, A., Heckmann, T., Eser, J.C., Spiegel, S., Scharfer, P., Schabel, W., 2023. (Near-) Infrared Drying of Lithium-Ion Battery Electrodes: Influence of Energy Input on Process Speed and Electrode Adhesion. Energy Technol. 11, 2200785. https://doi.org/10.1002/ente.202200785

Aurbach, D., Weissman, I., Zaban, A., Dan, P., 1999. On the role of water contamination in rechargeable Li batteries. Electrochimica Acta 45, 1135–1140. https://doi.org/10.1016/S0013-4686(99)00312-6

Bauer, R., 1977. Efektive radiale Wärmeleitung gasdurchströmter Schüttungen mit partikeln unterschiedlicher Form und Größenverteilung. Technische Hochschule Karlsruhe.

Börnhorst, T., 2021. Über die Diffusions- und Relaxationsprozesse bei der Trocknung von nanometerskaligen Polymerschichten. Karlsruher Institut für Technologie (KIT).

Börnhorst, T., Frankenhauser, L., Scharfer, P., Schabel, W., 2020. Drying kinetic measurements of polymer nanolayers – Experimental results with a model-based validation and interpretation of solvent diffusion. Polymer 200, 122595. https://doi.org/10.1016/j.polymer.2020.122595

Börnhorst, T., Scharfer, P., Schabel, W., 2021. Drying Kinetics from Micrometer- to Nanometer-Scale Polymer Films: A Study on Solvent Diffusion, Polymer Relaxation, and Substrate Interaction Effects. Langmuir ACS J. Surf. Colloids 37, 6022–6031. https://doi.org/10.1021/acs.langmuir.1c00641

Bosanquet, C.H., 1944. Wall effects in gas-temperature measurements. Br. TA Rep. BR-507.

Bruggeman, D.A.G., 1935. Berechnung verschiedener physikalischer Konstanten von heterogenen Substanzen. I. Dielektrizitätskonstanten und Leitfähigkeiten der Mischkörper aus isotropen Substanzen. Ann. Phys. Chem. 416, 636–664. https://doi.org/10.1002/andp.19354160705

Brunauer, S., Deming, L.S., Deming, W.E., Teller, E., 1940. On a Theory of the van der Waals Adsorption of Gases. J. Am. Chem. Soc. 62, 1723–1732. https://doi.org/10.1021/ja01864a025

Brunauer, S., Emmett, P.H., Teller, E., 1938. Adsorption of Gases in Multimolecular Layers. J. Am. Chem. Soc. 60, 309–319. https://doi.org/10.1021/ja01269a023

Bryntesen, S.N., Strømman, A.H., Tolstorebrov, I., Shearing, P.R., Lamb, J.J., Stokke Burheim, O., 2021. Opportunities for the State-of-the-Art Production of LIB Electrodes—A Review. Energies 14, 1406. https://doi.org/10.3390/en14051406

Burganos, V.N., 1998. Gas diffusion in random binary media. J. Chem. Phys. 109, 6772–6779. https://doi.org/10.1063/1.477323

Burganos, V.N., Sotirchos, S.V., 1987. Diffusion in pore networks: Effective medium theory and smooth field approximation. AIChE J. 33, 1678–1689. https://doi.org/10.1002/aic.690331011

Burns, J.C., Sinha, N.N., Jain, G., Ye, H., VanElzen, C.M., Scott, E., Xiao, A., Lamanna, W.M., Dahn, J.R., 2013. The Impact of Intentionally Added Water to the Electrolyte of Li-ion Cells. J. Electrochem. Soc. 160, 2281–2287. https://doi.org/10.1149/2.101311jes

Buss, F., 2017. Zur Lösemitteldiffusion in Polymernanoschichten: Schichtdicken- und Konzentrationsabhängigkeit. KIT Scientific Publishing, Place of publication not identified.

Butt, H.-J., Graf, K., Kappl, M., 2003. Physics and chemistry on interfaces, Physics textbook. Wiley-VCH, Weinheim.

Cano, Z.P., Banham, D., Ye, S., Hintennach, A., Lu, J., Fowler, M., Chen, Z., 2018. Batteries and fuel cells for emerging electric vehicle markets. Nat. Energy 3, 279–289. https://doi.org/10.1038/s41560-018-0108-1

Chambre, P., Schaaf, S.A., 1961. Flow of Rarefied Gases. Princeton University Press, New Jersey.

Chen, H., Ericson, T., Temperton, R.H., Källquist, I., Liu, H., Eads, C.N., Mikheenkova, A., Andersson, M., Kokkonen, E., Brant, W.R., Hahlin, M., 2023. Investigating Surface Reactivity of a Ni-Rich Cathode Material toward CO_2, H_2O, and O_2 Using Ambient Pressure X-ray Photoelectron Spectroscopy. ACS Appl. Energy Mater. 6, 11458–11467. https://doi.org/10.1021/acsaem.3c01621

Crank, J., 1975. The Mathematics of Diffusion.

Degen, F., Winter, M., Bendig, D., Tübke, J., 2023. Energy consumption of current and future production of lithium-ion and post lithium-ion battery cells. Nat. Energy. https://doi.org/10.1038/s41560-023-01355-z

Diehm, R., Weinmann, H., Kumberg, J., Schmitt, M., Fleischer, J., Scharfer, P., Schabel, W., 2020. Edge Formation in High-Speed Intermittent Slot-Die Coating of Disruptively Stacked Thick Battery Electrodes.

Energy Technol. 8, 1900137. https://doi.org/10.1002/ente.201900137

Do, D.D. (Ed.), 1998. Adsorption analysis: Equilibria and kinetics, Series on chemical engineering. Imperial College Press, London.

Epstein, N., 1989. On tortuosity and the tortuosity factor in flow and diffusion through porous media. Chem. Eng. Sci. 44, 777–779. https://doi.org/10.1016/0009-2509(89)85053-5

Eser, J., 2021. Über das Stofftransport- und Sorptionsverhalten im Nachtrocknungsprozess von Elektroden für Li-Ionen-Batterien. Karlsruhe.

Eser, J.C., Deichmann, B., Wirsching, T., Merklein, L., Müller, M., Scharfer, P., Schabel, W., 2020a. Diffusion kinetics of water in graphite anodes for Li-ion batteries. Dry. Technol. 40, 1130–1145. https://doi.org/10.1080/07373937.2020.1852568

Eser, J.C., Deichmann, B., Wirsching, T., Weidler, P.G., Scharfer, P., Schabel, W., 2020b. Hysteresis Behavior in the Sorption Equilibrium of Water in Anodes for Li-Ion Batteries. Langmuir ACS J. Surf. Colloids 36, 6193–6201. https://doi.org/10.1021/acs.langmuir.0c00704

Eser, J.C., Wirsching, T., Weidler, P.G., Altvater, A., Börnhorst, T., Kumberg, J., Schöne, G., Müller, M., Scharfer, P., Schabel, W., 2020c. Moisture Adsorption Behavior in Anodes for Li-Ion Batteries. Energy Technol. 8, 1801162. https://doi.org/10.1002/ente.201801162

Fenske, H., Heckmann, T., Michalowski, P., Scharfer, P., Schabel, W., Kwade, A., 2025. Impact of humidity on moisture resorption and resulting electrochemical performance of Gr/NMC622-based Li-ion batteries. J. Energy Storage 119, 116238. https://doi.org/10.1016/j.est.2025.116238

Fenske, H., Lombardo, T., Gerstenberg, J., Kern, C., Steckermeier, D., Michalowski, P., Janek, J., Kwade, A., 2024. Influence of Moisture on the Electrochemical Performance of Prelithiated Graphite/SiO $_x$ Composite Anodes for Li-Ion Batteries. J. Electrochem. Soc. https://doi.org/10.1149/1945-7111/ad3856

Fick, A., 1855. Ueber Diffusion. Wiley. https://doi.org/10.1002/andp.18551700105

Flory, P.J., 1942. Thermodynamics of High Polymer Solutions. J. Chem. Phys. 10, 51–61. https://doi.org/10.1063/1.1723621

Froboese, L., Titscher, P., Westphal, B., Haselrieder, W., Kwade, A., 2017. Mercury intrusion for ion- and conversion-based battery electrodes –

Structure and diffusion coefficient determination. Mater. Charact. 133, 102–111. https://doi.org/10.1016/j.matchar.2017.09.002

Fuller, E.N., Ensley, K., Giddings, J.C., 1969. Diffusion of halogenated hydrocarbons in helium. The effect of structure on collision cross sections. J. Phys. Chem. 73, 3679–3685. https://doi.org/10.1021/j100845a020

Fuller, E.N., Schettler, P.D., Giddings, J.Calvin., 1966. NEW METHOD FOR PREDICTION OF BINARY GAS-PHASE DIFFUSION COEFFICIENTS. Ind. Eng. Chem. 58, 18–27. https://doi.org/10.1021/ie50677a007

Gnielinski, V., Mersmann, A., Thurner, F., 2013. Verdampfung, Kristallisation, Trocknung mit 30 Übungsbeispielen, Softcover reprint of the hardcover 1. ed. 1993, [Nachdr.]. ed. Springer-Fachmedien, Wiesbaden.

Gordon, R., Kassar, M., Willenbacher, N., 2020. Effect of Polymeric Binders on Dispersion of Active Particles in Aqueous LiFePO4-Based Cathode Slurries as well as on Mechanical and Electrical Properties of Corresponding Dry Layers. ACS Omega 5, 11455–11465. https://doi.org/10.1021/acsomega.0c00477

Gracia-Medrano-Bravo, V., Merklein, L., Oberle, N., Batora, M., Scharfer, P., Schabel, W., 2021. Determination of Binary Interaction Parameters for Ternary Polymer–Polymer–Solvent Systems Using Raman Spectroscopy. Adv. Mater. Technol. 6, 2000149. https://doi.org/10.1002/admt.202000149

Günther, T., Billot, N., Schuster, J., Schnell, J., Spingler, F.B., Gasteiger, H.A., 2016. The Manufacturing of Electrodes: Key Process for the Future Success of Lithium-Ion Batteries. Adv. Mater. Res. 1140, 304–311. https://doi.org/10.4028/www.scientific.net/AMR.1140.304

Hagemeister, J., Stock, S., Linke, M., Fischer, M., Drees, R., Kurrat, M., Daub, R., 2023. Lean Cell Finalization in Lithium-Ion Battery Production: Determining the Required Electrolyte Wetting Degree to Begin the Formation. Energy Technol. 11, 2200686. https://doi.org/10.1002/ente.202200686

Hawley, W.B., Li, J., 2019. Electrode manufacturing for lithium-ion batteries—Analysis of current and next generation processing. J. Energy Storage 25, 100862. https://doi.org/10.1016/j.est.2019.100862

Heck, C.A., Huttner, F., Mayer, J.K., Fromm, O., Börner, M., Heckmann, T., Scharfer, P., Schabel, W., Winter, M., Kwade, A., 2023. Production of Nickel-Rich Cathodes for Lithium-Ion Batteries from Lab to Pilot

Scale under Investigation of the Process Atmosphere. Energy Technol. 11, 2200945. https://doi.org/10.1002/ente.202200945

Heckmann, T., Barbig, P., Pham, A.T., Eser, J.C., Scharfer, P., Schabel, W., 2026a. Simulation of the water mass transport in electrodes during post-drying and moisture management of Li-ion battery production via the Two-Scale-Model. Dry. Technol. 12. https://doi.org/10.1080/07373937.2026.2631674

Heckmann, T., Eser, J.C., Altvater, A., Dörr, J., Lepère, H., Scharfer, P., Schabel, W., 2023. Mass Transport in the Stefan-Knudsen Transition Region during Vacuum Drying at Different Pressures in a Porous Structure Resembling Battery Electrodes. Langmuir ACS J. Surf. Colloids. https://doi.org/10.1021/acs.langmuir.2c03450

Heckmann, T., Eser, J.C., Altvater, A., Streller, N., Scharfer, P., Schabel, W., 2022. Experimental Investigation of the Temperature, Pressure, and Binder System Influence on Vacuum Postdrying Processes and Moisture Management of Li-Ion Battery Electrodes. Energy Technol. 2200859. https://doi.org/10.1002/ente.202200859

Heckmann, T., Lechner, M., Barbig, P., Gui, X., Madlindl, L., Scharfer, P., Daub, R., Schabel, W., 2026b. Influence of CO2 in the Li-ion battery-production atmosphere on the sorption kinetics of Li[Ni0.6Co0.2Mn0.2]O2 and its effect on cell performance. J. Energy Storage 153, 120994. https://doi.org/10.1016/j.est.2026.120994

Heckmann, T., Madlindl, L., Scharfer, P., Schabel, W., 2024. Increased Water Uptake of Li[Ni $_{0.6}$ Co $_{0.2}$ Mn $_{0.2}$]O $_2$ for Lithium-Ion Batteries in Humid Nitrogen above a Critical Gas Dew Point. ACS Appl. Energy Mater. 7, 1882–1889. https://doi.org/10.1021/acsaem.3c02976

Heider, U., Oesten, R., Jungnitz, M., 1999. Challenge in manufacturing electrolyte solutions for lithium and lithium ion batteries quality control and minimizing contamination level. J. Power Sources 81–82, 119–122. https://doi.org/10.1016/S0378-7753(99)00142-1

Henry, W., 1803. Experiments on the quantity of gases absorbed by water, at different temperatures, and under different pressures. Philos. Trans. R. Soc. Lond. 93, 29–274. https://doi.org/10.1098/rstl.1803.0004

Huggins, M.L., 1942. Theory of Solutions of High Polymers 1. J. Am. Chem. Soc. 64, 1712–1719. https://doi.org/10.1021/JA01259A068

Huttner, F., Diener, A., Heckmann, T., Eser, J.C., Abali, T., Mayer, J.K., Scharfer, P., Schabel, W., Kwade, A., 2021a. Increased Moisture Uptake of NCM622 Cathodes after Calendering due to Particle

Breakage. J. Electrochem. Soc. 168, 090539. https://doi.org/10.1149/1945-7111/ac24bb

Huttner, F., Haselrieder, W., Kwade, A., 2020. The Influence of Different Post-Drying Procedures on Remaining Water Content and Physical and Electrochemical Properties of Lithium-Ion Batteries. Energy Technol. 8, 1900245. https://doi.org/10.1002/ente.201900245

Huttner, F., Marth, A., Eser, J.C., Heckmann, T., Mohacsi, J., Mayer, J.K., Scharfer, P., Schabel, W., Kwade, A., 2021b. Design of Vacuum Post-Drying Procedures for Electrodes of Lithium-Ion Batteries. Batter. Supercaps 4, 1499–1515. https://doi.org/10.1002/batt.202100088

Imura, S., Takegoshi, E., 1974. Effect of Gas Pressure on Effective Thermal Conductivity of Packed Beds. Trans. Jpn. Soc. Mech. Eng. 40, 489–497. https://doi.org/10.1299/kikai1938.40.489

Jaiser, S., Funk, L., Baunach, M., Scharfer, P., Schabel, W., 2017. Experimental investigation into battery electrode surfaces: The distribution of liquid at the surface and the emptying of pores during drying. J. Colloid Interface Sci. 494, 22–31. https://doi.org/10.1016/j.jcis.2017.01.063

Jaiser, S., Müller, M., Baunach, M., Bauer, W., Scharfer, P., Schabel, W., 2016. Investigation of film solidification and binder migration during drying of Li-Ion battery anodes. J. Power Sources 318, 210–219. https://doi.org/10.1016/j.jpowsour.2016.04.018

Jung, R., Morasch, R., Karayaylali, P., Phillips, K., Maglia, F., Stinner, C., Shao-Horn, Y., Gasteiger, H.A., 2018. Effect of Ambient Storage on the Degradation of Ni-Rich Positive Electrode Materials (NMC811) for Li-Ion Batteries. J. Electrochem. Soc. 165, 132–141. https://doi.org/10.1149/2.0401802jes

Kachel, S., Scharfer, P., Schabel, W., 2013. Sorption isotherms of mixtures of polymers, proteins and electrolytes—Measurement data and model predictions. Chem. Eng. Process. Process Intensif. 68, 45–54. https://doi.org/10.1016/j.cep.2012.09.006

Kaiser, J., Wenzel, V., Nirschl, H., Bitsch, B., Willenbacher, N., Baunach, M., Schmitt, M., Jaiser, S., Scharfer, P., Schabel, W., 2014. Prozess- und Produktentwicklung von Elektroden für Li-Ionen-Zellen. Chem. Ing. Tech. 86, 695–706. https://doi.org/10.1002/cite.201300085

Kalam, S., Abu-Khamsin, S.A., Kamal, M.S., Patil, S., 2021. Surfactant Adsorption Isotherms: A Review. ACS Omega 6, 32342–32348. https://doi.org/10.1021/acsomega.1c04661

Kärger, J., Ruthven, D.M., Theodōru, T.N., 2012. Diffusion in nanoporous materials. Wiley-VCH-Verl., Weinheim.

Kennard, E.H., 1938. Kinetic Theory of Gases. McGrw-Hill Book Company, Inc., New York and London.

Keppeler, M., Roessler, S., Braunwarth, W., 2020. Production Research as Key Factor for Successful Establishment of Battery Production on the Example of Large-Scale Automotive Cells Containing Nickel-Rich LiNi 0.8 Mn 0.1 Co 0.1 O 2 Electrodes. Energy Technol. 8, 2000183. https://doi.org/10.1002/ente.202000183

Kitz, P.G., Novák, P., Berg, E.J., 2020. Influence of Water Contamination on the SEI Formation in Li-Ion Cells: An Operando EQCM-D Study. ACS Appl. Mater. Interfaces 12, 15934–15942. https://doi.org/10.1021/acsami.0c01642

Klemens, J., Wurba, A., Burger, D., Müller, M., Bauer, W., Büchele, S., Leonet, O., Blázquez, J.A., Boyano, I., Ayerbe, E., Ehrenberg, H., Fleischer, J., Smith, A., Scharfer, P., Schabel, W., 2023. Challenges and Opportunities for Large-Scale Electrode Processing for Sodium-Ion and Lithium-Ion Battery. Batter. Supercaps 6, e202300291. https://doi.org/10.1002/batt.202300291

Kosfeld, M., 2024. Feuchtemanagement in der Produktion von Lithium-Ionen Batterien. Braunschweig.

Kosfeld, M., Westphal, B., Kwade, A., 2023. Moisture behavior of lithium-ion battery components along the production process. J. Energy Storage 57, 106174. https://doi.org/10.1016/j.est.2022.106174

Krishna, R., Van Baten, J.M., 2012. Investigating the validity of the Bosanquet formula for estimation of diffusivities in mesopores. Chem. Eng. Sci. 69, 684–688. https://doi.org/10.1016/j.ces.2011.11.026

Kumberg, J., 2022. About Drying of Hierarchically Structured Electrodes for High Energy Li-Ion Battery Applications. Karlsruher Institut für Technologie (KIT).

Kumberg, J., Müller, M., Diehm, R., Spiegel, S., Wachsmann, C., Bauer, W., Scharfer, P., Schabel, W., 2019. Drying of Lithium-Ion Battery Anodes for Use in High-Energy Cells: Influence of Electrode Thickness on Drying Time, Adhesion, and Crack Formation. Energy Technol. 7, 1900722. https://doi.org/10.1002/ente.201900722

Kwade, A., Haselrieder, W., Leithoff, R., Modlinger, A., Dietrich, F., Droeder, K., 2018. Current status and challenges for automotive battery production technologies. Nat. Energy 3, 290–300. https://doi.org/10.1038/s41560-018-0130-3

Landesfeind, J., Hattendorff, J., Ehrl, A., Wall, W.A., Gasteiger, H.A., 2016. Tortuosity Determination of Battery Electrodes and Separators by Impedance Spectroscopy. J. Electrochem. Soc. 163, 1373–1387. https://doi.org/10.1149/2.1141607jes

Langklotz, U., Schneider, M., Michaelis, A., 2013. Water Uptake of Tape-Cast Cathodes for Lithium Ion Batteries. J. Ceram. Sci. Technol. 4, 69–76. https://doi.org/10.4416/JCST2012-00036

Langmuir, I., 1918. The Adsorption of Gases on Plane Surfaces of Glass, Mica and Platinum. J. Am. Chem. Soc. 40, 1361–1403. https://doi.org/10.1021/ja02242a004

Langmuir, I., 1913. The Vapor Pressure of Metallic Tungsten. Phys. Rev. 2, 329–342. https://doi.org/10.1103/PhysRev.2.329

Laurendeau, N.M., 2005. Statistical thermodynamics: fundamentals and applications. Cambridge University Press, New York.

Lechner, M., Kollenda, A., Bendzuck, K., Burmeister, J.K., Mahin, K., Keilhofer, J., Kemmer, L., Blaschke, M.J., Friedl, G., Daub, R., Kwade, A., 2024. Cost modeling for the GWh-scale production of modern lithium-ion battery cells. Commun. Eng. 3, 155. https://doi.org/10.1038/s44172-024-00306-0

Lechner, M., Wölfl, S., Kurz, E., Daub, R., 2025. Identification of critical moisture exposure for nickel-rich cathode active materials in lithium-ion battery production. J. Power Sources 626, 235661. https://doi.org/10.1016/j.jpowsour.2024.235661

Lippke, M., Ohnimus, T., Heckmann, T., Ivanov, D., Scharfer, P., Schabel, W., Schilde, C., Kwade, A., 2022. Simulation of Structure Formation during Drying of Lithium-Ion Battery Electrodes using Discrete Element Method. Energy Technol. 2200724. https://doi.org/10.1002/ente.202200724

Lux, S.F., Lucas, I.T., Pollak, E., Passerini, S., Winter, M., Kostecki, R., 2012. The mechanism of HF formation in LiPF6 based organic carbonate electrolytes. Electrochem. Commun. 14, 47–50. https://doi.org/10.1016/j.elecom.2011.10.026

Mamaliga, I., Schabel, W., Kind, M., 2004. Measurements of sorption isotherms and diffusion coefficients by means of a magnetic suspension balance. Chem. Eng. Process. Process Intensif. 43, 753–763. https://doi.org/10.1016/S0255-2701(03)00077-1

Maxwell, J.C., 1873. A Treatise on Electricity and Magnetism, Vol 1. The Calrendon Press, Oxford.

Mayer, J.K., Almar, L., Asylbekov, E., Haselrieder, W., Kwade, A., Weber, A., Nirschl, H., 2020. Influence of the Carbon Black Dispersing

Process on the Microstructure and Performance of Li-Ion Battery Cathodes. Energy Technol. 8, 1900161. https://doi.org/10.1002/ente.201900161

Merklein, L., Eser, J.C., Börnhorst, T., Könnecke, N., Scharfer, P., Schabel, W., 2021. Different dominating mass transport mechanisms for drying and sorption of toluene-PMMA films – Visualized with Raman spectroscopy. Polymer 222, 123640. https://doi.org/10.1016/j.polymer.2021.123640

NAG Library, 2017.

Neale, G.H., Nader, W.K., 1973. Prediction of transport processes within porous media: Diffusive flow processes within an homogeneous swarm of spherical particles. AIChE J. 19, 112–119. https://doi.org/10.1002/aic.690190116

Oehler, D., Seegert, P., Wetzel, T., 2020. Modeling the Thermal Conductivity of Porous Electrodes of Li-Ion Batteries as a Function of Microstructure Parameters. Energy Technol. 9, 2000574. https://doi.org/10.1002/ente.202000574

Plakhotnyk, A.V., Ernst, L., Schmutzler, R., 2005. Hydrolysis in the system LiPF6—propylene carbonate—dimethyl carbonate—H2O. J. Fluor. Chem. 126, 27–31. https://doi.org/10.1016/j.jfluchem.2004.09.027

Pollard, W.G., Present, R.D., 1948. On Gaseous Self-Diffusion in Long Capillary Tubes. Phys. Rev. 73, 762–774. https://doi.org/10.1103/PhysRev.73.762

Reid, D.S., 2007. Water Activity: Fundamentals and Relationships, in: Barbosa-Cánovas, G.V., Fontana, A.J., Schmidt, S.J., Labuza, T.P. (Eds.), Water Activity in Foods. Wiley, pp. 15–28. https://doi.org/10.1002/9780470376454.ch2

Renfrew, S.E., Kaufman, L.A., McCloskey, B.D., 2019. Altering Surface Contaminants and Defects Influences the First-Cycle Outgassing and Irreversible Transformations of LiNi0.6Mn0.2Co0.2O2. ACS Appl. Mater. Interfaces 11, 34913–34921. https://doi.org/10.1021/acsami.9b09992

Reyes, S.C., Iglesia, E., 1991. Effective diffusivities in catalyst pellets: new model porous structures and transport simulation techniques. J. Catal. 129, 457–472. https://doi.org/10.1016/0021-9517(91)90049-A

Rockland, L.B., 1960. Saturated Salt Solutions for Static Control of Relative Humidity between 5° and 40° C. Anal. Chem. 32, 1375–1376. https://doi.org/10.1021/ac60166a055

Rörig-Dalgaard, I., 2021. Direct Measurements of the Deliquescence Relative Humidity in Salt Mixtures Including the Contribution from Metastable Phases. ACS Omega 6, 16297–16306. https://doi.org/10.1021/acsomega.1c00538

Ruthven, D.M., 1984. Principles of adsorption and adsorption processes, A Wiley-Interscience publication. Wiley, New York.

Saure, Schlünder, R., 1995. Sorption isotherms for methanol, benzene and ethanol on poly(vinyl acetate) (PVAc).

Schabel, W., Ludwig, I., Kind, M., 2004. Measurements of Concentration Profiles in Polymeric Solvent Coatings by Means of an Inverse Confocal Micro Raman Spectrometer—Initial Results. Dry. Technol. 22, 285–294. https://doi.org/10.1081/DRT-120028234

Schabel, W., Mamaliga, I., Kind, M., 2003a. Messungen von Sorptionsisothermen und Diffusionskoeffizienten in Polymerlösungen. Chem. Ing. Tech. 75, 36–41. https://doi.org/10.1002/cite.200390017

Schabel, W., Scharfer, P., Kind, M., Mamaliga, I., 2007. Sorption and diffusion measurements in ternary polymer–solvent–solvent systems by means of a magnetic suspension balance—Experimental methods and correlations with a modified Flory–Huggins and free-volume theory. Chem. Eng. Sci. 62, 2254–2266. https://doi.org/10.1016/j.ces.2006.12.062

Schabel, W., Scharfer, P., Müller, M., Ludwig, I., Kind, M., 2003b. Messung und Simulation von Konzentrationsprofilen bei der Trocknung binärer Polymerlösungen. Chem. Ing. Tech. 75, 1336–1344. https://doi.org/10.1002/cite.200300055

Scharfer, P., 2009. Zum Stofftransport in Brennstoffzellenmembranen: Untersuchungen mit Hilfe der konfokalen Mikro-Raman-Spektroskopie. KIT Scientific Publ, Karlsruhe.

Scharfer, P., Schabel, W., Kind, M., 2008. Modelling of alcohol and water diffusion in fuel cell membranes—Experimental validation by means of in situ Raman spectroscopy. Chem. Eng. Sci. 63, 4676–4684. https://doi.org/10.1016/j.ces.2008.03.014

Schiesser, W.E., Griffiths, G.W., 2009. A Compendium of Partial Differential Equation Models. Cambridge University Press.

Schlünder, E.-U., 1996. Einführung in die Stoffübertragung, [2. Aufl.]. ed, Lehrbuch Chemie + Technik. Vieweg, Braunschweig.

Schmitt, M., Baunach, M., Wengeler, L., Peters, K., Junges, P., Scharfer, P., Schabel, W., 2013. Slot-die processing of lithium-ion battery electrodes—Coating window characterization. Chem. Eng. Process.

Process Intensif. 68, 32–37. https://doi.org/10.1016/j.cep.2012.10.011

Scholl, S., Kajszika, H., Mersmann, A., 1993. Adsorption and desorption kinetics in activated carbon. Gas Sep. Purif. 7, 207–212. https://doi.org/10.1016/0950-4214(93)80019-S

Schuer, A.R., Kuenzel, M., Yang, S., Kosfeld, M., Mueller, F., Passerini, S., Bresser, D., 2022. Diagnosis tools for humidity-born surface contaminants on Li[Ni0.8Mn0.1Co0.1]O2 cathode materials for lithium batteries. J. Power Sources 525, 231111. https://doi.org/10.1016/j.jpowsour.2022.231111

Schünemann, J.-H., Dreger, H., Bockholt, H., Kwade, A., 2016. Smart Electrode Processing for Battery Cost Reduction. ECS Trans. 73, 153–159. https://doi.org/10.1149/07301.0153ecst

Scott, D.S., Dullien, F.A.L., 1962. Diffusion of ideal gases in capillaries and porous solids. AIChE J. 8, 113–117. https://doi.org/10.1002/aic.690080126

Scott, W.J., 1957. Water Relations of Food Spoilage Microorganisms, in: Advances in Food Research. Elsevier, pp. 83–127. https://doi.org/10.1016/S0065-2628(08)60247-5

Shkrob, I.A., Gilbert, J.A., Phillips, P.J., Klie, R., Haasch, R.T., Bareño, J., Abraham, D.P., 2017. Chemical Weathering of Layered Ni-Rich Oxide Electrode Materials: Evidence for Cation Exchange. J. Electrochem. Soc. 164, 1489–1498. https://doi.org/10.1149/2.0861707jes

Sicklinger, J., Metzger, M., Beyer, H., Pritzl, D., Gasteiger, H.A., 2019. Ambient Storage Derived Surface Contamination of NCM811 and NCM111: Performance Implications and Mitigation Strategies. J. Electrochem. Soc. 166, 2322–2335. https://doi.org/10.1149/2.0011912jes

Siebel, D., Schabel, W., Scharfer, P., 2017. Diffusion in quaternary polymer solutions—Model development and validation. Prog. Org. Coat. 110, 187–194. https://doi.org/10.1016/j.porgcoat.2017.05.002

Sing, K.S.W., 1982. Reporting physisorption data for gas/solid systems with special reference to the determination of surface area and porosity (Provisional). Pure Appl. Chem. 54, 2201–2218. https://doi.org/10.1351/pac198254112201

Spiegel, S., Hoffmann, A., Klemens, J., Scharfer, P., Schabel, W., 2022. Optimization of Edge Quality in the Slot-Die Coating Process of High-Capacity Lithium-Ion Battery Electrodes. Energy Technol. 2200684. https://doi.org/10.1002/ente.202200684

Stephan, P., Kabelac, S., Kind, M., Mewes, D., Schaber, K., Wetzel, T. (Eds.), 2019. VDI-Wärmeatlas, Springer Reference Technik. Springer Berlin Heidelberg, Berlin, Heidelberg. https://doi.org/10.1007/978-3-662-52989-8

Stephan, P., Schaber, K., Stephan, K., Mayinger, F., 2013. Thermodynamik: Grundlagen und technische Anwendungen Band 1: Einstoffsysteme, 19., ergänzte Aufl. 2013. ed, Springer-Lehrbuch. Springer Berlin Heidelberg, Berlin, Heidelberg; s.l. https://doi.org/10.1007/978-3-642-30098-1

Stephan, P., Schaber, K., Stephan, K., Mayinger, F., 2010. Thermodynamik - Grundlagen und technische Anwendungen: Band 2: Mehrstoffsysteme und chemische Reaktionen, Springer-Lehrbuch. Springer Berlin Heidelberg.

Stich, M., Pandey, N., Bund, A., 2017. Drying and moisture resorption behaviour of various electrode materials and separators for lithium-ion batteries. J. Power Sources 364, 84–91. https://doi.org/10.1016/j.jpowsour.2017.08.009

Terborg, L., Nowak, S., Passerini, S., Winter, M., Karst, U., Haddad, P.R., Nesterenko, P.N., 2012. Ion chromatographic determination of hydrolysis products of hexafluorophosphate salts in aqueous solution. Anal. Chim. Acta 714, 121–126. https://doi.org/10.1016/j.aca.2011.11.056

Thakker, M.T., Chi, C.Whan., Peck, R.E., Wasan, D.T., 1968. Vapor pressure measurements of hygroscopic salts. J. Chem. Eng. Data 13, 553–558. https://doi.org/10.1021/je60039a032

Thurner, F., Stietz, M., 1984. Bestimmung der sorptionsisothermen lösungsmittelfeuchter sorbentien nach der durchströmungsmethode. Chem. Eng. Process. Process Intensif. 18, 333–340. https://doi.org/10.1016/0255-2701(84)87010-5

Tsien, H.-S., 1946. Superaerodynamics, Mechanics of Rarefied Gases. J. Aeronaut. Sci. 13, 653–664. https://doi.org/10.2514/8.11476

Tsotsas, E., Martin, H., 1987. Thermal conductivity of packed beds: A review. Chem. Eng. Process. Process Intensif. 22, 19–37. https://doi.org/10.1016/0255-2701(87)80025-9

Ventura Silva, G., Thomitzek, M., Lippke, M., Heckmann, T., Karaki, H., Lischka, C., Möhlen, F., Mayer, D., Hagemeister, J., Daub, R., Fleischer, J., Nirschl, H., Schröder, D., Scharfer, P., Schabel, W., Kwade, A., Herrmann, C., 2022. Digitalization Platform for Sustainable Battery Cell Production: Coupling of Process, Production, and Product Models. Energy Technol. 2200801. https://doi.org/10.1002/ente.202200801

Vetter, J., Novák, P., Wagner, M.R., Veit, C., Möller, K.-C., Besenhard, J.O., Winter, M., Wohlfahrt-Mehrens, M., Vogler, C., Hammouche, A., 2005. Ageing mechanisms in lithium-ion batteries. J. Power Sources 147, 269–281. https://doi.org/10.1016/j.jpowsour.2005.01.006

Vrentas, J.S., Vrentas, C.M., 1996. Hysteresis Effects for Sorption in Glassy Polymers. Macromolecules 29, 4391–4396. https://doi.org/10.1021/ma950969l

Vrentas, J.S., Vrentas, C.M., 1991. Sorption in glassy polymers. Macromolecules 24, 2404–2412. https://doi.org/10.1021/ma00009a043

Vu, H.T., Tsotsas, E., 2018. Mass and Heat Transport Models for Analysis of the Drying Process in Porous Media: A Review and Numerical Implementation. Int. J. Chem. Eng. 2018, 1–13. https://doi.org/10.1155/2018/9456418

Whitaker, S., 1999. The Method of Volume Averaging. Springer Netherlands, Dordrecht.

Williams, D.D., Miller, R.R., 1970. Effect of Water Vapor on the LiOH-CO2 Reaction. Dynamic Isothermal System. Ind. Eng. Chem. Fundam. 9, 454–457. https://doi.org/10.1021/i160035a024

Wood, M., Li, J., Ruther, R.E., Du, Z., Self, E.C., Meyer, H.M., Daniel, C., Belharouak, I., Wood, D.L., 2020. Chemical stability and long-term cell performance of low-cobalt, Ni-Rich cathodes prepared by aqueous processing for high-energy Li-Ion batteries. Energy Storage Mater. 24, 188–197. https://doi.org/10.1016/j.ensm.2019.08.020

Xiong, D.J., Petibon, R., Madec, L., Hall, D.S., Dahn, J.R., 2016. Some Effects of Intentionally Added Water on LiCoO $_2$ /Graphite Pouch Cells. J. Electrochem. Soc. 163, A1678–A1685. https://doi.org/10.1149/2.0901608jes

Yang, D., Li, X., Wu, N., Tian, W., 2016. Effect of moisture content on the electrochemical performance of LiNi 1/3 Co 1/3 Mn 1/3 O 2 /graphite battery. Electrochimica Acta 188, 611–618. https://doi.org/10.1016/j.electacta.2015.12.063

Yue, M., Azam, S., Zhang, N., Dahn, J.R., Yang, C., 2024. Residual NMP and Its Impacts on Performance of Lithium-Ion Cells. J. Electrochem. Soc. 171, 050515. https://doi.org/10.1149/1945-7111/ad4396

Zehner, P., Schlünder, E.U., 1973. Die effektive Wärmeleitfähigkeit durchströmter Kugelschüttungen bei mäßigen und hohen

Temperaturen. Chem. Ing. Tech. 45, 272–276. https://doi.org/10.1002/cite.330450509

Zehner, P., Schlünder, E.U., 1970. Wärmeleitfähigkeit von Schüttungen bei mäßigen Temperaturen. Chem. Ing. Tech. 42, 933–941. https://doi.org/10.1002/cite.330421408

Zhao, F., Han, F., Zhang, S., Tian, H., Yang, Y., Sun, K., 2018. Vacuum drying kinetics and energy consumption analysis of LiFePO4 battery powder. Energy 162, 669–681. https://doi.org/10.1016/j.energy.2018.08.023

Zou, L., He, Y., Liu, Z., Jia, H., Zhu, J., Zheng, J., Wang, G., Li, X., Xiao, J., Liu, J., Zhang, J.-G., Chen, G., Wang, C., 2020. Unlocking the passivation nature of the cathode–air interfacial reactions in lithium ion batteries. Nat. Commun. 11, 3204. https://doi.org/10.1038/s41467-020-17050-6

List of Figures

List of Tables

8 Appendix

8.1 Porosimetry data spherical graphite and PVDF anode

Figure 8.1 displays the porosimetry data of the PVDF anode and its active material.

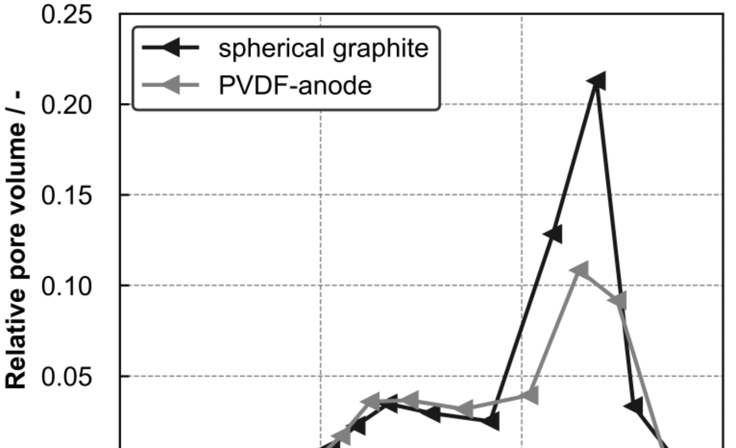

Figure 8.1: Porosimetry data of the PVDF anode and its active material, the spherical graphite. The graphs show that the pores of around 200 nm exist in both structures. The largest relative pore volume in both structures are pores between 2 and 3 µm.

8.2 Material and Methods

The following Figures show the repeatability of the vacuum drying experiments:

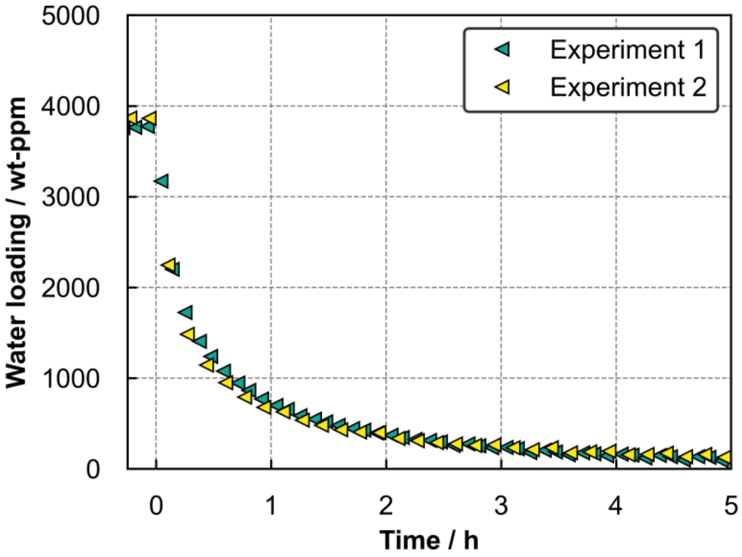

Figure 8.2: Three experiments made with the compressed stack of CMC/SBR-electrodes. The experiments were performed on different days with different samples. The pressure was 200 mbar at 80 °C. The data of all experiments are sufficiently alike to consider the method as repeatable.

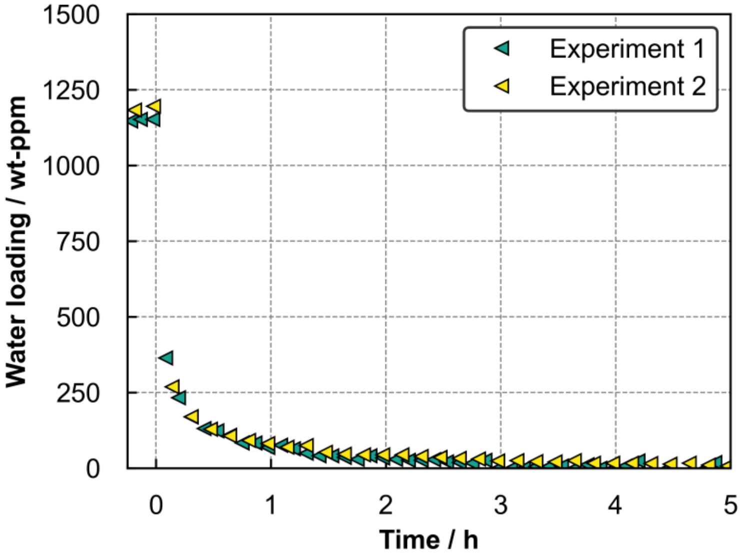

Figure 8.3: Three experiments made with the compressed stack of PVDF-electrodes. The experiments were performed on different days with different samples. The pressure was 200 mbar at 80 °C. The data of all experiments are sufficiently alike to consider the method as repeatable.

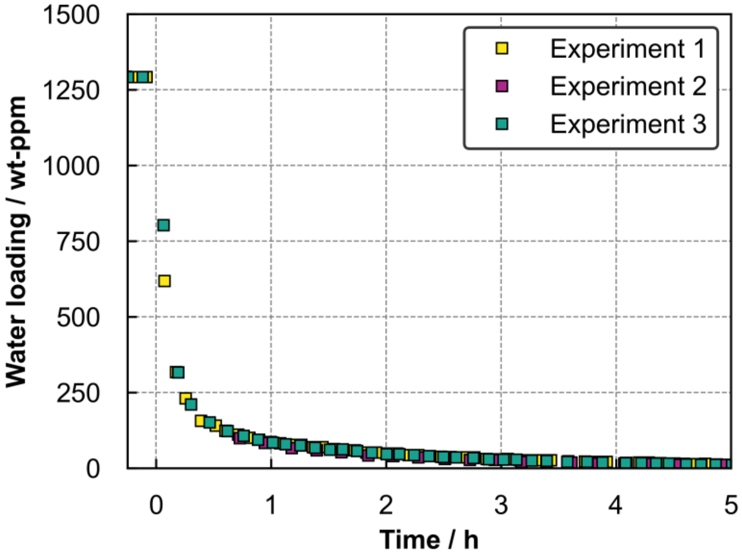

Figure 8.4: Three experiments made with the backfill of graphite. The experiments were performed on different days with different samples. The pressure was 40 mbar at 30 °C. The data of all experiments are sufficiently alike to consider the method as repeatable.

8.3 Geometrical tortuosity versus tortuosity factor

The geometric tortuosity is the net length of a curved path L_{curve} compared to its length if the curve was a straight path $L_{straight}$. In case of pores, the net length of a pore L is compared to a straight capillary:

$$\tau_{geometric} = \frac{L_{straight}}{L_{curve}} = \frac{L_{capillary}}{L} \qquad (35)$$

Most tortuosity-correlations provide a value for the tortuosity factor rather than the geometric tortuosity. This distinction is often neglected, as the tortuosity is a fit parameter and not mathematically derived. The difference between the tortuosity factor and the geometric tortuosity can be shown by deriving Fick's first law for porous media starting from the diffusion through a straight capillary. The flux through a capillary is:

$$\dot{n}_{i,capillary} = -D_{i,j} \cdot \frac{dc_i}{ds_{capillary}} \tag{36}$$

Exchanging $ds_{capillary}$ according to the definition of the geometric tortuosity ($ds_{capillary} = ds \cdot \tau_{geometric}$), which is the elongation of the diffusion distance trough the capillary $ds_{capillary}$ compared to the diffusion distance in porous media ds. Therefore, transforming the coordinate from the capillary to the porous media yields:

$$\dot{n}_{i,capillary} = -\frac{1}{\tau_{geometric}} \cdot D_{i,j} \cdot \frac{dc_i}{ds} \tag{37}$$

Comparing residence times of molecules in a capillary and in the pores of the porous media gives an expression for the interstitial flux through the pores of the porous media:

$$t_{pore} = \frac{L \cdot c_{i,mean}}{\dot{n}_{i,pores}} \tag{38}$$

And

$$t_{capillary} = \frac{L_{capillary} \cdot c_{i,mean}}{\dot{n}_{i,capillary}} \tag{39}$$

The mean concentration $c_{i,mean}$ of pore and capillary is equal. If the residence time in the pore t_{pore} and in the capillary $t_{capillary}$ is equal, $L_{capillary}$ must be larger than the length of the porous media L (not the pore's length) by the factor $\tau_{geometric}$:

$$\dot{n}_{i,pores} = \dot{n}_{i,capillary} \frac{L}{L_{capillary}} = \dot{n}_{i,capillary} \cdot \frac{1}{\tau_{geometric}} \tag{40}$$

The flux through pores of the porous media is smaller than the flux of a capillary by the factor $\tau_{geometric}$, to maintain the same residence time in the porous media as in the capillary. Therefore, the flux through the pores of the porous media is:

$$\dot{n}_{i,pores} = -\frac{1}{\tau_{geometric}^2} \cdot D_{i,j} \cdot \frac{dc_i}{ds} \tag{41}$$

Equation 41 shows the interstitial flux of the component i through the porous media in transport direction s. This flux through the porous media multiplied by the porosity ε is equal to the superficial flux of this media ($\dot{n}_{i,media} = \varepsilon \cdot \dot{n}_{i,pores}$), which results in:

$$\dot{n}_{i,media} = -\frac{\varepsilon}{\tau_{geometric}^2} \cdot D_{i,j} \cdot \frac{dc_i}{ds} \tag{42}$$

The flux in porous media can also be written as a function of $D_{eff,i,j}$:

$$\dot{n}_{i,media} = -D_{eff,i,j} \cdot \frac{d\tilde{c}_i}{ds} \tag{43}$$

Comparing equation 42 and 43 allows the comparison of $D_{i,j}$ and $D_{eff,i,j}$:

$$D_{eff,i,j} = \frac{\varepsilon}{\tau_{geometric}^2} \cdot D_{i,j} = \frac{\varepsilon}{\tau_{factor}} \cdot D_{i,j} \tag{44}$$

Thus, the effective diffusion coefficient in porous media is a function of the geometric tortuosity squared. If derived for the diffusion through a straight capillary, the square dependency originates from the coordinate transformation and the flux decrease of the diffusion through porous media compared to the diffusion through a straight capillary.

8.4 Diffusion regimes: Knudsen diffusion coefficient

The mass transport of a gas molecule in a discontinuous gas phase can be derived from the kinetic gas theory. In this theory, gas molecules are considered as spheres with masses that randomly move through time and space. It is assumed that molecules do not interact with each other, and their energy is purely kinetic. The Maxwell-Boltzmann velocity distribution gives the speed and orientation of the gas-molecule movement. The normalized velocity distribution in x-direction, derived from the momentum equation is (Laurendeau, 2005):

$$f(v_x)dx = \left(\frac{m}{2 \cdot \pi \cdot k \cdot T}\right)^{\frac{1}{2}} \cdot \exp\left(-\frac{m}{2 \cdot k \cdot T} \cdot v_x^2\right) dx \tag{45}$$

This velocity distribution can be used to derive the diffusion coefficient of molecules in a discontinuous gas phase.

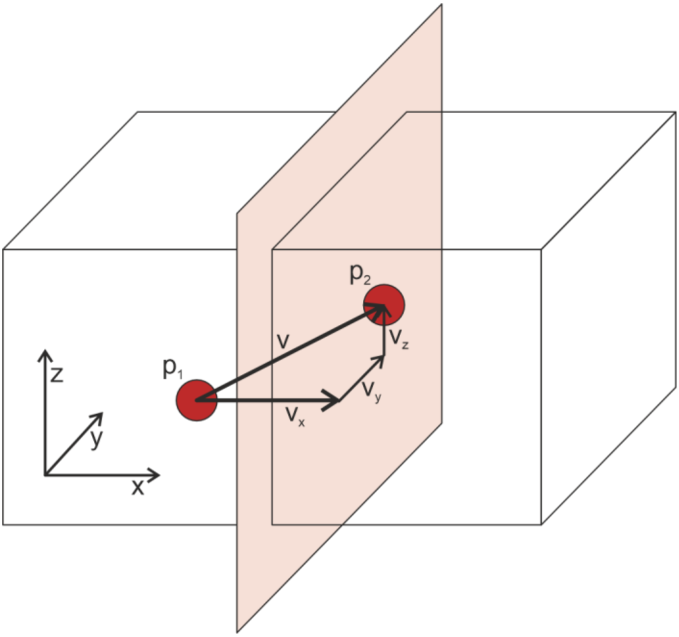

Figure 8.5: The velocity v of a molecule (red circle) that moves from position one (p_1) to position two (p_2) can be divided into the velocities of the cartesian coordinates (v_x, v_y, v_z). The molecule travels or diffuses in x-direction with the velocity v_x. The Maxwell-Boltzmann Speed distribution can be used for a general calculation of the mean velocity of molecules in any direction.

All molecules that strike a plane orthogonal for example to the x-axis in space can be considered diffused from one side of this plane to the other in x-direction. Therefore, the mean velocity in the positive x-direction is the diffusion coefficient in x-direction. This consideration is valid for all space coordinates. The mean velocity in positive x-direction is:

$$\overline{v}_x = \int_0^{\infty} v_x \cdot f(v_x) dx \tag{46}$$

Combining equations 45 and 46 yields:

$$\overline{v}_x = \left(\frac{m}{2 \cdot \pi \cdot k \cdot T}\right)^{\frac{1}{2}} \cdot \int_0^{\infty} v_x \cdot \exp\left(-\frac{m}{2 \cdot k \cdot T} \cdot v_x^2\right) dx \tag{47}$$

This is a Gaussian integral in the form of $\int_0^{\infty} x \cdot e^{-a \cdot x^2} dx = (2 \cdot a\,)^{-1}$, which integrates to:

$$\overline{v}_x = \left(\frac{m \cdot k^2 \cdot T^2}{2 \cdot \pi \cdot k \cdot T \cdot m^2}\right)^{\frac{1}{2}} = \sqrt{\frac{k \cdot T}{2 \cdot \pi \cdot m}} \tag{48}$$

This is the equation for the mean molecule velocity in x-direction. The mean velocity $\overline{v}_x$ of gas molecules can be divided by the mean velocities of gas molecule $\overline{v}$ at a given temperature:

$$\overline{v} = \sqrt{\frac{8 \cdot k \cdot T}{\pi \cdot m}} \tag{49}$$

This division yields the following known equation for the mass-transport coefficient of gas molecules (i) in the direction x depending on the mean velocity of the gas molecules (equations 48 and 49):

$$\frac{\overline{v}_x}{\overline{v}} = \frac{\sqrt{\frac{k \cdot T}{2 \cdot \pi \cdot m}}}{\sqrt{\frac{8 \cdot k \cdot T}{\pi \cdot m}}} = \frac{1}{4} \tag{50}$$

This is the mass-transport coefficient ($\beta_i = \overline{v}_x$) for a gas phase without obstacles. However, if there are diffusion boundaries such as in a porous structure, they must be incorporated to obtain an applicable transport quantity. This diffusion coefficient in the discontinuum can be derived via force balance in a pore.

8.5 Derivation of the equation used in chapter 4 and 5

The following tables list the derivation of the equations for the adsorption and absorption simulation, compare section 3.3.1 and 3.3.2. The basis of the equation is Fick's second law of diffusion according to Crank (Crank, 1975). The indexes will be introduced upon first usage. The following table shows, the derivation as well as boundary and initial conditions of the equation in section 3.3.1 for the component i. The comment column discloses the step to the equation in the subsequent row.

Equation	#	Units	Comment
$\frac{\partial c_i}{\partial t} = \frac{\partial}{\partial z} D_{i,j} \frac{\partial c_i}{\partial z}$	(51)	$\frac{mol_i}{m^3 \cdot s} = \frac{1}{m} \cdot \frac{m^2}{s} \cdot \frac{mol_i}{m^3 \cdot m}$	Split into gas and solid phase.
$\overbrace{\varepsilon \frac{\partial c_i}{\partial t}}^{gas} + \overbrace{(1-\varepsilon) \frac{\partial c_i}{\partial t}}^{solid} = \overbrace{\varepsilon \frac{\partial}{\partial z} D_{i,g} \frac{\partial c_i}{\partial z}}^{gas} + \overbrace{(1-\varepsilon) \frac{\partial}{\partial z} D_{i,s} \frac{\partial c_i}{\partial z}}^{solid}$	(52)	$\frac{m^3_{g(gas)}}{m^3} \cdot \frac{mol_i}{m^3_g} \cdot \frac{1}{s} + \frac{m^3_{s(solid)}}{m^3} \cdot \frac{mol_i}{m^3_s} \cdot \frac{1}{s} = \frac{1}{m} \cdot \frac{m^2}{s} \cdot \frac{mol_i}{m^3\,m} + \frac{1}{m} \cdot \frac{m^2}{s} \cdot \frac{mol_i}{m^3\,m}$	Neglecting surface diffusion. Transformation to other concentration quantities.

$\varepsilon\frac{\partial\tilde{\rho}_g\tilde{y}_i}{\partial t}+(1-\varepsilon)\frac{\partial\tilde{\rho}_s\tilde{X}_i}{\partial t}=$ $\varepsilon\frac{\partial}{\partial z}D_{i,g}\frac{\partial\tilde{\rho}_g\tilde{y}_i}{\partial z}$	(53)	$\frac{m_g^3}{m^3}\cdot\frac{mol_g}{m_g^3}\cdot\frac{mol_i}{mol_g}\cdot\frac{1}{s}+\frac{m_s^3}{m^3}\cdot\frac{mol_s}{m_s^3}\cdot\frac{mol_i}{mol_s}\cdot$ $\frac{1}{s}=\frac{1}{m}\cdot\frac{m^2}{s}\cdot\frac{mol_g}{m^3}\cdot\frac{mol_i}{mol_g}\cdot\frac{1}{m}$	Density of gas and solids do not change with space and time.
$\varepsilon\tilde{\rho}_g\frac{\partial\tilde{y}_i}{\partial t}+(1-\varepsilon)\tilde{\rho}_s\frac{\partial\tilde{X}_i}{\partial t}=\varepsilon D_{i,g}\tilde{\rho}_g\frac{\partial^2\tilde{y}_i}{\partial z^2}$	(54)	" – "	Transforming molar loading of the solid phase into gravimetric loading.
$\varepsilon\tilde{\rho}_g\frac{\partial\tilde{y}_i}{\partial t}+(1-\varepsilon)\tilde{\rho}_s\frac{\widetilde{M}_S}{\widetilde{M}_i}\frac{\partial X_i}{\partial t}=$ $\varepsilon D_{i,g}\tilde{\rho}_g\frac{\partial^2\tilde{y}_i}{\partial z^2}$	(55)	" – " $+\frac{m_s^3}{m^3}\cdot\frac{mol_s}{m_s^3}\cdot\frac{\frac{kg_s}{mol_s}}{\frac{kg_i}{mol_i}}\cdot\frac{kg_i}{kg_s}\cdot\frac{1}{s}=$ " – "	Transforming concentration quantities via either **Option 1** or **Option 2**.
Option 1: constant sorption parameter $\widetilde{M}_i\tilde{y}_i=KX_i\Leftrightarrow\tilde{y}_i=\frac{K}{\widetilde{M}_i}X_i$	(56)	$\frac{kg_i}{mol_i}\cdot\frac{mol_i}{mol_g}=\frac{kg_s}{mol_g}\cdot\frac{kg_i}{kg_s}$	Inserting Dividing by $\widetilde{M}_i$

$\varepsilon\tilde{\rho}_g K \frac{\partial X_i}{\partial t} + (1-\varepsilon)\,\underbrace{\tilde{\rho}_s \widetilde{M}_s}_{\rho_s} \frac{\partial X_i}{\partial t} =$ $\varepsilon D_{i,g}\tilde{\rho}_g K \frac{\partial^2 X_i}{\partial z^2}$	(57)	$\frac{m_g^3}{m^3} \cdot \frac{mol_g}{m_g^3} \cdot \frac{kg_s}{mol_g} \cdot \frac{kg_i}{kg_s} \cdot \frac{1}{s} + \frac{m_s^3}{m^3} \cdot \frac{kg_s}{m_s^3} \cdot$ $\frac{kg_i}{kg_s} \cdot \frac{1}{s} = \frac{m_g^3}{m^3} \cdot \frac{m^2}{s} \cdot \frac{mol_g}{m_g^3} \cdot \frac{kg_s}{mol_g} \cdot \frac{kg_i}{kg_s} \cdot \frac{1}{m^2}$	Final equation, Option 1
Option 2: Multiplying $\frac{\partial \tilde{y}_i}{\partial t}$ with $\frac{\partial X_i}{\partial X_i} \cdot \frac{\partial a_i}{\partial a_i}$ and differentiation for non-linear sorption equilibrium. $\frac{\partial \tilde{y}_i}{\partial t} = \frac{\partial \tilde{y}_i}{\partial a_i}\frac{\partial a_i}{\partial X_i}\frac{\partial X_i}{\partial t}$	(58)	$\frac{mol_i}{s} = \frac{mol_i}{-} \cdot \frac{-}{kg_s} \cdot \frac{kg_s}{s}$	Application of Rault's and Dalton's law. $\frac{\partial a_i}{\partial X_i}$ is approximated via the sorption equilibrium.
$\varepsilon \widetilde{M}_i \tilde{\rho}_g \frac{p_i^0(T)}{p}\frac{\partial a_i}{\partial X_i}\frac{\partial X_i}{\partial t} +$ $(1-\varepsilon)\rho_s \frac{\partial X_i}{\partial t} =$ $\varepsilon \widetilde{M}_i D_{i,g}\tilde{\rho}_g \frac{p_i^0(T)}{p}\frac{\partial a_i}{\partial X_i}\frac{\partial^2 X_i}{\partial z^2}$	(59)	$\frac{m_g^3}{m^3} \cdot \frac{kg_i}{mol_i} \cdot \frac{mol_g}{m_g^3} \cdot \frac{Pa_i}{Pa_g} \cdot \frac{kg_s}{kg_i} \cdot \frac{kg_i}{kg_s} \cdot \frac{1}{s} +$ $\frac{m_s^3}{m^3} \cdot \frac{kg_s}{m_s^3} \cdot \frac{kg_i}{kg_s} \cdot \frac{1}{s} =$ $\frac{m_g^3}{m^3} \cdot \frac{kg_i}{mol_i} \cdot \frac{m^2}{s} \cdot \frac{mol_g}{m_g^3} \cdot \frac{Pa_i}{Pa_g} \cdot \frac{kg_s}{kg_i} \cdot \frac{kg_i}{kg_s}\frac{1}{m^2}$	Final equation, Option 2

Initial condition:

$$X_i(t = 0) = X_{IV\ (initial\ value)}$$

(60) $\frac{kg_i}{kg_s} = \frac{kg_i}{kg_s}$

Boundary condition Dirichlet:

$$X_i\big|_{z=z_{max}} = X_{BC(boundary\ condition)}$$

(61) $\frac{kg_i}{kg_s} = \frac{kg_i}{kg_s}$

Boundary condition with a fixed value.

Boundary condition Neumann:

$$\frac{\partial X_i}{\partial z}\bigg|_{z=z_0} = 0$$

(62)

Zero gradient condition for example at diffusion barrier.

Boundary condition Robin: $\varepsilon D_{i,g}\tilde{\rho}_g K \frac{\partial X_i}{\partial z} = -\frac{D_{i,g}}{s}\tilde{\rho}_g \widetilde{M}_i (y_i\vert_{z=z_{max}} - y_{i,\infty})$	(63)	$\frac{m_g^3}{m^3}\cdot\frac{m^2}{s}\cdot\frac{mol_g}{m_g^3}\cdot\frac{kg_s}{mol_g}\cdot\frac{kg_i}{kg_s}\cdot\frac{1}{m} = \frac{m^2}{s}\cdot\frac{1}{m}\cdot\frac{molg}{m^3}\,\frac{kg_i}{mol_i}\,\frac{mol_i}{mol_g}$	Flux at a phase boundary defined by Fick's 1st law of diffusion.

The equations in the following table incorporate the micro scale into the partial differential equations from the previous table. Initial and boundary conditions are the same as the ones listed in the previous table. The units are like the units in the previous table. Therefore, only the final units on each side of the equal sign will be displayed. For the sake of shorter equations, the concentration quantities will be transformed via **Option 1** from (56). A transformation with **Option 2** from 58 is equally possible.

Equation	#	Unit	Comment
$\frac{\partial c_i}{\partial t} = \frac{\partial}{\partial z} D_{i,j}\frac{\partial c_i}{\partial z}$	(64)	$\frac{mol_i}{m^3\cdot s}$	Split into gas and solid phase.

$\underbrace{\overbrace{\varepsilon\frac{\partial c_{i,g}}{\partial t}}^{gas}+\overbrace{(1-\varepsilon)\frac{\partial c_{i,s}}{\partial t}}^{solid}=\overbrace{\varepsilon\frac{\partial}{\partial z}D_{i,g}\frac{\partial c_{i,g}}{\partial z}}^{gas}+\overbrace{(1-\varepsilon)\frac{\partial}{\partial z}D_{i,s}\frac{\partial c_{i,s}}{\partial z}}^{solid}}_{macro\ scale}$	(65)	$\frac{mol_i}{m^3\cdot s}$	Neglecting surface diffusion. Introducing micro scale
$\underbrace{\Phi\left(\varepsilon\frac{\partial c_{i,g}}{\partial t}+(1-\varepsilon)\frac{\partial c_{i,s}}{\partial t}\right)}_{macro\ scale}+\underbrace{(1-\Phi)\frac{\partial c_{i,Mi(Micro)}}{\partial t}}_{micro\ scale}=\underbrace{\Phi\,\varepsilon\frac{\partial}{\partial z}D_{i,g}\frac{\partial c_{i,g}}{\partial z}}_{macro\ scale}$ With $\Phi=\frac{V_{Ma}}{V_{Gesamt}}$	(66)	$\frac{mol_i}{m^3\cdot s}$	Transforming concentration quantities
$\Phi\left(\varepsilon\widetilde{M}_i\tilde{\rho}_g\frac{\partial\tilde{y}_{i,g}}{\partial t}+(1-\varepsilon)\rho_s\frac{\partial X_{i,s}}{\partial t}\right)+(1-\Phi)\rho_{Mi}\frac{\partial X_{i,Mi}}{\partial t}=$ $\Phi\,\varepsilon\widetilde{M}_i\frac{\partial}{\partial z}D_{i,g}\tilde{\rho}_g\frac{\partial\tilde{y}_{i,G}}{\partial z}$	(67)	$\frac{kg_i}{m^3\cdot s}$	Transforming $\tilde{y}_{i,g}$ to $X_{i,s}$ via **Option 1** from (56).
$\tilde{y}_{i,G}=\frac{K}{\widetilde{M}_i}X_{i,s}$	(68)	$\frac{kg_i}{mol_g}$	Inserting
$\Phi\left(\varepsilon\tilde{\rho}_g K\frac{\partial X_{i,s}}{\partial t}+(1-\varepsilon)\rho_s\frac{\partial X_{i,s}}{\partial t}\right)+(1-\Phi)\rho_{Mi}\frac{\partial X_{i,Mi}}{\partial t}=$ $\Phi\,\varepsilon\frac{\partial}{\partial z}D_{i,g}\tilde{\rho}_g K\frac{\partial X_{i,s}}{\partial z}$	(69)	$\frac{kg_i}{m^3\cdot s}$	Final equation.

This final equation can be implemented into a PDE-solver. The equation contains two variables that depend on z and t. Depending on the diffusion times on micro and macro scale this equation can either be solved as:

i. Partial differential equation of $X_{i,s}$ ($\tau_{Micro} \ll \tau_{Macro}$),
ii. Coupled PDE's via the time of $X_{i,s}$ and $X_{i,Mi}$ ($\tau_{Micro} \sim \tau_{Macro}$), or
iii. Partial differential equation of $X_{i,Mi}$ ($\tau_{Macro} \ll \tau_{Micro}$).

The cases i. and iii. are the boundary cases discussed in chapter 4.2. These cases define the diffusion times τ_{Micro} and τ_{Macro}. Case ii. is the Two-Scale-Model discussed in chapter 4. The following table shows these three cases.

Equation	#	Unit	Comment
Case i. for $\tau_{Micro} \ll \tau_{Macro}$: Mass transport on micro scale is fast, $X_{i,Mi} \neq f(x)$ $X_{i,Mi} = K_{MiMa} X_{i,s}$	(70)	$\frac{kg\ i}{kg\ Mi} = \frac{kg\ s}{kg\ Mi}\frac{kg\ i}{kg\ s}$	Transforming $X_{i,Mi}$ to $X_{i,s}$ via **Option 1** from (56).
$\Phi\left(\varepsilon\tilde{\rho}_G K \frac{\partial X_{i,s}}{\partial t} + (1-\varepsilon)\rho_s \frac{\partial X_{i,s}}{\partial t}\right) + (1-\Phi) K_{MiMa}\rho_{Mi}\frac{\partial X_{i,s}}{\partial t} =$ $\Phi\ \varepsilon \frac{\partial}{\partial z} D_{i,g}\tilde{\rho}_G K \frac{\partial X_{i,s}}{\partial z}$	(71)	$\frac{kg_i}{m^3 \cdot s}$	Deriving τ_{Macro}

$\tau_{Macro} = \frac{s_{Ma}^2}{D_{Ma}} = \frac{s_{Ma}^2}{\frac{\Phi\varepsilon D_{i,g}\tilde{\rho}_G K}{\Phi(\varepsilon\tilde{\rho}_G K+(1-\varepsilon)\rho_s)+(1-\Phi)K_{MiMa}\rho_{Mi}}}$	(72)	s	
Case ii. for $\tau_{Micro} \sim \tau_{Macro}$: Implementing the PDE's on micro scale in between every two macro-scale mesh points. $\frac{\partial X_{i,Mi}(z)}{\partial t} = \frac{\partial}{\partial x} D_{i,Mi} \frac{\partial X_{i,Mi}(z)}{\partial x}$ $\left.\frac{\partial X_{i,Mi(z)}}{\partial x}\right\|_{x=0} = 0$ $\left.X_{i,Mi}(z)\right\|_{x=x_{max}} = K_{MiMa}X_{i,s}(z)$	(73)	$\frac{kg_i}{kg_{Mi}\cdot s}$ $-$ $\frac{kg_i}{kg_{Mi}}$	The implementation of any other boundary condition at the interface of micro and macro scale are also possible.
Case iii. for $\tau_{Micro} \gg \tau_{Macro}$: $\partial X_{i,s} \approx konst. \approx X_{i,s,GGW} \rightarrow \frac{\partial X_{i,s}}{\partial t} = 0$ This yield the micro-scale PDE from 73	(74)		Deriving τ_{Micro}
$\tau_{Micro} = \frac{s_{Mi}^2}{D_{i,Mi}}$	(75)	s	

8.6 Ratio of the diffusion times in chapter 4.3

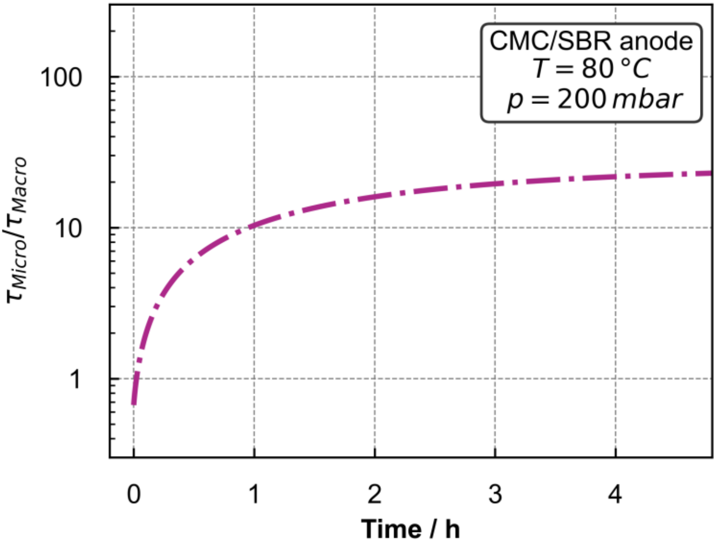

Figure 8.6: Propagation of the ratio between τ_{Micro} and τ_{Macro} over time. In the beginning the ratio is close to one which means both scales affect the mass transport in the electrode. As the electrode desorbs further, the ratio shifts towards a micro scale controlled drying.

8.7 Sorption equilibrium spherical graphite

The sorption equilibrium is used for the modeling of the drying in chapter 5. The spherical graphite was loaded with water at 30 °C. The equilibrium was measured until a threshold criterion was met. Due to an insufficiently sealed measurement cell during the desorption, the desorption of the sample was kinetically limited by inert gas in the cell. This could cause that the desorption data points could be closer to the sorption data points than indicated. This effect was included into the uncertainty interval of Figure 5.2.

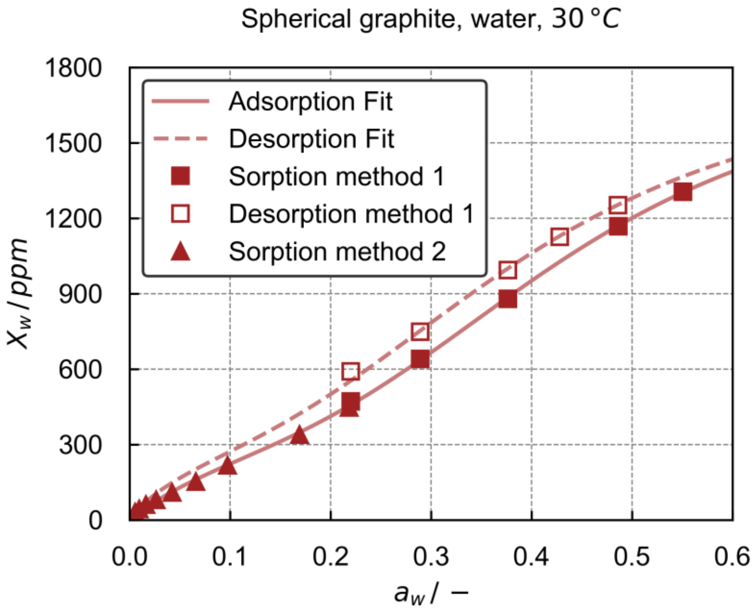

Figure 8.7: Sorption equilibrium of the spherical graphite and water. The model after Brunauer, Emmett and Teller is fitted to the sorption data. The sorption deviates from the desorption. The data were recorded by the magnetic suspension balances, method is the pure vapor method and method 2 is the perfusion method.

8.8 Comparison of analytical and numerical solutions of Equation 23

Equation 23 can be solved analytically if all coefficients of the PDE are constant. The sorption equilibrium for example is non-linear which results in variable coefficients of the PDE. A comparison of numerical and analytical solution of Equation 23 is possible if both solutions assume a linear sorption equilibrium via a sorption constant. Figure 8.8 shows these results.

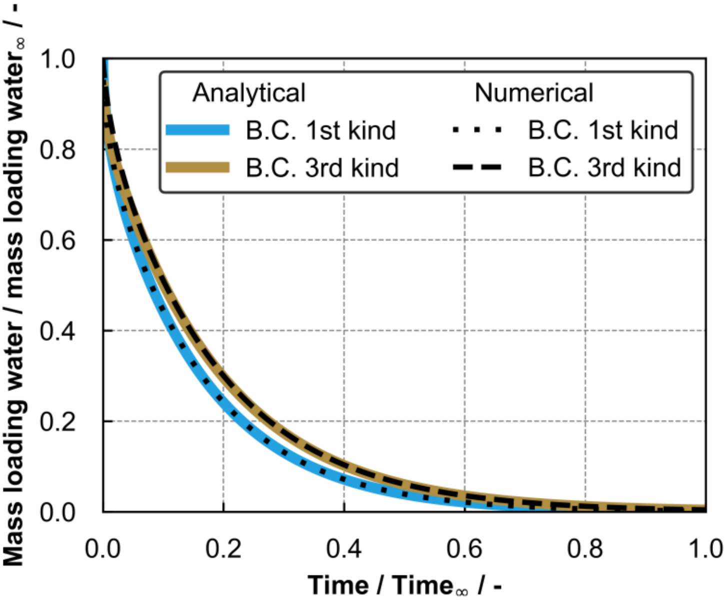

Figure 8.8: Comparison of the numerical model derived from Equation 23 to the analytical solution of Equation 23 after Kärger et al.. The numerical solutions with the Dirichlet (1st kind) and Robin (3rd kind) boundary condition both match their analytical counterpart. This is an initial validation, which shows that the numerical implementation of PDE, initial values and boundary conditions is correct.

8.9 Variation of porosity and tortuosity models

Various porosity-tortuosity models were tested to replicate the desorption of a backfill made of the anode active material graphite from chapter 5.2. The model after Zehner-Bauer-Schlünder replicated the desorption better than the other ones. Therefore, this model will be used in this study. Of course, a fitted tortuosity would yield a similar result.

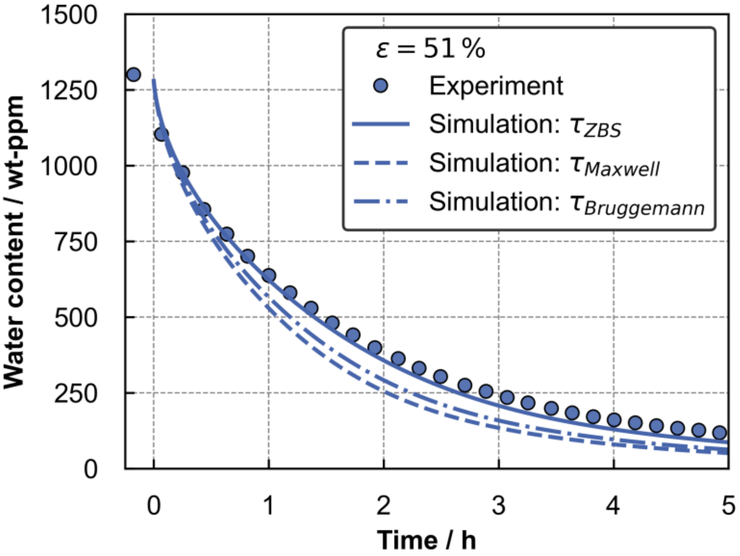

Figure 8.9: Drying of a backfill made of anode active material. The experiment were conducted at 30 °C and 800 mbar with a porosity of 51% and a height of the backfill of 40 mm. The simulation uses several tortuosity correlations: Zehner-Bauer-Schlünder (ZBS), Maxwell, and Bruggemann.

8.10 Sorption of NMC-622 at different relative humidities

The sorption of NMC-622 in humid air, did not reach an equilibrium within four days at a RH of 2.3% and within three months at a RH of 72% compare Figure 6.2. Therefore, the samples are exposed to the various relative humidities for a constant period. The RH increases after each constant period. The kinetic of the mass uptake changes if the acting sorption mechanism is accelerated by the relative humidity. This form of sorption investigation presupposes that sufficient NMC-622 is available for the mass uptake. If the mass uptake decreases with increasing RH, this presumption must be challenged. The data obtained from this RH scan are mass uptake over time. This mass uptake is quantified for each RH as mass uptake per hour and plotted over the dew-point temperature in Figure 8.10.

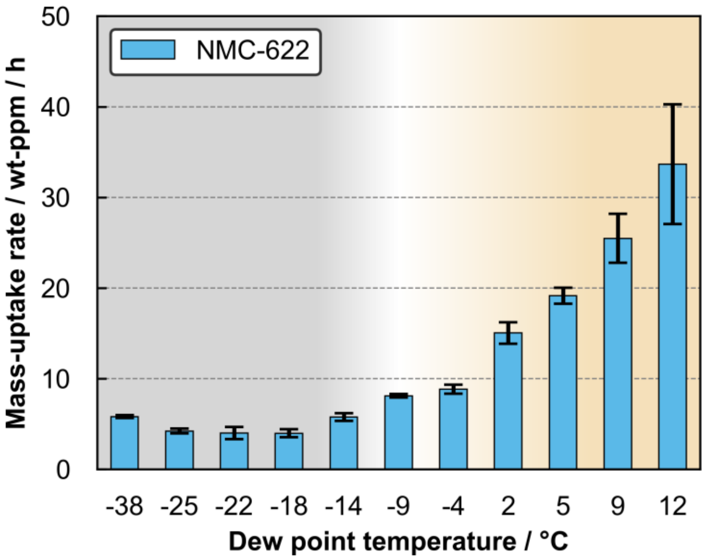

Figure 8.10: Exposure of NMC-622 to humidified air, temperature 30 °C. The CO_2-content is the one of the atmosphere approx. 400 ppm (year 2022). The mass-uptake rate is given for dew-point temperatures between -38 °C and 12 °C. Each dew-point was held for 10 h prior to succeeding to the next dewpoint temperature. The mass-uptake rate increases with rising dew-point temperature.

The rate of the mass uptake is initially higher compared to the following dew-point temperatures. The uptake rate increases after a dew-point temperature of -18 °C continuously to the largest dew-point temperature of 12 °C. The error bars show that the scatter of the results at low dewpoints is small compared to the higher dewpoints. The initial decrease and subsequent increase of the mass-uptake rate is unexpected. In the grey colored area, the rate is initially higher than the rest. However, it remains under 6 wt-ppm per hour. Other than the initially high uptake rate, this rate in the grey area appears to be unaffected by the dew-point temperature. It is possible that the higher uptake rate at -38 °C origins from the initially steep kinetic also observed in Figure 6.2. The mass-uptake rate at -20 °C of the humidity scan can be compared to the sorption in humid air form Figure 6.2: the uptake rate in the time interval between hour 10 and 30 is like the mass-uptake rate observed in the humidity scan at the same dewpoint. The rise of the mass-uptake rate at higher dew-point temperatures (yellow area) indicates that the either a mechanism is activated or a kinetic is accelerated at a certain dew-point temperature.

Conclusions about which sorption mechanism is responsible for the observed behavior is not possible. It is likely that multiple mechanisms overlap. Differentiating between the sorption with and without CO_2 can give further insight into the acting sorption mechanism. Excluding CO_2 from the experiment will assure that the mass transport of CO_2 into the sample is not responsible for this observation.

8.11 Calculation of CO_2 mass transport chapter 6.2 and 6.3

A “worst-case” estimation that considers the mass transport of CO_2 into the sample of the NMC-622 evaluates if this mass transport must be considered during the analysis of the experiments. The equations from chapter 3.3.1 are used with a theoretical sorption constant. This sorption constant is chosen to enable the worst-case estimation. At the CO_2 concentration of the atmosphere (400 vol-ppm), the NMC-622 is assumed to adsorb 1000 wt-ppm of CO_2. This is four times more, than experimentally observed. Figure 8.11 show the simulation results.

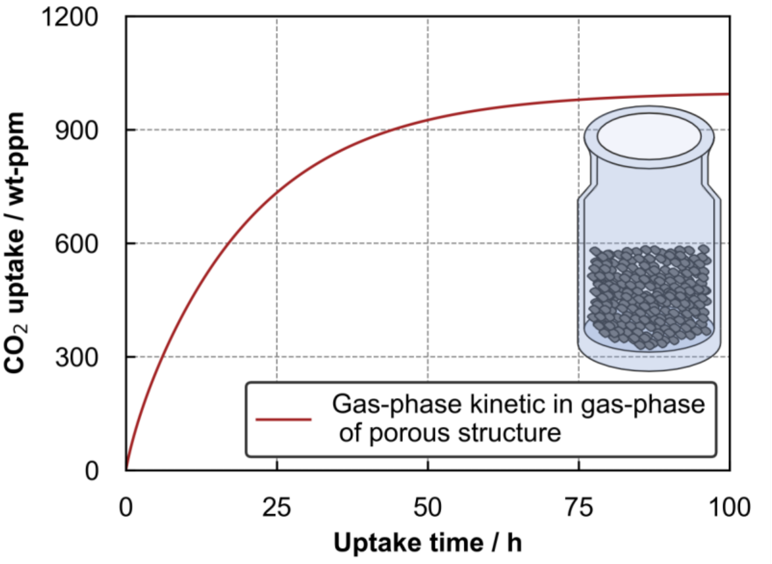

Figure 8.11: Theoretical CO_2 uptake curve in the sample of the NMC-622. The gas phase with 400 vol-ppm CO_2 provides enough CO_2 within 100 h to reach 1000 wt-ppm uniformly across the sample. This shows, that based on the gas-phase mass-transport kinetic in the sample holder, the mass uptake could be four times larger than experimentally observed.

The Figure plots CO_2 uptake over time. The simulation is conducted at experimental process conditions and with an average pore diameter of 0.8 µm. If the mass transport in the gas phase of the NMC-622 sample restricts the mass uptake of the sample, the mass uptake could be four times higher than the experimental observation. This is further indication that the mass uptake in the experiment is restricted by a different kinetic than the gas-phase mass transport. Figure 8.12 shows the gradients of the simulation from Figure 8.11. The distance between 0 cm and 1.5 cm is the NMC-622. The distance between 0 cm and 1.5 cm is the resting gas layer on top of the sample. The gradients are almost at equilibrium after 67 h.

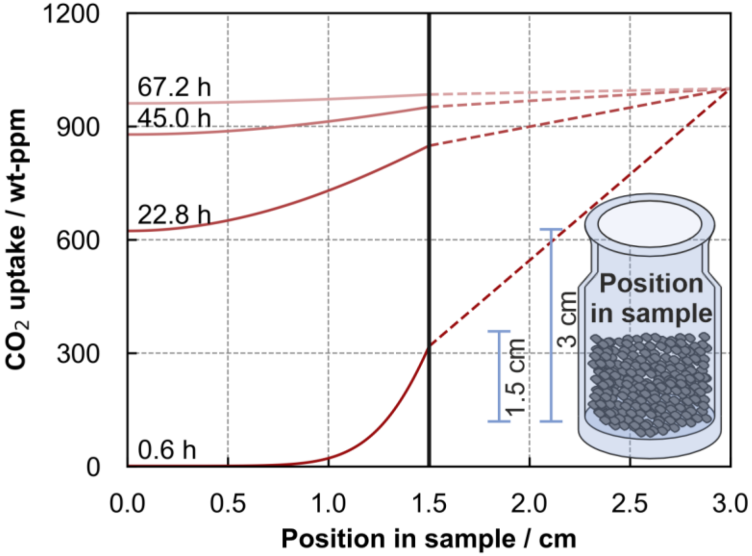

Figure 8.12: Gradients of the simulation from Figure 8.11 at four time steps. Position 0 marks the bottom of the sample vail. Position 1.5 cm marks the surface of the NMC-622 particle. The distance between 1.5 cm and 3 cm is the resting gas-layer on top of NMC-622. The gradients are nearly equilibrated after 67 h.

8.12 Further references

Publications

(1) **T. Heckmann**, P. Barbig, A. T. Pham, J. C. Eser, P. Scharfer, W. Schabel, W. *Simulation of the water mass transport in electrodes during post-drying and moisture management of Li-ion battery production via the Two-Scale-Model*, Drying Technology, 2026. 10.1080/07373937.2026.2631674

(2) **T. Heckmann**, M. Lechner, P. Barbig, X. Gui, L. Madlindl, P. Scharfer, R. Daub, W. Schabel. *Influence of CO2 in the Li-ion battery-production atmosphere on the sorption kinetics of Li[Ni0.6Co0.2Mn0.2]O2 and its effect on cell performance,* Journal of Energy Storage, 2026. 10.1016/j.est.2026.120994

(3) F. Fenske, **T. Heckmann**, P. Michalowski, P. Scharfer, W. Schabel, A. Kwade. *Impact of humidity on moisture resorption and resulting electrochemical performance of Gr/NMC622-based Li-ion batteries,* Journal of Energy Storage, 2025. 10.1016/j.est.2025.116238

(4) M. Lippke, C. Willuhn, T. Ohnimus, **T. Heckmann**, P. Scharfer, W. Schabel, C. Schilde, A. Kwade. *Coupled numerical simulation of the drying and calendering for Lithium-ion battery anodes with non-spherical particles,* Powder Technology, 2025. 10.1016/j.powtec.2024.120566

(5) **T. Heckmann**, L. Madlindl, P. Scharfer, W. Schabel. *Increased Water Uptake of Li[Ni 0.6Co0.2Mn0.2]O2 for Lithium-Ion Batteries in Humid Nitrogen above a Critical Gas Dew Point*, ACS Applied Energy Materials, 2024. 10.1021/acsaem.3c02976

(6) A. Altvater, J. Klemens, J. Borho, A. Smith, **T. Heckmann**, P. Scharfer, W. Schabel. *Application of Multistage Drying Profiles for Accelerated Production of Li-Ion Battery Anodes Using Infrared Radiation: Validation with Electrochemical Performance and Structural Properties*, Energy Technology, 2024. 10.1002/ente.202301272

(7) G. V. Silva, **T. Heckmann**, T. Abraham, P. Scharfer, W. Schabel, C. Herrmann. *Model-based process design under consideration of*

production performance for battery cell production: A coating and drying study, Procedia CIRP, 2023. 10.1016/j.procir.2023.09.075

(8) **T. Heckmann**, J. C. Eser, A. Altvater, J. Dörr, H. Lepère, P. Scharfer, W. Schabel. *Mass transport in the Stefan Knudsen transition region during vacuum drying at different pressures in a porous structure resembling battery electrodes,* Langmuir, 2023. 10.1021/acs.langmuir.2c03450

(9) C. A. Heck, F. Huttner, J. K. Mayer, O. Fromm, M. Börner, **T. Heckmann**, P. Scharfer, W. Schabel, M. Winter, A. Kwade. *Production of nickel-rich cathodes for lithium-ion batteries from lab to pilot scale under investigation of the process atmosphere*, Energy Technology, 2023. 10.1002/ente.202200945

(10) M. Ling, N. Zimmerer, J. Schäfer, P. Quarz, **T. Heckmann**, P. Scharfer, W. Schabel, J. Fleischer. *Investigation on a micro-environment concept for MEA production process supported by numerical simulations*, Proceeding - 2nd Fuel Cell Conference Chemnitz, 2022.

(11) A. Altvater, **T. Heckmann**, J. C. Eser, S. Spiegel, P. Scharfer, W. Schabel. *(Near-) Infrared Drying of Lithium-Ion Battery Electrodes: Influence of Energy Input on Process Speed and Electrode Adhesion*, Energy Technology, 2022, 10.1002/ente.202200785

(12) G. V. Silva, M. Thomitzek, M. Lippke, **T. Heckmann**, H. Karaki, C. Lischka, F. Möhlen, D. Mayer, J. Hagemeister, R. Daub, J. Fleischer, H. Nirschel, D. Schröder, P. Scharfer, W. Schabel, A. Kwade, C. Herrmann. *Digitalization Platform for Sustainable Battery Cell Production: Coupling of Process, Production, and Product Models*, Energy Technology, 2022. 10.1002/ente.202200801

(13) M. Lippke, T. Ohnimus, **T. Heckmann**, D. Ivanov, P. Scharfer, W. Schabel, C. Schilde, A. Kwade. *Simulation of Structure Formation during Drying of Lithium-Ion Battery Electrodes using Discrete Element Method*, Energy Technology, 2022. 10.1002/ente.202200724

(14) A. Hoffmann, S. Spiegel, **T. Heckmann**, P. Scharfer, W. Schabel. *CFD model of slot die coating for lithium-ion battery electrodes in 2D and 3D with load balanced dynamic mesh refinement enabled with a local-slip boundary condition in OpenFOAM*, Journal of

Coatings Technology and Research, 2022. 10.1007/s11998-022-00660-8

(15) **T. Heckmann**, J.C. Eser, A. Altvater, N. Streller, P. Scharfer, W. Schabel. *Experimental Investigation of the Temperature, Pressure, and Binder System Influence on Vacuum Postdrying Processes and Moisture Management of Li-Ion Battery Electrodes*, Energy Technology, 2022. 10.1002/ente.202200859

(16) S. Spiegel, **T. Heckmann**, A. Altvater, R. Diehm, P. Scharfer, W. Schabel. *Investigation of Edge Formation during the Coating Process of Li-Ion Battery Electrodes*, Journal of Coatings Technology and Research, 2022. 10.1007/s11998-021-00521-w

(17) F. Huttner, A. Diener, **T. Heckmann**, J. C. Eser, T. Abali, J. K. Mayer, P. Scharfer, W. Schabel, A. Kwade. *Increased Moisture Uptake of NCM622 Cathodes after Calendering due to Particle Breakage*, Journal of the Electrochemical Society, 2021. 10.1149/1945-7111/ac24bb

(18) F. Huttner, A. Marth, J. C. Eser, **T. Heckmann**, J. Mohacsi, J. K. Mayer, P. Scharfer, W. Schabel, A. Kwade. *Design of Vacuum Post-Drying Procedures for Electrodes of Lithium-Ion Batteries*, Batteries & Supercaps, 2021. 10.1002/batt.202100088

(19) **T. Heckmann**, J. D. Schiffman. *Spatially Organized Nanopillar Arrays Dissimilarly Affect the Antifouling and Antibacterial Activities of Escherichia coli and Staphylococcus aureus*, ACS Applied Nano Materials, 2019. 10.1021/acsanm.9b01942

Conference contributions

(1) **T. Heckmann**, P. Barbig, P. Scharfer, W. Schabel. *Multi-component mass-transport model of water in electrodes during moisture management and post drying of battery electrodes*. Annual Meeting of the Subject Division Heat and Mass Transfer, March 11 - 13, 2024, Magdeburg, Germany. (Talk)

(2) **T. Heckmann**, P. Barbig, P. Scharfer, W. Schabel. *Post-drying: simulation and experiments of micro- and macro-scale mass transport*. International Battery Production Conference, November 07 - 09, 2023, Brunswick, Germany. (Talk)

(3) **T. Heckmann**, P. Scharfer, W. Schabel. *Sorption and Diffusion Processes in Cathode Active Materials for Lithium-ion Batteries during the Production of Electrodes*. European Coating Symposium, September 13 - 15, 2023, Paris, France. (Talk)

(4) **T. Heckmann**, A. Altvater, J. Eser, P. Scharfer, W. Schabel. *Sorption and mass transport through multi-component, porous structures during moisture management of battery electrodes*. Annual Meeting of the Subject Division Heat and Mass Transfer, March 06 - 08, 2023, Frankfurt, Germany. (Talk)

(5) **T. Heckmann**, A. Altvater, J. Eser, P. Scharfer, W. Schabel. *Towards an efficient humidity management for electrodes of Li-ion batteries*. Batterieforum Deutschland, January 18 - 20, 2023, Berlin, Germany. (Poster)

(6) **T. Heckmann**, J. Eser, P. Scharfer, W. Schabel. *A time-resolved investigation of the vacuum post-drying for lithium-ion-battery electrodes*. International Battery Production Conference, November 07 - 08, 2022, Brunswick, Germany. (Talk)

(7) **T. Heckmann**, J. Eser, P. Scharfer, W. Schabel. *Mass Transport in Porous Thin Films during the Post-Drying of Battery Electrodes*. International Coating Science and Technology Symposium (ISCST), September 11 - 14, 2022, Minneapolis, USA. (Talk)

(8) **T. Heckmann**, J. Eser, P. Scharfer, W. Schabel. *Mass transport in porous media applied to the electrode production and moisture management during battery assembly*. Annual Meeting of the Sub-

ject Division Heat and Mass Transfer, July 18 - 20, 2022, Würzburg, Germany. (Talk)

(9) **T. Heckmann**, J. Eser, P. Scharfer, W. Schabel. *Vacuum post drying of Li-ion battery electrodes*. Annual Meeting of the Subject Division Drying Technology, March 10 - 11, 2022, Frankfurt, Germany. (Talk)

(10) **T. Heckmann**, J. Eser, A. Altvater, P. Scharfer, W. Schabel. *Humidity management and post drying of electrodes for Li-ion batteries: experiments and simulation*. Batterieforum Deutschland, January 19 - 25, 2022, online. (Poster)

(11) G. Silva, **T. Heckmann**, T. Abraham, P. Scharfer, W. Schabel, C. Herrmann. *The influence of process parameters on the intermediate electrode structure and process chain performance: a coating and drying study*. Batterieforum Deutschland, January 19 - 25, 2022, online. (Poster)

(12) **T. Heckmann**, A. Altvater, J. Eser, P. Scharfer, W. Schabel. *About the vacuum post-drying process in the production of lithium-ion batteries*. International Battery Production Conference (IBPC), November 01 - 03, 2021, Brunswick, Germany. (Talk)

(13) **T. Heckmann**, J. Eser, P. Scharfer, W. Schabel. *Sorption and mass transport investigations in porous thin films applied to the post-drying process of lithium-ion battery electrodes*. European Coating Symposium 2021, September 07 - 09, 2021, Brussels, Belgium. (Talk)

(14) **T. Heckmann**, J. Eser, A. Altvater, P. Scharfer, W. Schabel. *Theoretical Comparison of Different Strategies for Post-Drying Process of Lithium-ion Battery Electrodes*. Annual Meeting of the Subject Division Drying Technology, March 15 - 16, 2021, online. (Poster)

(15) **T. Heckmann**, J. Eser, A. Altvater, P. Scharfer, W. Schabel. *Water Mass Transport Simulation on Porous Media Applied to the Post-Drying Process of Lithium-Ion Battery Electrodes*. Annual Meeting of the Subject Division Heat and Mass Transfer, February 24 - 25, 2021, online. (Poster)

(16) J. Eser, **T. Heckmann**, A. Altvater, H. Lepère, P. Scharfer, W. Schabel. *Vacuum for post-drying of electrodes for Li-ion batteries:*

experiments and simulation. Batterieforum Deutschland, January 20 - 27, 2021, online. (Poster)

(17) **T. Heckmann**, J. Eser, A. Altvater, R. Banzhaf, P. Scharfer, W. Schabel. *Simulation of water mass transport during the post-drying process in the production of lithium-ion batteries*. International Battery Production Conference (IBPC), November 02 - 04, 2020, online. (Poster)

(18) **T. Heckmann**, S. Spiegel, C. Wachsmann, R. Diehm, P. Scharfer, W. Schabel. *Modeling of Edge Formation during the Slot-Die Coating of Lithium-Ion Battery Electrodes Based on CFD-Simulation*. International Coating Science and Technology Symposium (ISCST), September 20 - 23, 2020, online. (Poster)

(19) **T. Heckmann**, J. Eser, J. Kumberg, S. Spiegel, P. Scharfer, W. Schabel. *Integrated Simulation of Drying Phenomena in Lithium-Ion Battery Electrodes with Focus on Mass Transport Mechanisms*. Annual Meeting of the Subject Division Heat and Mass Transfer, March 12 - 13, 2020, Erfurt, Germany. (Poster)

(20) **T. Heckmann**, Shiuan-Ying Peng, T. Börnhorst, Ying-Chih Liao, P. Scharfer, W. Schabel. *Band Gap Induced by Halide Gradiant for Self-Passivating Perovskite Solar Cells*. European Coating Symposium 2019, September 08 - 11, 2019, Heidelberg, Germany. (Poster)

Awards

- Best Lecture Award (1st place), Annual Meeting of the Subject Division Drying Technology, March 2022, Frankfurt
- Poster Award (2nd place), Batterieforum Deutschland, January 2021, online
- Poster Award (1st place), International Coating Science and Technology Symposium (ISCST), September 2020, online